Additive Manufacturing of Critical Components – Phase II

Final Report

Prepared under:

**NCMS Project No. 142094 and
Cooperative Agreement HQ0034-20-2-0007
for the
Commercial Technologies for Maintenance Activities (CTMA) Program**

November 2024

**National Center for Manufacturing Sciences
3025 Boardwalk
Ann Arbor, Michigan 48108**

Table of Contents

Section   **Page**

This information, as disclosed to DOD, shall not be modified without the written consent of NCMS.   iii

DISTRIBUTION STATEMENT A. Approved for public release. Distribution is unlimited. OPSEC#9316

List of Figures

Figure   **Page**

This information, as disclosed to DOD, shall not be modified without the written consent of NCMS.   vii

DISTRIBUTION STATEMENT A. Approved for public release. Distribution is unlimited. OPSEC#9316

List of Tables

This information, as disclosed to DOD, shall not be modified without the written consent of NCMS.

ix

DISTRIBUTION STATEMENT A. Approved for public release. Distribution is unlimited. OPSEC#9316

Acronyms and Abbreviations

Term	Definition
AG	As-Grown
AGB	Accessory Gearbox
AI	Artificial Intelligence
AM	Additively Manufacturing/Additively Manufactured
AMCM	Additive Manufacturing Customized Machines
AMoCC	Additive Manufacturing of Critical Components
ANN	Artificial Neural Network
API	Application Programming Interface
BSE	Backscattered Electron
CAD	Computer-Assisted Design
CD	Confidence on Distribution
CMOS	Complementary Metal Oxide Semiconductor
CT	Computed Tomography
CTMA	Commercial Technologies for Maintenance Activities
DDAMC	Digital Design and Additive Manufacturing Center
DfAM	Design for Additive Manufacturing
DM	Desktop Metal
DOD	Department of Defense
DOE	Design of Experiments
Dv	Depth of Valley
EBM	Electron Beam Melting
EBSD	Electron Back Scatter Diffraction
ECDF	Empirical Cumulative Distribution Function
EDS	Energy-Dispersive X-ray Spectroscopy
ERL	Eaton Research Labs
FCC	Face Centered Cubic
FCGR	Fatigue Crack Growth Rate
FEA	Finite Element Analysis
FPI	Fluorescent Penetrant Inspection
GELU	Gaussian Error Linear Unit
GTAW	Gas Tungsten Arc Weld

This information, as disclosed to DOD, shall not be modified without the written consent of NCMS.   xi

DISTRIBUTION STATEMENT A. Approved for public release. Distribution is unlimited. OPSEC#9316

GVSC   Ground Vehicle Systems Center

HCF   High Cycle Fatigue

HIP   Hot Isostatic Pressing

ID   Inner Diameter

IPA   Isopropyl Alcohol

IR   Infrared

LCF   Low Cycle Fatigue

LOF   Lack of Fusion

L-PBF   Laser Powder Bed Fusion

M&P   Machined and Polished

MAE   Mean Absolute Error

MLP   Multi-Layer Perceptron

NCMS   National Center for Manufacturing Sciences

OD   Outer Diameter

ODASD-MR   Office of the Deputy Assistant Secretary of Defense, Materiel Readiness

OEM   Original Equipment Manufacturer

OT   Optical Tomography

PAC   Precision Aerospace Corporation

PBA   Powder Bed Analysis

PRS   Powder Removal System

R_a Surface Roughness

QMP   Qualified Machine Parameters

Rm1   Remedial Surface Chem Milled

S_a Areal Average Roughness

SE   Secondary Electron

SEM   Scanning Electron Microscopy

T&P   Turned and Polished

U.S.   United States

USF   Ultrasonic Fatigue

UTS   Ultimate Tensile Strength

VFD   Variable Frequency Drive

VHCF   Very High Cycle Fatigue

YS   Yield Strength

1. Executive Summary

Challenges that exist with additive manufacturing (AM) are the lack of defined standards for the qualification and certification of the materials and processes, and variability from process to process. This lack of standards and certification has an adverse effect on maintenance and sustainment tasks and can prolong the repairs of critical equipment as maintainers must wait for traditionally manufactured parts from a sluggish supply system. Promising results were identified at the conclusion of Phase I and relevant efforts were continued in Phase II.

Funding was secured for the collaborative initiative through the National Center for Manufacturing Sciences (NCMS) Commercial Technologies for Maintenance Activities (CTMA) Program and the Office of the Deputy Assistant Secretary of Defense, Materiel Readiness (ODASD-MR).

1.1 Results

A complete explanation of the results of Phase II is presented in Section 3. To summarize:

- Rapid qualification procedures were developed for laser powder bed fusion (L-PBF) AlSi10Mg via ultrasonic fatigue (USF). Results may prove inconclusive due to spread in underlying base fatigue data.

- Dependence of fatigue performance on surface and defect structure within thin-walled binder 17-4 binder jetting specimens was established, allowing for improved component fabrication in the future.

- Non-Gaussian beam shaping in L-PBF AlSi10Mg can realize a potential >2X increase in build productivity.

- Aluminum port-and-pressure plate successfully designed and built in L-PBF. Component can be improved by making the design less conservative going forward.

- Improvement in fatigue performance with some chemical milling operation on electron beam melting (EBM) Ti-6Al-4V in coupon and component level testing. This finding will be implemented in subsequent Eaton components.

- Improvement in binder jetting 17-4 and 4340 mechanical properties achieved.

- 17-4 binder jet steel rotor built and successfully spin tested.

- Various in-situ monitoring techniques assessed and down-selected for future use.

- Crack growth models developed both for binder jetting 17-4 and AM Ti-6Al-4V in two modalities.

1.2 Benefits

Prior to this project's initiation, there were several identified key technological gaps in AM that had not been adequately addressed by industry. Specific key benefits of this project include: a more complete understanding of AM in-situ monitoring techniques, crack growth mechanisms in Ti-6Al-4V, and rapid qualification methodologies for high-throughput fatigue testing of AM materials. The encouraging results will result in adoption of key in-situ monitoring technologies and the fabrication of materials with improved mechanical properties. New materials, including 4340 and 8620 steels,

This information, as disclosed to DOD, shall not be modified without the written consent of NCMS.   13

DISTRIBUTION STATEMENT A. Approved for public release. Distribution is unlimited. OPSEC#9316

have been produced via binder jetting as a part of this project, allowing for greater property space in application.

More generally, this project has been beneficial in the sense that it allows for greater acceptance of AM as a legitimate means of fabricating components in applications with higher degrees of criticality. It has been successfully demonstrated that these next generation Phase II components have performed at or exceeded baseline requirements. This leads to increased confidence in the utility of AM going forward.

1.3 Recommendations

- Rapid qualification procedures via USF remain a promising avenue for future research. Other AM modalities and materials systems deserve scrutiny in future work. This can be done using a similar design of experiment.

- Learnings from thin-walled and surface studies should be applied to steel binder jetting builds for greater control of fatigue performance. Caution must be employed during component design.

- Non-Gaussian beam shaping should be incorporated in select L-PBF applications. By adding the necessary infrastructure, improved productivity can be realized.

- Chemical milling on EBM Ti-6Al-4V components is a viable method for improving fatigue performance.

- 4340 and other steels should be further developed in binder jetting. Full mechanical and qualification testing likely requires a large collaborative effort.

- 17-4 binder jet steel rotor can be developed further with the goal of reaching low-rate initial production.

- Certain growth models developed both for binder jetting 17-4 and AM Ti-6Al-4V in two modalities.

1.4 Invention Disclosure

☐ Yes Inventions   ☒ No Inventions
DD882 Invention Report sent to NCMS ☒

1.5 Project Partners

- U.S. Army Ground Vehicle Systems Center (GVSC)

- Eaton Corporation, ExOne

- University of Michigan

- Brown University

- National Center for Manufacturing Sciences (NCMS)

2. Introduction

2.1 Background

Traditional multi-step manufacturing techniques are costly, time consuming and can create significant delays for organizations charged with keeping both commercial and military vehicle fleets operational. AM offers a unique solution to this problem but testing of critical parts and components manufactured via AM has lagged behind current technologies. Currently there are several different types of AM processes and equipment, and the technology is constantly evolving. Each different type of AM process can have a unique and specific set of variables from one type of process to another. These variables have a direct impact on the resulting material properties and fatigue life of the produced component. Variation in material properties can also be present between a test coupon and a component utilizing the same process parameters. This variation can be influenced by geometry, cooling rate and surface roughness. The resulting variation in material properties is a direct result of the material microstructure. Differences in material microstructure result in differences in material performance. Differences in microstructure are generally caused by differences in the heating and cooling of a material. The cooling rate of an AM deposition is a function of specific process parameters related to the specific AM process, the specific machine, and each specific build.

Prior to the work presented in this report, an initial Phase I of the Additive Manufacturing of Critical Components (AMoCC) project was conducted and a separate final report generated. Phase I results include the collection of a large breadth of material data for AM aluminum, titanium, and steel using L-BPF, EBM, and binder jetting, respectively. The data includes surface roughness, defect population, and fatigue properties as a baseline. This information was used to populate an intelligent material database that can be queried in the design process to optimize AM components for productivity, strength, and other relevant characteristics. One aluminum steering arm component identified by the Ground Vehicle Systems Center (GVSC) was fully demonstrated in Phase I. Pro–mising results were identified at the conclusion of Phase I and relevant efforts were continued in Phase II. This second phase was determined to be necessary in order to advance Phase I understanding of AM technologies in direct support of a diverse array of applications.

2.2 Purpose

While AM has high potential to revolutionize manufacturing, it has not been widely applied to the design of critical components. Largely this is because of limitations in material characterization and qualification procedures given the high stresses and temperatures involved in these applications. Significant variability can also exist from process to process and machine to machine, also limiting successful qualification regardless of criticality. AMoCC seeks to advance understanding of AM methodologies to mitigate these limitations through advancing several key technologies, including rapid qualification, in-situ monitoring, alloy development, and the direct manufacture of components themselves.

2.3 Scope/Approach

The second phase of AMoCC was multi-faceted, with an emphasis on advancing the most promising research avenues from the first phase. Phase II applied the lessons learned to the construction of new

This information, as disclosed to DOD, shall not be modified without the written consent of NCMS.   15

DISTRIBUTION STATEMENT A. Approved for public release. Distribution is unlimited. OPSEC#9316

components, specifically steel and titanium. Components were chosen that have a high potential for successful production via AM. Addressing the current difficulty in monitoring in-situ defects as the AM build is happening is a key problem area. Resolving this problem via the surveying of existing techniques and their adoption within the scope of this initiative will allow for greater control of defect population within a component and the resulting mechanical properties. Crack growth in AM alloys on the mesoscale is also not a widely understood phenomenon and was another area of focus that will lead to development of advanced models that can be used to mitigate crack growth in a select class of AM alloys.

The work has involved collaboration between government, industry, and academic participants. Industry (Eaton Corporation, ExOne) developed a process database with information determined by academic partners (University of Michigan, Brown University) to enable AM of critical components for the GVSC. Once developed and validated, Eaton applied this methodology to produce several critical components identified by the government.

The individual deliverables corresponding are as follows:

- Standard and validated procedure for rapid fatigue characterization.
- Optimized post-processing techniques for improved surface and fatigue performance of AM alloys.
- Optimized AM AlSi10Mg and steel performance with respect to high productivity and mechanical properties.
- AM L-PBF aluminum and/or steel component from government sponsor and/or industry partner built and tested.
- Optimized AM EBM titanium component design based on learnings from Phase I.
- AM EBM titanium component from government sponsor and/or industry partner built and tested.
- Improved material properties and dimensional accuracy in steel binder jetting.
- AM binder jetting steel component from government sponsor and/or industry partner built and tested.
- Current capability assessment for in-situ defect detection bridging research and development to production applicability (possible adoption).
- Model for prediction of critical flaw size in AM alloys.
- CTMA Quarterly Reports and a Final Report.

3. Project Narrative

The project architecture of AMoCC Phase II was multi-faceted, with many individual teams working in conjunction toward the creation of viable AM critical components. In order to enhance understanding, this narrative will be divided into separate sections according to the deliverables outlined in Section 2.3.

3.1 Standard and Validated Procedure for Rapid Fatigue Characterization

3.1.1 Rapid Qualification

AM processes such as L-PBF are obtaining widespread acceptance for the manufacture of critical structural components for aerospace and ground vehicle applications. In the coming decade AM processes are envisioned to replace traditional methods like metal casting and provide much needed resiliency in the supply chain for critical components. Validation of High Cycle Fatigue (HCF: $10^4 \leq N \leq 10^7 \ cycles$) and Very High Cycle Fatigue (VHCF: $N > 10^7 \ cycles$) properties using conventional servohydraulic equipment requires long turnaround times. For example, at a test frequency of 50 kHz, testing a component using conventional fatigue equipment to 10^9 cycles can take eight months, making rapid qualification untenable. An alternative to conventional fatigue testing is to use ultrasonic frequencies (typically in the range 15-25 kHz) and achieve the necessary stress amplitude through resonance in the specimen. USF methods have evolved over the past 70 years or so; and they can significantly reduce turnaround times for HCF/VHCF testing. For example, using USF at 20 kHz, testing to 10^9 cycles can be completed in a few days (Figure 1).
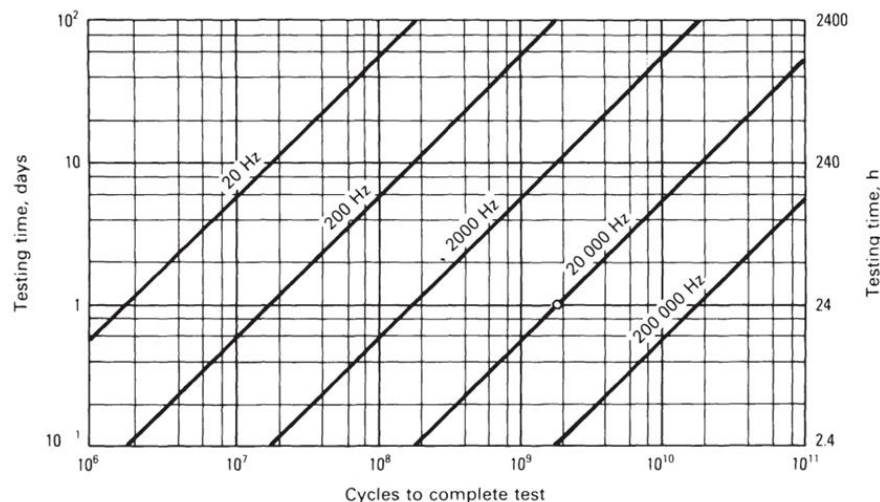
Figure 1.   Testing Times vs Number of Cycles as Function of Frequency
(Kuhn, 2000, pp.717-729)

The primary aim of this deliverable was to assess the viability of USF as a rapid qualification tool for validation of fatigue properties in as-printed AM components. Additionally, the contribution of the random nature of defects towards variability in fatigue performance of as-printed components was examined.

In terms of material, the scope of this study was restricted to AM aluminum alloy specimens. Furthermore, the specimens were tested for fatigue properties at room temperature in the as-printed condition: they were not subjected to heat treatment of Hot Isostatic Pressing (HIP) post-fabrication.

Two different testing frameworks were used to examine HCF properties – the first being a conventional servohydraulic setup at a third-party facility: (Element Materials Technologies, Cincinnati OH); and the second being the USF setup at Eaton Research Labs (ERL), Southfield, MI.

The cylindrical blanks out of which the fatigue test specimens were extracted were fabricated out of AlSi10Mg alloy by L-PBF process on EOS M400 platform at the Eaton Aerospace facility in Charleston, SC, using qualified machine parameters (QMP).

Fatigue test specimens for conventional servohydraulic and USF specimens were machined out of the blanks in the as-printed condition. The specimens for conventional fatigue testing were machined in accordance with ASTM E466 standards. The specimens for USF were machined in accordance with a geometrical specification optimized to resonate at frequency ~20 kHz. Schematic represen–tations of the geometries of the conventional and USF specimens are shown in Figure 2. The surface roughness requirement for the specimens was 0.2µm (8µin) or better.
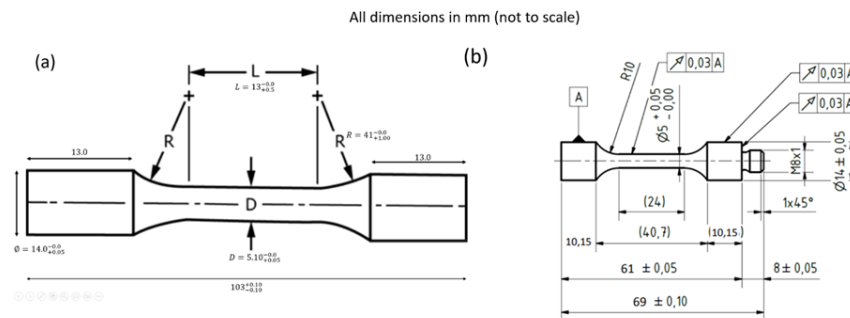
Figure 2. Schematic Showing Specimen Geometries
(a) Conventional Fatigue, (b) USF Testing

The displacement-controlled USF setup along with the specimen mounted is shown in Figure 3. The testing was conducted under fully reversed loading condition ($R = -1$), for which one end of the specimen is allowed to vibrate freely. The specimen is subjected to intermittent load, with periodic pulses accompanied by pauses for forced air cooling in order to prevent large local heating within the sample due to cyclic deformation. In the HCF and VHCF regime, the deformation behavior is approximately linear elastic. Therefore, Hooke's law can be used to calculate the cyclic stress values from measured strains. A total of 199 specimens were tested at increasing magnitudes of stress amplitudes until failure. The number of cycles for stoppage of the test at a given amplitude (run-out) was fixed at 10^8 (0.1 gigacycles).

The conventional fatigue testing was performed using a force controlled servohydraulic system under fully reversed loading conditions at test frequency of 60 Hz. The number of cycles to run-out was fixed at 10 million. A total of 30 specimens were tested at different stress amplitudes.

The plots of stress magnitude as a function of cycles to failure (S-N curves) for the two sets of specimens are shown in Figure 4. Additionally, data from conventional fatigue testing conducted at 60 Hz by Eaton's Aero division on a previously fabricated set of specimens on the same L-PBF platform using QMP is provided for comparison.
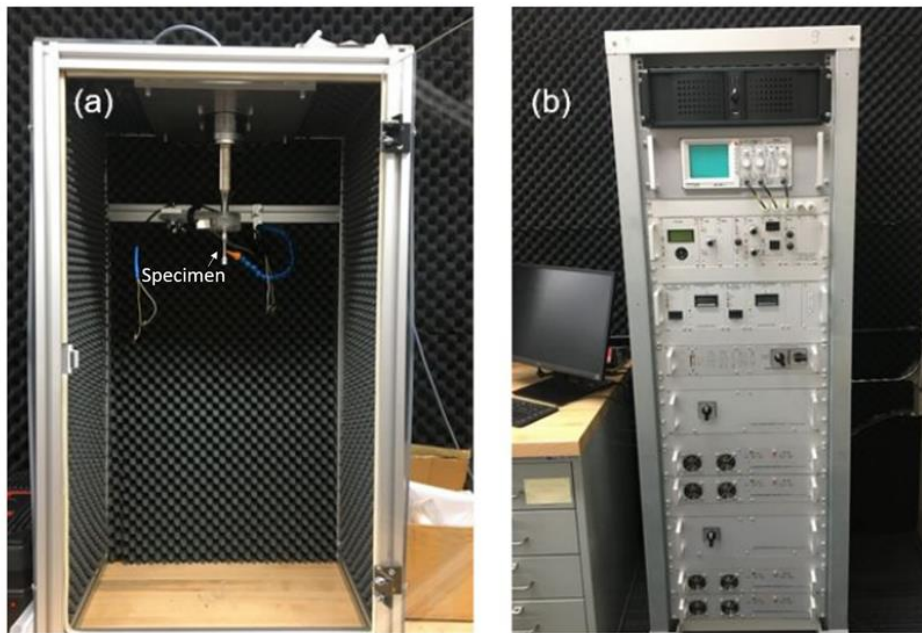
Figure 3. **USF Testing Setup at ERL**
(a) Specimen Stage and (b) Control/Data Acquisition Column
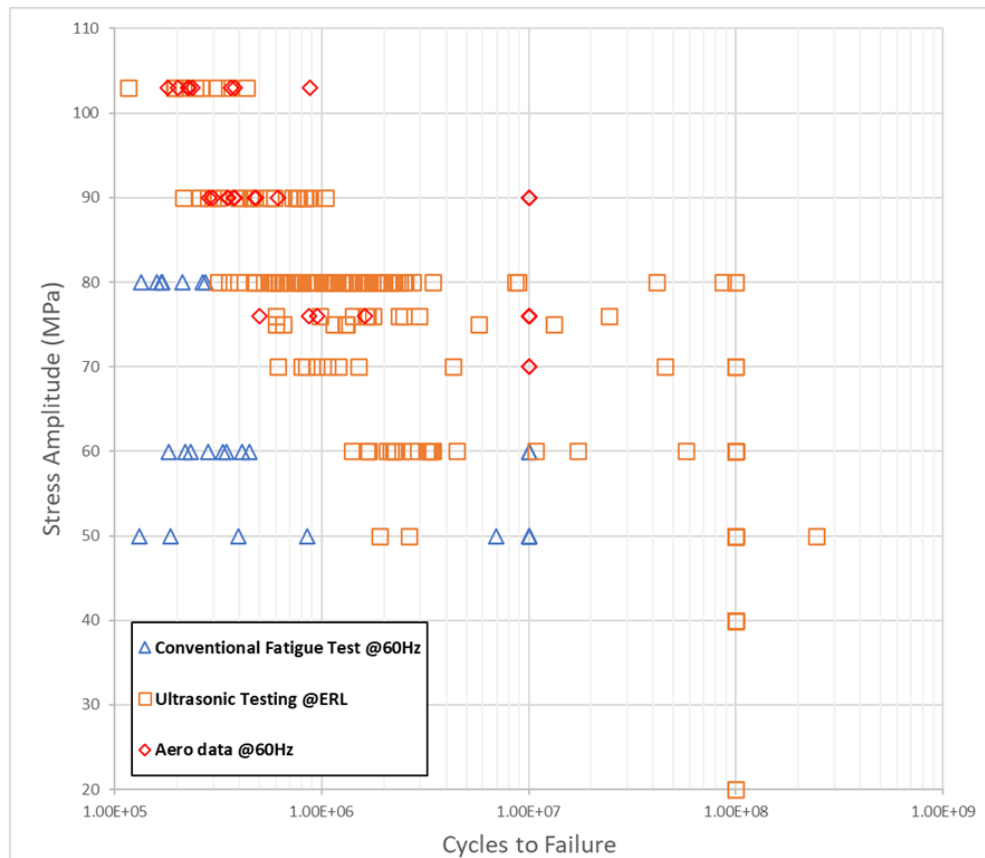
Figure 4. **S-N Curves for USF and Conventional Fatigue Test Specimens**
The points for run-out (stoppage) of the conventional and USF test were set at 10^7 and 10^8 cycles respectively

A large amount of scatter is observed among the three sets because of randomness of defect distribution in the as-built condition. Significant differences are observed between ultrasonic and conventional fatigue specimens tested out of the same build. The number of cycles to failure at 80 MPa for the conventional fatigue specimens tested at Element is of the order of 10^5. Approximately 40% of the USF specimens tested at the same stress amplitude have cycles to failure of the same order, while the remaining specimens fail at ~10^6 cycles. At stress amplitude of 60 MPa, approxi–mately 60% of the USF specimens ran out at 10^8 cycles, compared to 20% for conventional fatigue specimens. At stress amplitudes of 50 MPa, 88% of the USF specimens ran out at 10^8 cycles, whereas 50% of the conventional specimens ran out at the preset stoppage point of 10^7 cycles.

On the other hand, there is some agreement of conventional test results from a previous build and USF specimens tested at ERL. This can be observed from the test results at stress amplitudes of 70, 76, 90 and 103 MPa.

In order to obtain more granularity with regard to the spread of the datasets a box plot analysis was conducted. The plots for the three different datasets are shown in Figure 5 (conventional fatigue testing at Element materials and Eaton Aero) and Figure 6 (USF testing conducted at ERL) respectively. Cycles to failure/run-out scaled down by an arbitrary factor of 10^5 is plotted as a function of stress amplitude.

It is important to note in these plots that the scale on the Y axis is an order of magnitude higher for USF (Figure 6) because the run-out point was considered to be 10^8 cycles, compared to 10^7 cycles for conventional fatigue testing.

The comparison plots of the two datasets of the conventional test results with the corresponding USF test data are shown in Figure 7 and Figure 8. In order to make a more one-to-one comparison the cycle times of the specimens that ran out during the USF were further scaled down by a factor of 10.
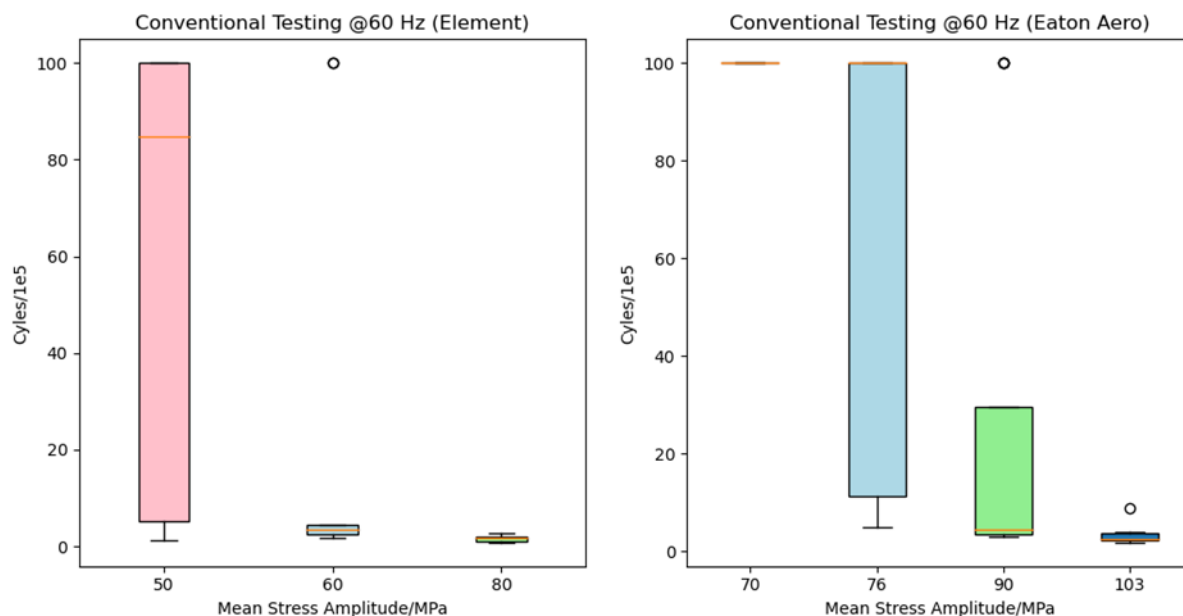
Figure 5. Box Plots for Conventional Fatigue Test Data Conducted at Element Materials (left) and Eaton Aero (right) *Showing Cycles to Failure/Run-out Plotted as Function of Stress Amplitude*
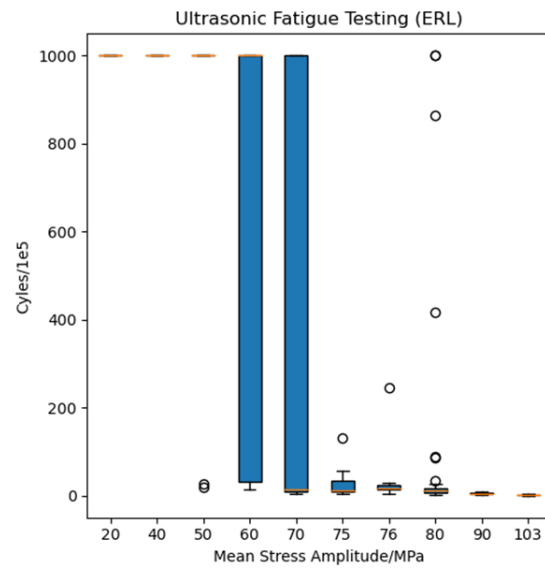
Figure 6. *Box Plot for USF Test Data Conducted at ERL*
Showing Cycles to Failure/Run-out Plotted as
Function of Stress Amplitude
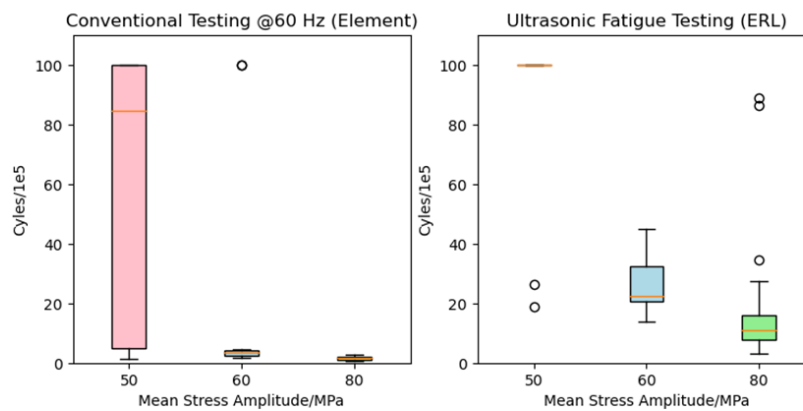
Figure 7. *Box Plots Showing Conventional Test Data (Element) with USF*
Test Data
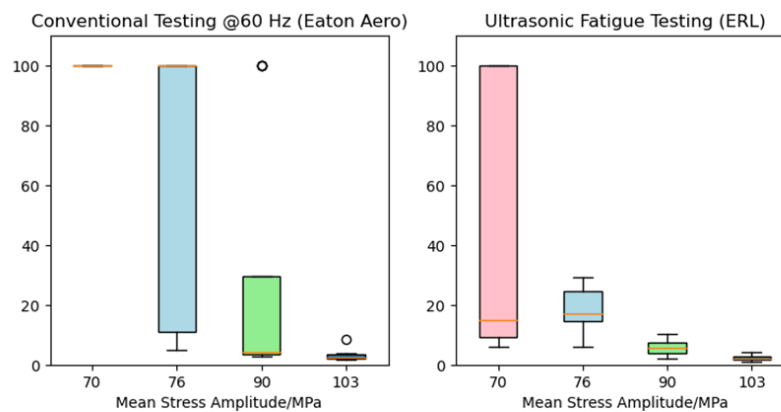
Figure 8. *Box Plots Showing Conventional Test Data (Eaton Aero) with*
USF Test Data

It can be seen that for 50 MPa stress amplitude there is a much wider scatter in the results for the conventional fatigue tests performed at Element, compared with the corresponding data from USF. The median cycle to failure for the conventional test is ~8.5E6, while most of the specimens tested at 50 MPa ran out during the USF testing. In contrast the conventional test data for 60 and 80 MPa does not show much scatter, whereas a wider variance is observed for the USF test cycle times at the same stress amplitudes. Overall, the fatigue lifetimes are higher for the USF tests.

Comparison of the ultrasonic test data with the conventional fatigue test data from Eaton Aero is shown in Figure 8. In this instance, the USF tests at amplitudes of 70 and 76 MPa seem to show lower fatigue life in comparison to conventional fatigue tests. However, good convergence between USF and conventional tests is seen at stress amplitudes of 90 and 103 MPa.

Fracture surfaces of a selected number of specimens (six each of conventional and USF) were examined using optical imaging and Scanning Electron Microscopy (SEM). The images of the characterized fracture surfaces are for each type of specimen are shown in Figure 9a-f and Figure 10a-f respectively. The region of the origin of the fatigue fracture is encircled in red in each of the figures. In each instance, SEM images from the region where the fatigue fracture originated are shown in Secondary Electron (SE) and Backscattered Electron (BSE) modes. The former mode is based on inelastic scattering of electrons closer to the material surface and are sensitive to surface topography. The latter mode is based on elastic scattering of electrons, and is sensitive to atomic mass of materials, although the image resolution tends to be lower. For each specimen, the top row
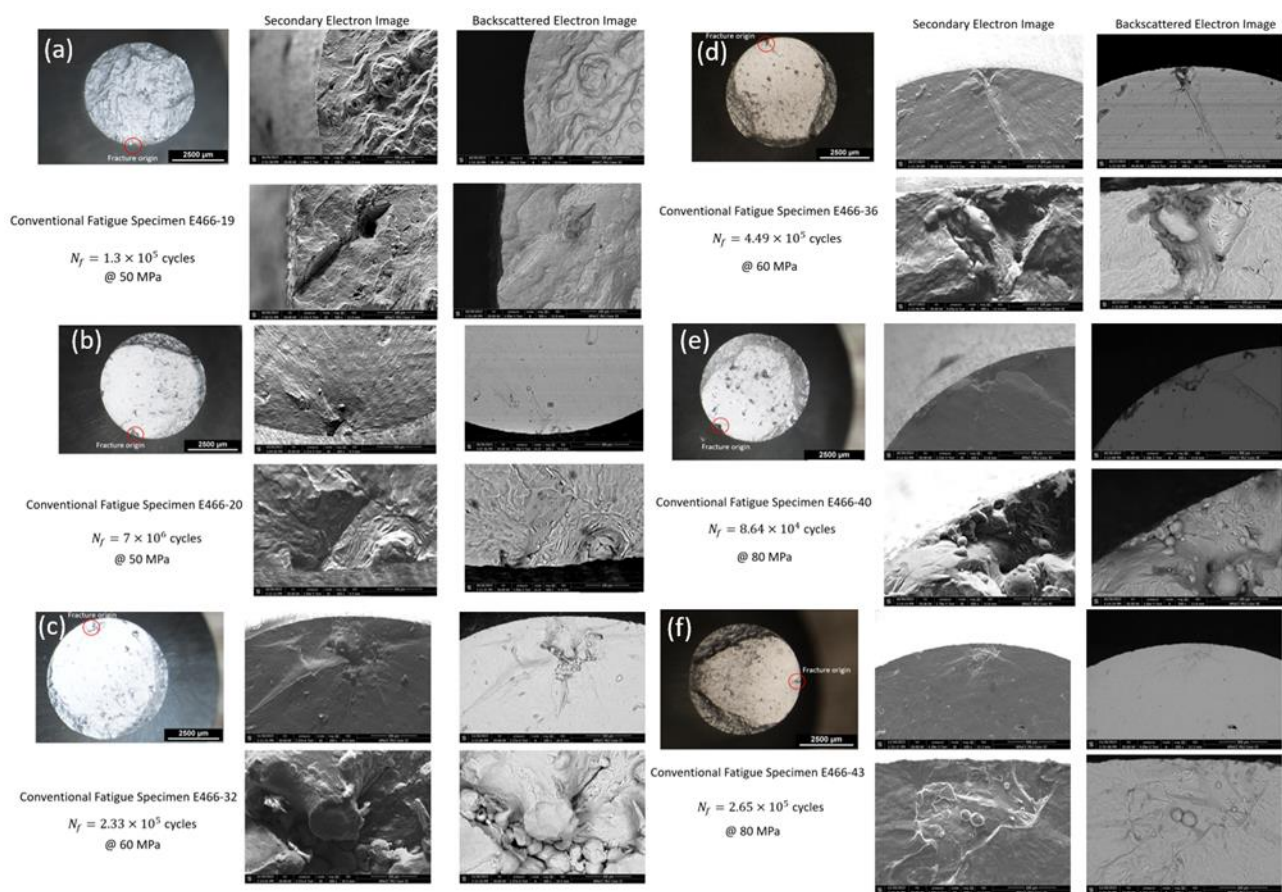
Figure 9. Optical and SEM Images of Fracture Surfaces from Six Conventional Fatigue Test Specimens

of SEM images shows the region of fracture origin at 100X, while a more magnified set of images of the same region (500X) is shown in the bottom row.

Examining the fracture surfaces of the six conventional fatigue test specimens, the balling or bead-up effect in the vicinity of the surface as a result of Rayleigh-Plateau instability seems to be the dominant mechanism of fatigue failure. This typically occurs in situations where the melt pool length is significantly larger than the melt pool width and imparts poor surface roughness (Agrawal, Rankouhi, & Thoma, 2022). The only exceptions in this group are specimens E466-19 (Figure 10a) and E466-20 (Figure 10b), where fatigue crack propagation seems to have been triggered by lining up of surface-breaking porosities.

Keyhole type defects can be observed in the USF specimens numbered 55 and 61 (Figure 10a-b). Specimen #55 ran out to the preset stoppage point of 10^8 cycles at a stress amplitude of 80 MPa. The specimen was then tested after raising the stress amplitude to 90 MPa, where it failed at 8.63E5 cycles. On the other hand, Specimen #61 had a relatively low fatigue life 1.91E6, when tested at an amplitude of 50 MPa. It is likely that the latter specimen had surface porosity that aided rapid crack propagation, even at a lower stress amplitude. Similar to most of the conventional specimens shown the Figure 9, Rayleigh-Plateau instability appears to be the predominant cause of fatigue failure in the remaining four characterized USF specimens. Specimen #172 (Figure 10f) ran out to 10^8 cycles at a stress amplitude of 60 MPa. Fatigue failure occurred at 8.91E6 cycles when the stress amplitude was increased to 80 MPa, likely due to surface porosity lining up with the unfused region caused by the ball up effect.
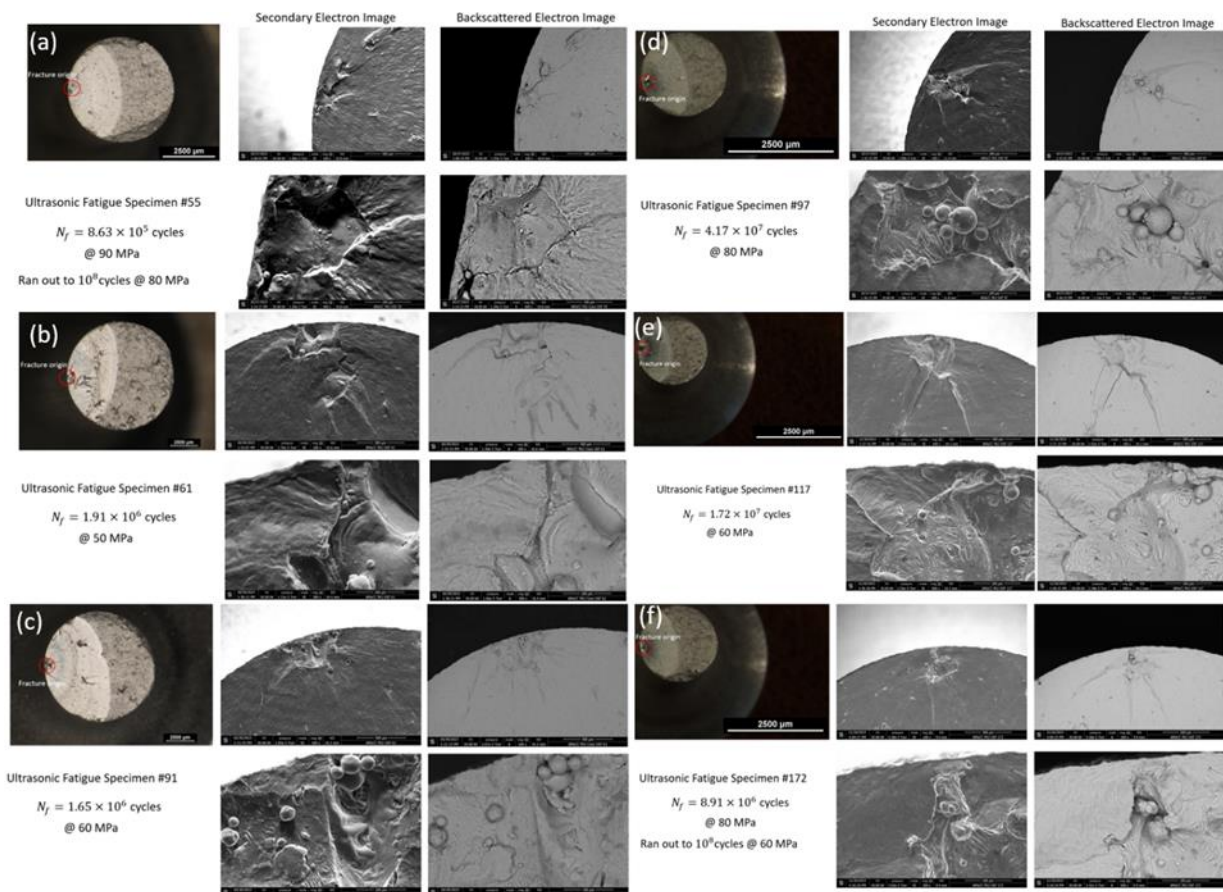
Figure 10.   Optical and SEM Images of Fracture Surfaces from Six USF Specimens

To summarize the rapid characterization work, the difference in fatigue lifetime results between conventional and USF is likely to be combination of randomness in defect occurrence, along with some contribution of frequency effects. However, review of existing literature indicates that dis–crepancy in fatigue properties between conventional and USF methods is not very significant for materials with Face Centered Cubic (FCC) crystal structure. This is because the relatively lower critical resolved shear stress in FCC materials and the availability of active slip systems at higher perturbation frequencies. Indeed, most studies predict little difference in fatigue life between conventional and USF methods (Mayer, 2016). There have been studies however, that have reported discrepancies of an order of magnitude in fatigue life between conventional and USF for E319 cast aluminum alloys (Tahmasbi, Alharthi, Webster, & Haghsenas, 2023). This difference is attributed to the change in rate of fatigue crack formation due to environmental factors. The crack growth rate at ultrasonic frequencies is expected to be lower because of lower exposure to moisture. The moisture exposure is measured in terms of the ratio of partial pressure of water vapor to the test frequency (Tahmasbi, Alharthi, Webster, & Haghsenas, 2023). Even with the same process parameters, the randomness of the defects makes it challenging to obtain concurrence of fatigue results with high degree of confidence. Use of a solution treatment and precipitation hardening cycle post-build could eliminate some of the variability associated with defect occurrence.

It is recommended that for future comparison tests, the specimens be classified into two groups – as-built and post-processed. This would yield more valuable information about the effect of post-processing operation like heat treatment and HIP on reducing the random nature of defects, thereby providing a more consistent basis for a comparative study.

3.1.2 Transfer Function

L-PBF can be used to AM critical components with complex geometries using a variety of metal alloys. In this context it is critical that defects generated during the manufacturing process be minimized or maintained at or below a predetermined threshold. This section explores the development of a cross L-PBF platform transfer function to predict optimal process parameters given a preset defect threshold. The problem statement can therefore be written as follows. Given data on defect size, volume, and shape (morphology) can the optimal process parameters for an L-PBF platform be predicted? A schematic representation of the problem statement is shown in Figure 11. Each set of defect data (size, volume, and morphology) is considered as a defect signature.
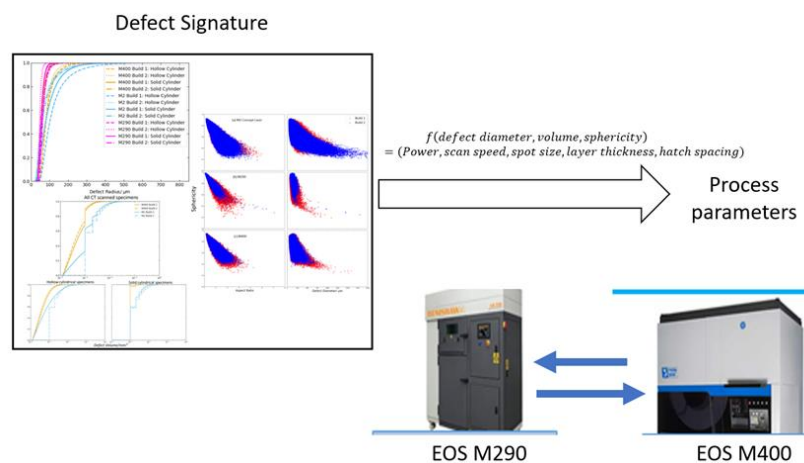
Figure 11. Schematic of Problem Statement Defining Transfer Function

Two L-PBF platforms, EOS M290 and EOS M400 were chosen for this study because their configurations of laser optics are similar. Defect data was collected using Computed Tomography (CT) scans on AlSi10Mg alloy specimens of cylindrical geometry fabricated on the two platforms.

The transfer function development is modeled as a multiple target regression problem considering the defect signature data (defect diameter, volume and sphericity) as input parameters. The first two input parameters define the size of the defect. The third parameter (sphericity) contains information about the morphology of the defect. The closer the sphericity value is to 1, the more circular its morphology is. According to available literature, sphericity values greater than 0.7 correspond to porosity time defects, while lower values are typical of linear, Lack of Fusion (LOF) type defects. The parameter space sought to be predicted by the regression model has five components – laser power, scan velocity, spot size, layer thickness and hatch spacing.

The regression problem is solved using a Multi-Layer Perceptron (MLP) based Artificial Neural Network (ANN) model. The basic principle of a single layer perceptron is shown in the inset (top right) in Figure 12. Given an input parameter space $(x_1, ..., x_n)$, the goal is to predict a regression function that will predict output parameters consistent with the training data. The input parameters are multiplied by initialized weight values. The weighted inputs are then summed and applied to an activation function produce the output f(x). The predicted output parameters are compared with the training data in each pass (epoch) and the weights are revised and the process iterates over to the next epoch and so on.

An MLP based ANN regression model uses one or more intermediate layers (known as hidden layers) to eventually arrive at the output regression function. Beginning at the input layer (in this case a three-component vector with defect diameter, volume and sphericity as the input parameters), the patterns of the training data are propagated through the ANN to generate a regression function. The regression function is then modified after comparison with the training data. The error is backpropagated and the initialized weights are recalculated, and the model is updated. This process is iterated over several epochs to arrive at a final regression function that best fits the training data. Hyperparameters (like number of hidden layers, number of epochs) can be tuned to obtain optimal results.

Figure 12. *Schematic Representation of MLP-Based ANN Regression Model*
Inset (top right) shows the basic principle of a single layer perception
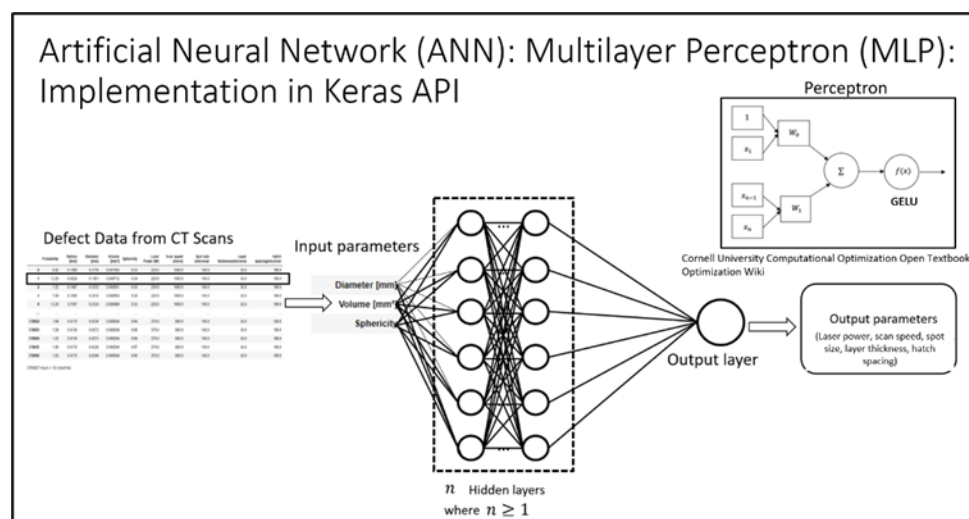
The implementation of the MLP based ANN regression model for predicting optimal machine process parameters is shown in Figure 13. The implementation is done on Keras, which is an open source, python-based Application Programming Interface (API) for deep learning applications. This particular layer has five sequential hidden layers. A Gaussian Error Linear Unit (GELU) activation function is used in this particular implementation of ANN.
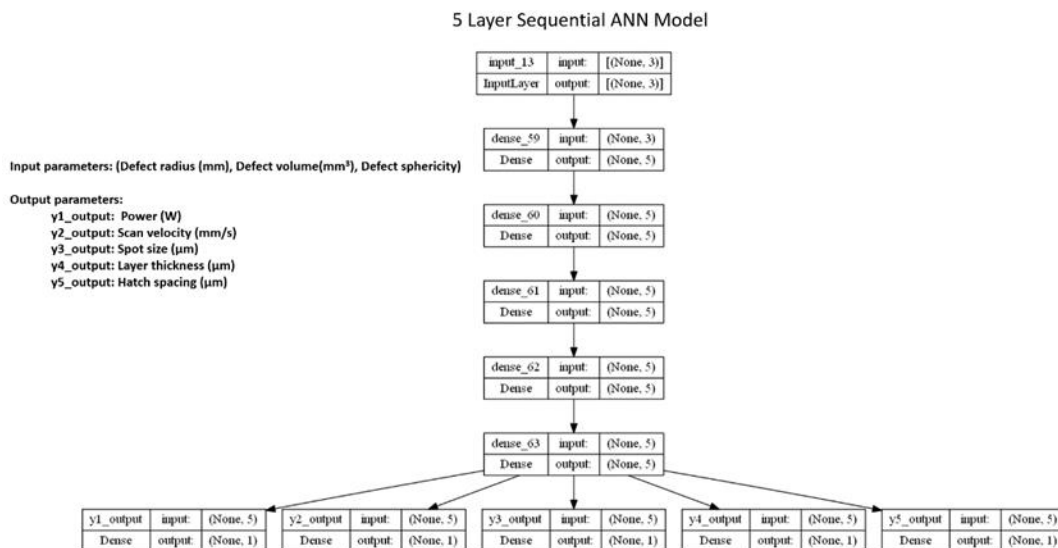
Figure 13.   Outline of Implemented Five-Layer Sequential ANN Model for Predicting L-PBF Process Parameters Based on Defect Area

Altogether, 750,000 defect data points collected from specimens fabricated on both M290 and M400 platforms were used in the ANN model. After several trials with different percentage values of split of the dataset for training and testing, it was found that a 50% split yielded the least variation in prediction between training and test data. The Mean Absolute Error (MAE) between the training and test data for each of the five output parameters are shown as a function of epochs in Figure 14. It can be seen from the plots that the MAE values decrease rapidly for the training data after the first five epochs and tend to follow an asymptotic behavior afterwards. The MAE values for the test data match the training data quite well.
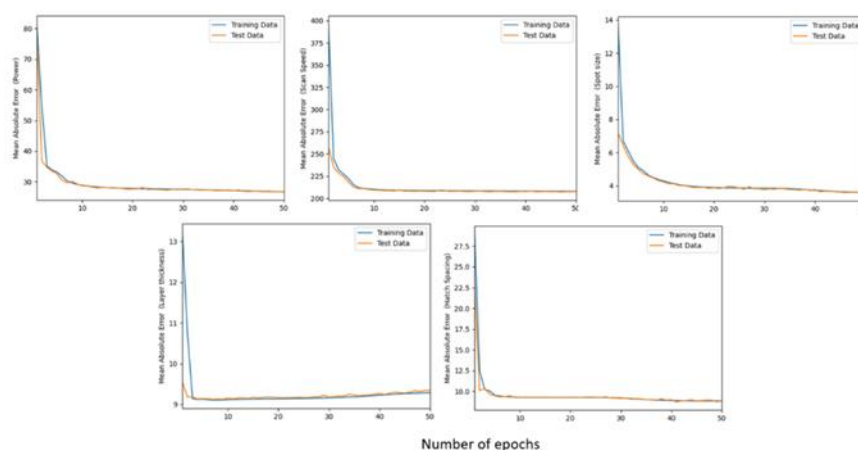
Figure 14.   Mean Absolute Error Evolution for Each of Five Output Parameters Plotted as Function of the Number of Epochs

The empirical cumulative distribution function plot for the percentage error in prediction of the test data for each of the five output parameters is shown in Figure 15. It is seen that the percent errors in prediction of the scan velocity and layer thickness are relatively high. For instance, if scan velocity is considered, approximately 81% of the 375,000 data points have a prediction error of 23% or less. Moreover, that are a smaller fraction of data points (<6%) that have an error of 100% or more.

Similarly, for layer thickness, approximately 78% of the datapoints have prediction error of 5% or less, but about 22% of the data points have error values of 50% or greater. The prediction error values are less for hatch spacing and spot size, where approximately 90% data points have less than 10% error. With respect to laser power, the error values are slightly higher where 90% of the data points have 15% or less.
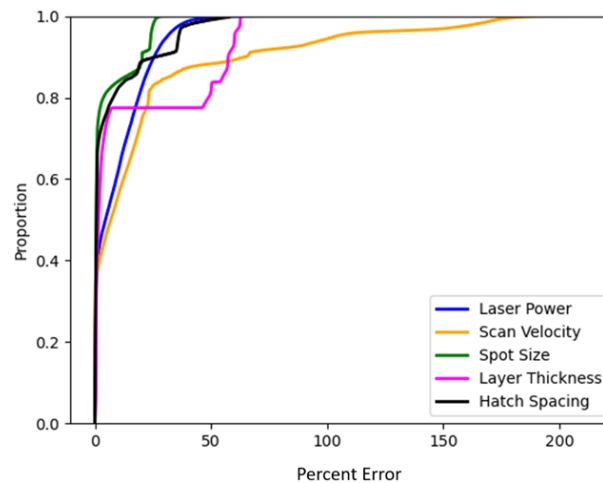
Figure 15. Empirical Cumulative Distribution Function (ECDF) Plots Showing Percentage Error in Prediction of Output Parameters for Test Data

In summary, an ANN model based on MLP was implemented to develop a predictive transfer function to generate optimal process parameters across two L-PBF platforms with similar configuration of laser optics. A composite defect dataset of 750,000 points obtained from CT scan results of AlSi10Mg specimens fabricated on the two platforms was used to train and test the regression model. The MAE values show good convergence between the training and test data. The predicted percentage error values, however, are relatively large for at least two (scan velocity and layer thickness) of the five output parameters. Further optimization of the hyperparameters would be necessary to reduce the prediction errors. Furthermore, an integer programming-based optimization algorithm needs to be interfaced with the current model so that whole number solutions are obtained that can be used to generate practically useable process parameters. Lastly, experiments to validate the generated process parameters would be useful in establishing a correlation with defect size, volume, and morphology. Overall, a data informed transfer function holds considerable promise in limiting defect occurrence in fabricated components on L-PBF platforms.

3.1.3 Thin-Walled Study on AM AlSi10Mg

Several AlSi10Mg thin-walled specimens of cylindrical and flat plate geometry were fabricated using a General Electric Concept Laser M2 UP1 Dual machine. The fabrication was completed using ranges of laser power between 219-370W, scan velocity 400-1500mm/s and spot size 50-100µm respectively. Additional specimens were fabricated using QMP proprietary to Eaton, optimized for

AlSi10Mg alloys. The specimens were fabricated at build orientations of 0°, 45°, and 55°. The wall thicknesses variation ranged from 0.2mm to 1.0mm. Details of the process parameter sets are enumerated in Table 1.

A smaller subset of specimens (shown in Figure 16) was chosen for CT scanning for nondestructive defect characterization and surface roughness measurement in the as-fabricated condition. Helical CT scans were performed using a Nikon™ XTH 225 system equipped with a Perkin Elmor 4343 detector panel having a resolution of 2850×2850 pixels. Surface roughness (R_a) measurements were conducted using a Zygo™ Newview 7000 series optical profilometer.

Table 1. Details of Process Parameters Used for Specimen Fabrication

Parameter Set	Parameter Description	Contour					Hatch/Infill					
		Spot Size (μm)	Power (W)	Scanning Speed (mm/s)	Offset From Contour (mm)	Energy (J/mm³)	Scan Strategy	Spot Size (μm)	Power (W)	Scanning Speed (mm/s)	Offset From Contour (mm)	Spacing Between Hatches (mm)	Energy (J/mm³)
P1	High Power, High Speed, Fixed Spot Size	100	370	1500	0.06	31	Diagonal stripes, 90° rotation every layer	100	370	2125	0.165	0.11	22
P2	High Power, High Speed, Fixed Spot Size, Contour Collapse	100	370	1500	0.06	31	Concentric circles filling towards center	100	370	2000	0.165	0.11	24
P3	Low Power, Low Speed, Fixed Spot Size	100	250	400	0.06	80	Diagonal stripes, 90° rotation every layer	100	278	1275	0.165	0.11	28
P4	High Power, High Speed, Variable Spot Size, Contour Collapse	50	219	1000	0.035	111	Concentric circles filling towards center	100	370	2000	0.115	0.11	24

Figure 16. Specimens Selected for CT Characterization

For each type of build geometry (cylinders, half sections of the longer cylinders and plates) the Empirical Cumulative Distribution Functions (ECDF) were plotted. Additionally, the sphericity of the defects were plotted as a function of defect diameter and aspect ratio respectively. Surface roughness measurements were taken at different locations of the specimens in order to capture the variation in surface quality. Figure 17 shows an example comparison of defect size distribution and defect morphology with surface measurements. The variation of sphericity is shown as a function of both defect diameter and aspect ratio. The first type of plot helps identify the morphology of the largest sized defect in the population. Literature sphericity values of 0.7 or greater correspond to gas porosity type defects, while lower sphericity values correspond to linear LOF type defects.
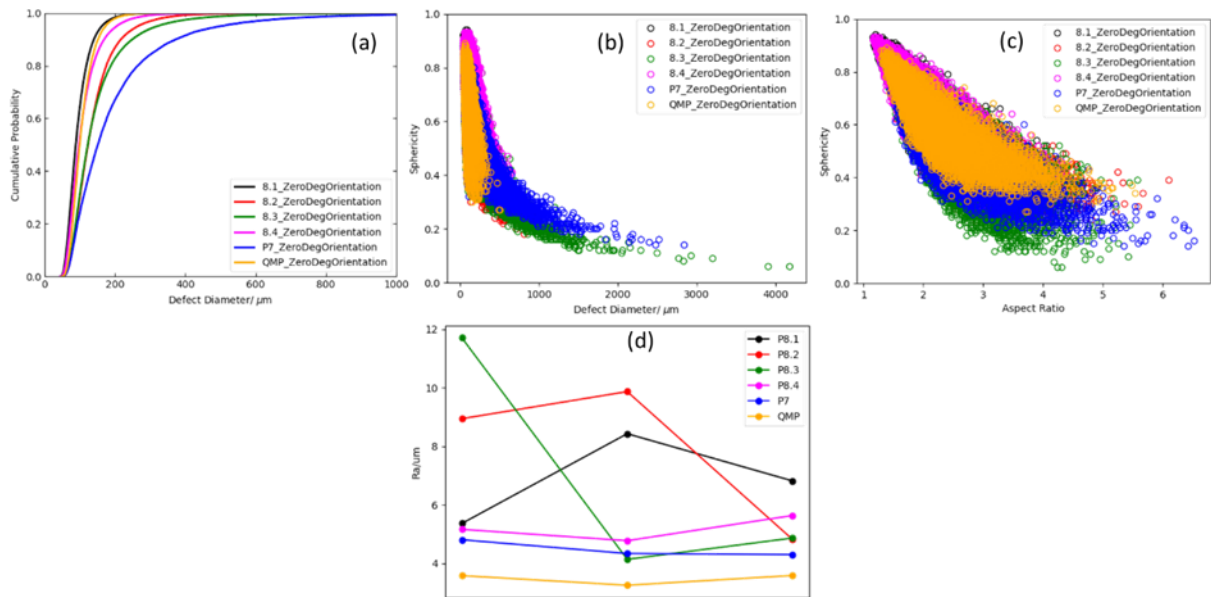
Figure 17. *Cylindrical Specimens Fabricated at 0° Build Orientation*
(a) ECDF plot of defect size, (b) and (c) show the variation of sphericity as a function of defect size and aspect ratio respectively. (d) shows the surface roughness (R_a) collected from three points on the specimen

From Figure 17c, it can be seen that the predominant type of defect in the population for the 0° build orientation cylindrical specimens is LOF type. The largest size defects, however, appear to be gas porosity type as seen from Figure 17b. From the ECDF plot and surface measurement data it can be seen that the builds corresponding to QMP are well optimized for minimizing defects and good surface quality.

Predominance of LOF type defects is also observed for the cylindrical specimens fabricated at 45 and 55 degree build orientations. A marked deterioration in surface quality can also be seen on the downskin surfaces of the specimens, when compared with the upskin surfaces.

The sphericity plots for the flat plate specimens show a larger percentage of gas porosity type defects in the population. Again, the downskin surface quality tends to be worse than the upskin for the 45 and 55 degrees build orientation specimens, similar to the cylindrical specimens.

A clear correlation between surface roughness and defect distribution could not be established, although it was seen in several instances that specimens with smaller defect size distributions tend to correspond with better surface quality in the as-fabricated condition. For both cylindrical and flat

plate types of specimens fabricated using 45 and 55 degree build orientations, the surface quality on the downskin surface was worse than the upskin surface. One likely reason for this variation is the difference in heat dissipation, resulting in adherence of powder particles on downskin surface. The QMP used at Eaton, seem to be well optimized to minimize defects and render good surface quality generally. Based on the observation of defect morphology, LOF type defects are more predominant in the cylindrical specimens, while larger population of gas porosity defects are seen in the flat plate specimens. A more extensive set of surface roughness and defect distribution data needs to be collected for future work to better understand the correlation between the two parameters – given that it is well known that poor surface quality coupled with large defect size distribution in components lead to sub-optimal fatigue properties.

3.2 Optimized Post-Processing Techniques for Improved Surface and Fatigue Performance of AM Alloy

3.2.1 Introduction

This section summarizes work performed to quantify the effect of specimen thickness and surface condition on the HCF performance of binder jet produced 17-4 PH (UNS S17400, SUS630) in the HIP and heat treated H900 condition. Mechanical test specimens were produced at four as-fused thicknesses of 0.5, 1, 2, and 4mm and covering three surface conditions, as-grown, machined, and lightly (0.001-0.002" per side) chemical milled. Tensile and fatigue tests were performed and frac–tography used to measure originating defect size on a subset of specimens. Metallurgical sections and high-resolution micro-CT were used to characterize surface defects. A simple numerical fatigue crack growth model specific targeting mechanically small crack behavior was assembled and used to extract implied defect size based on measured fatigue life. The implied sizes were compared with measured size and for similar surface condition specimens (as-grown, lightly chemical milled), found to be in reasonable semi-quantitative agreement. The model was unable however to simul–taneously accommodate machined specimens without a change in model constants. It was concluded that broadly different defect structures lead to differences in fatigue behavior that were beyond the capability of the model as implemented.

While promising to be a low-cost AM technique, binder jetting is also the least characterized of the powder bed fusion processes. The risk of unknown material performance is a deterrent to its use, in particular for demanding products such as dynamic seals where unknown material performance combined with the parts intricate geometry and dynamic loading could lead to design failures. This project begins to address this risk by characterizing the fatigue performance of binder jet produced 17-4 over a range of specimen thicknesses and surface conditions appropriate to Eaton's East Providence hydrodynamic seals. Other products will also benefit from this data.

3.2.2 Scope

This work was bounded by the following scope:

1. Single alloy specified as 17-4 PH (UNS S17400, SUS630).

2. Binder jet process executed by a single fabricator (Azoth) using a single machine platform (Desktop Metal (DM) SHOP System).

3. All specimens produced on a single build with the primary specimen material axis aligned with the machines *X* axis.

4. Use of a single standard sintering process specified by the fabricator and machine for 17-4 PH.

5. Use of a single standard HIP and H900 heat treat regimen practiced by a single HIP (Paulo – Cleveland, OH) and heat treat vendor (Vac-Met – Ann Arbor, MI).

6. Flat specimens grown to nominal thicknesses of 0.5, 1, 2, and 4mm. A small complement of cylindrical specimens grown to nominal 15mm diameter.

7. Flat fatigue specimens tested under three surface conditions: as-grown, machined, and very light (0.001-0.002" per side) chemical milling.

8. Specimen geometry conforming to ASTM E8 and E466 with a majority of the specimens being flats and a limited number of cylindrical specimens run for reference. Total specimen count of approximately 144 flats and 16 cylinders.

9. Data collection and analysis covering primarily two experimental variables – as-grown plate thickness (0.5, 1, 2, and 4mm) and surface condition (as-grown, machined, and light chemical mill).

10. "As-grown" surface flat specimens had their thinner edges profile milled. Only the wide surfaces of these specimens were retained in the as-grown condition.

11. Chemical milling restricted to one vendor (PAC) and a single, very light (removal of ~ 0.0015" per side), chemical milling operation.

12. Defects and microstructure characterized as "representative". Aside from post-test fractography, there was no attempt to perform a one-to-one mapping of specific specimen defects or surface condition to same specimen mechanical performance.

3.2.3 Specimen Fabrication

Specimens were fabricated in a single build by Azoth 3D LLC using a DM SHOP System. Stock DM 17-4PH parameters were used with a deposition layer thickness of 50 microns. Although Azoth stated that the 17-4 PH feedstock is considered infinitely recyclable, the feedstock used in this work was virgin powder.

The build plate layout was as shown in Figure 18, Figure 19, and Figure 20. In total, (192) flats, 48 of each thickness 0.5, 1, 2, and 4mm, (20) 15mm constant diameter cylinders, and (4) 15mm x 15mm x 80mm metallurgical blocks were grown and processed. All specimens except the metal–lurgical blocks were grown with their major material axis aligned with the machines X axis, their width with the Y axis, and thickness in the Z machine direction. Metallurgical blocks were grown with vertical Z axis orientation. Nominal scaling factors were applied to all part geometries prior to the build to accommodate for shrink during sintering. Dimensional measurements on a few specimens after sintering showed that nominal dimensions had been achieved.

All horizontal specimens were grown, transferred, and sintered resting on carrier blocks to minimize unbalanced shrinkage forces and possible distortion during sintering. Visual inspection of the specimens after sintering showed the specimens to be essentially straight and flat.

Flat specimens were grown as individual coupons with a constant rectangular cross-section. This required that even specimens designated for test in the as-grown surface condition be machined on their thin edges to achieve the required "dog bone" profile for test. This is believed to be a small but

nevertheless noteworthy concession to the as-grown surface test results. In general, machining was performed after all thermal treatments were complete.
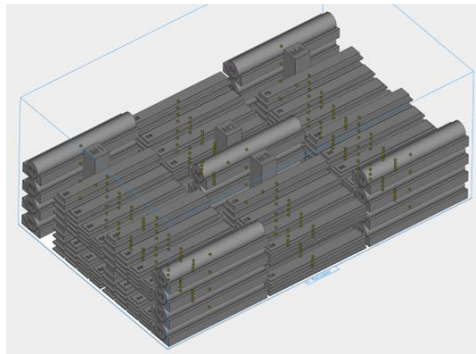
Figure 18.   Build Plate Layout – Full Plate View
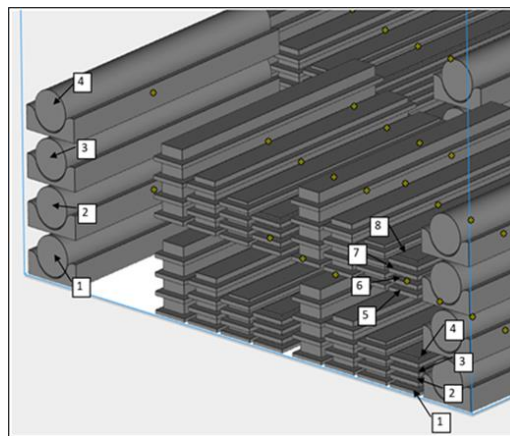
Figure 19.   Oblique View Showing Recurring Elevation Numbers
Each specimen rests on a carrier plate used to prevent warpage during sintering
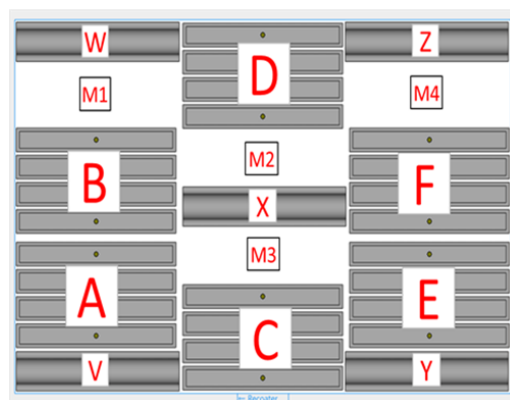
Figure 20.   Top-Down View Showing XY Group Arrangements
Each group contains four stacks, one stack for each thickness

3.2.4 Thermal Treatments

Except for a subset of metallurgical specimens, all mechanical test specimens were taken through a 3-step thermal treatment process as described in Table 2.

Cure, devolatilization, and sintering was performed at Azoth in an Elnik MIM3015 oven. Specimens were then visually inspected by Eaton and forwarded to a HIP process. Following HIP, specimens were again visually inspected and then sent through a H900 solution anneal, quench, freeze, and age process at Vac-Met in Ann Arbor, MI. Additional specifics are provided in Table 2.

Visual inspection of the flat bars after sintering showed them to be visually straight and in general conformance with expected dimensions. After HIP, the 0.5 and 1mm specimens showed significant warp, for some specimens up to several specimen thicknesses in total deviation. Similar levels of warpage were observed after full heat treat.

While specimen bow will cause bending stresses during test, the thin nature of these specimens reduces the magnitude of those stresses. As a result, it was decided to continue with processing and test as originally planned.

Figure 21 shows a subset of the specimens as observed after each of the thermal treatment steps.

Table 2. Thermal Treatment Process

Step	Process
1. Cure, Devolatilize, Sinter	• Polymer cure at 200°C for 48 hours in air. • Devolatilize (Debind) during ramp to 500°C, hold at 500°C for 2 hours, then ramp to 1370°C. • Sinter at 1370°C for 4 hours in pure hydrogen atmosphere.
2. Hot Isostatic Press	• Heat in Argon to 2050 ± 25°F at 15 ksi ™ 0.25 ksi and hold for 4 hours, -0/+15 minutes. Then cool under pressure to 400°F.
3. H900 Heat Treatment	• Solution Anneal in Vacuum @ 1900ºF ± 25ºF hold at heat for 60-70 minutes, then hydrogen gas quench, cooling to below 90ºF within one hour of quench. • Freeze @ -100°F to -120°F ± 10°F tolerance at selected temperature for 1-2 hours only. • Age in Vacuum of 1 x 10-3 Torr or better at 900ºF ±10ºF for 1 hour +15/-0 minutes and Argon or Nitrogen Gas Quenched.

Figure 21.   Representative Specimens
  a) After sintering but before HIP and heat treatment; b) After HIP; c) After HIP and H900 heat treatment

3.2.5 Specimen Geometry

Mechanical test specimens were grown as constant cross-section rectangular bars (flats) or constant diameter cylinders. Overall, 20 cylinders and 192 flats were grown to a nominal diameter of 15mm

and nominal thicknesses of 0.5, 1,2, and 4mm, respectively. All mechanical test specimens were machined to final shape after all thermal processes were executed.

All flat tensile and fatigue specimens were machined to the same profile (gage width and length) geometry. The as-grown (AG) and remedial surface chem milled (Rm1) specimens were profile milled on their narrow edges but left unmodified on the 6/10mm wide surfaces. The machined and polished (M&P) flats had their profile surfaces milled; thereafter, all four surfaces were longi–tudinally polished. Note that the 6/10mm wide surfaces of the M&P specimens were not milled prior to polishing. This led to a major deficiency in the M&P flats. The polishing process was not sufficiently controlled to remove all the as-grown surface defects which led to poor fatigue performance (relative to the fully machined cylinders) during subsequent fatigue tests.

Cylinders were turned and longitudinally polished to two different profile geometries – tensile specimens and fatigue. The fatigue specimens used a shorter gage length to allow for fully reversed loads (R=-1) without fear of buckling. Overall, the turned and polished (T&P) specimens showed no issues with remnant as-grown surface defects because a significant amount of stock was removed during turning.

Metallurgical specimens were cut as needed from vertically grown 15mm x 15mm x 80mm blocks M1 through M4, dispersed over the area of the build.

3.2.6 Chemical Milling
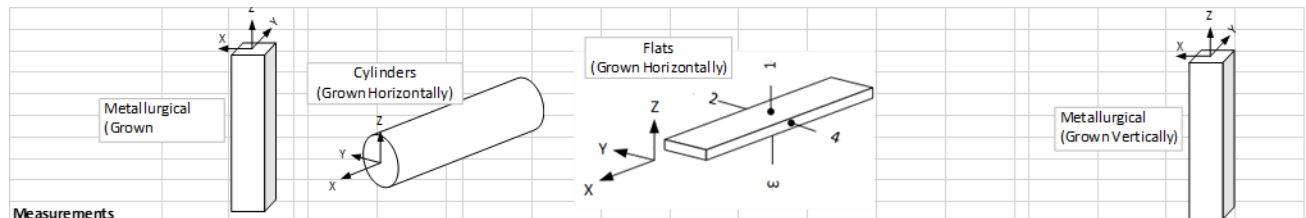
A subset of 48 flat specimens were treated to light chemical milling. The purpose of these specimens was to determine if even small amounts of chemical milling can provide a beneficial effect in fatigue performance.

Chemical milling was performed prior to final machining (cutting of the profile dog bone shape) by Precision Aerospace Corporation (PAC) in Rancho Cucamonga, CA. The specified target removal amount was 0.002" to 0.004" across the specimen thickness (~0.0015" per side). All specimens were measured by PAC before and after processing at two locations on opposing tabs of the specimen to avoid any marring in the specimens gage area. Analysis of the collected thickness data showed an overall average removal of 0.0031" with standard deviation of 0.000495". Differences in the amount of material removed across the different nominal thickness groups were reasonably small. On average 0.0030", 0.0035", 0.0028" and 0.0029" was removed for the 0.5, 1, 2, and 4mm specimens respectively. Differences in removal between the thickness groups were not statistically different except for the 1mm specimens which showed the highest overall removal rate.

3.2.7 Vickers Hardness

Vickers hardness was measured across all specimen types (metallurgical bars, cylinders, flats), heat treat conditions (as-grown, HIPed, H900), and material orientations (longitudinal, transverse). The H900 flats, in particular the 0.05mm thick flats, were found to be the hardest of any the specimen groups and at the upper range of what typically is reported for 17-4 in the H900 condition. The as-grown (or as-sintered) hardness was in line with values typically reported for 17-4PH in the "A" (mill annealed) condition. Finally, the HIPed specimens showed the lowest hardness, slightly below the as-sintered specimens. A summary of the data and summary statistics are given in Table 3.

Table 3. Vickers Hardness Measurements

Spec Type	Metallurgical		Cylinders		Rectangles											
Spec #	M1	M1	X1	X1	A2	A2	A2	A2	A2	A2	A2	A2	M2	M2	M3	M3
HT Cond	H900	H900	H900	H900	H900	H900	H900	H900	H900	H900	H900	H900	AG	AG	HIP	HIP
Thickness (mm)	15	15	15	15	0.5	1	2	4	0.5	1	2	4	15	15	15	15
Orientation (geom)	trans	long	trans	long	trans	trans	trans	trans	long	long	long	long	trans	long	trans	long
Mat'l Plane	yz,xz	xy	xy	yz,xz	xy	xy	xy	xy	yz,xz	yz,xz	yz,xz	yz,xz	yz,xz	xy	yz,xz	xy
	449	463	467	450	485	460	453	467	460	433	456	449	381	378	351	333
	467	452	467	467	474	456	456	452	460	453	456	459	351	380	348	344
	456	456	463	453	478	449	463	463	456	449	453	459	344	383	358	360
	463	449	474	443	474	412	456	440	467	463	439	421	380	383	351	356
	414	467	471	423	485	460	443	453	456	466	470	436	386	381	339	329
	460	460	463	411	485	446	449	443	456	449	453	443	380	375	351	348
Statistics																
Per Spec & Orient																
Min	414	449	463	411	474	412	443	440	456	433	439	421	344	375	339	329
Max	467	467	474	467	485	460	463	467	467	466	470	459	386	383	358	360
Range	53	18	11	56	11	48	20	27	11	33	31	38	42	8	19	31
Ave	451.5	457.8	467.5	441.2	480.2	447.2	453.3	453.0	459.2	452.2	454.5	444.5	370.3	380.0	349.7	345.0
SD	19.4	6.8	4.4	20.6	5.5	18.2	6.8	10.6	4.3	11.8	9.9	14.6	18.0	3.1	6.2	12.3
CoV	4.3%	1.5%	0.9%	4.7%	1.1%	4.1%	1.5%	2.3%	0.9%	2.6%	2.2%	3.3%	4.9%	0.8%	1.8%	3.6%

3.2.8 Surface Roughness

3D optical surface measurements were taken from a subset of flat specimens representing the as-grown, polished, and light chemical milled state. Sampled specimens were measured in four locations, one location per side, near each specimen's mid-length (Figure 22). Fully machined and polished specimens were measured after mechanical testing. For these specimens, the measurements were taken 3-5mm away from the failure location to avoid the influence of any localized damage.
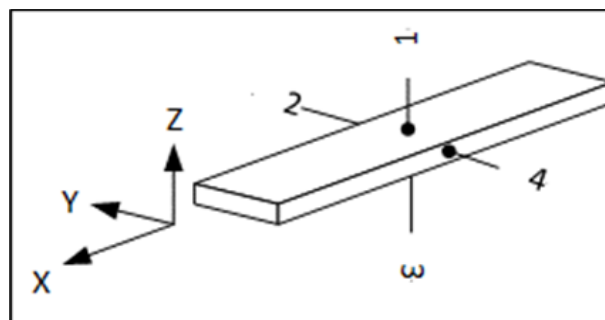
Figure 22.   Surface Roughness Measurement Locations

Table 4 shows how four specimens, one per nominal thickness, changed in roughness following the chemical milling process.

The changes in roughness are aligned with reported total removal rates. The thinner 0.5 and 1mm and 2mm specimens tended to show a greater and higher statistical significance in measured change than did the thicker 4mm flats.

Table 4. Change in Roughness Before and After Chemical Milling

Surface / Specimen	Sa μm	Sv μm	Sz μm	Sz25 μm	Ssk	Sku	Ave Δthk (mil)
	Percent Change in Roughness Metric 100*(Chem Mill-AG)/AG						
1	-19%	39%	19%	-9%	-7600%	27%	
2	-15%	-28%	-26%	-21%	-13%	-21%	
3	-24%	-10%	-23%	-23%	-165%	-1%	
4	-30%	-27%	-28%	-29%	-390%	12%	
B6-.5mm	**-22%**	**-7%**	**-15%**	**-20%**	**-2042%**	**4%**	**3.0**
1	-6%	-19%	-23%	-8%	-52%	-5%	
2	-17%	-14%	-18%	-21%	57%	5%	
3	-22%	-21%	-27%	-27%	267%	-6%	
4	-37%	-46%	-38%	-38%	-10100%	3%	
B6-1mm	**-20%**	**-25%**	**-26%**	**-24%**	**-2457%**	**-1%**	**3.5**
1	1%	-4%	-3%	6%	-82%	-2%	
2	12%	-26%	-13%	2%	-61%	-10%	
3	-18%	-36%	-24%	-21%	-108%	-9%	
4	-23%	-19%	-11%	-11%	-1878%	19%	
B6-2mm	**-7%**	**-21%**	**-13%**	**-6%**	**-532%**	**-1%**	**2.8**
1	20%	-14%	-9%	-1%	-1211%	-24%	
2	0%	25%	14%	-1%	862%	17%	
3	-19%	-25%	-21%	-18%	-77%	3%	
4	-7%	-2%	-9%	-11%	38%	-21%	
B6-4mm	**-1%**	**-4%**	**-6%**	**-8%**	**-97%**	**-7%**	**2.9**
Ave across (4) B6 Specimens	**-14%**	**-16%**	**-16%**	**-15%**	**-375%**	**-2%**	**3.1**

3.2.9 Metallurgical Sections

Six cross-sections – (3) 0.5mm and (3) 4mm thick flat specimens, were cut, polished, and inspected for surface connected crevice depth. Depth was measured as the distance from the nearby "mean" surface to the deepest visual indication. For these measurements, the mean surface was visually estimated as the cutting plane having approximately 50% solid material. Roughly 70% of each specimen's perimeter was inspected and only defects deeper than roughly 20 microns were recorded.

Prior to data analysis, each image was reviewed, and defects further segregated into those for which evidence showed they were surface connected (Type 1) and those for which the visual evidence was weak to nonexistent (Type 2). While many of the Type 2 defects may also have been surface connected, this separation was performed to eliminate any remnant interior voids and provide consistency with CT surface analysis.

A box plot of the Type 1 defects is provided in Figure 23. The graph shows little to no difference in crevice depth due to surface orientation (1=up, 3=down) but some weak difference due to specimen thickness. Simple T tests show the significance of this marginally dependance in Table 5.

Why thickness should matter is not clear. Additional sampling across the build would be required to determine if this effect is real or an artifact of the limited sampling performed (location within the build, *X-Y* or *Z* height?)
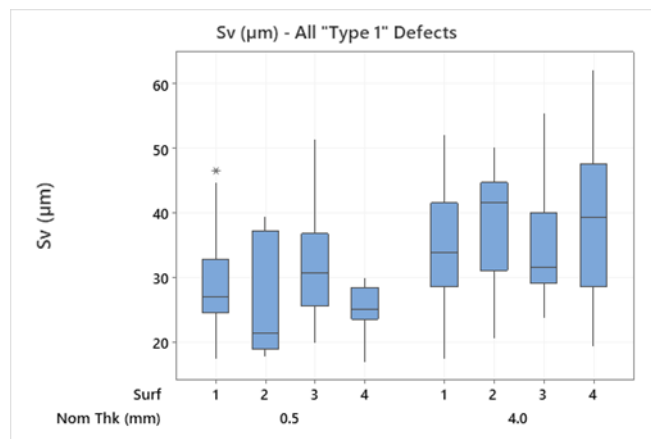
Figure 23. Box Plot of Surface Connected (Type 1) Defects

Table 5. 2T Tests for Statistical Differences

Diff btwn .5 & 4mm?	T.test P-Value	.5mm ave μm	4mm ave μm	Concl.
for surf 1	0.00637	29.34	36.84	marginal?
for surf 3	0.13310	31.43	34.32	no
all surfaces	0.00000	29.58	36.56	yes
Diff btwn Surf 1 and 3?	T.test P-Value	Surf1 ave μm	Surf2 ave μm	Concl.
across both thickness's	0.94989	33.03	32.92	no
.5mm thk specimens	0.27363	29.34	31.43	no
4 mm thk specimens	0.34214	36.84	34.32	no

The deepest Type 1 defects, one from each specimen and surface (24 data points in total) were then combined into a single population to assess the applicability of various distributions and extract an extreme value statistic. The results are shown in Table 6 and Figure 24.

It's interesting to note that average of the maximum crevice depths CD(50,50) were different for the 0.5mm and 4mm specimens but that the 99% projections CD(95,99) are very much alike. Although very similar to the normal, Weibull, the extreme value distribution provided the largest CD(95,99) numbers. Taking the extreme value numbers as the best representation of the data, suggests that at least 66μm (0.0026") would need to be removed from the mean surface (0.0052" peak to valley) to fully remove 99% of the deepest defects.

Table 6. Distribution Tests for Metallurgical Crevice Depth, 0.5mm & 4mm Thickness

.5mm Specimens, All Surfaces, Type 1 Corrected						4mm Specimens, All Surfaces, Type 1 Corrected					
Distribution	AD	P	LRT P	CD(50,50)	CD(95,99)	Distribution	AD	P	LRT P	CD(50,50)	CD(95,99)
Normal	0.131	0.973		35.97	58.38	Normal	0.357	0.392		50.55	62.93
Box-Cox Transformation	0.133	0.971				Box-Cox Transformation	0.306	0.515			
Lognormal	0.26	0.644				Lognormal	0.318	0.49			
3-Parameter Lognormal	0.146	*	0.225			3-Parameter Lognormal	0.435	*	0.187		
Exponential	3.036	<0.003				Exponential	4.515	<0.003			
2-Parameter Exponential	1.439	<0.010	0			2-Parameter Exponential	0.359	>0.250	0		
Weibull	0.139	>0.250		36.39	55.45	Weibull	0.51	0.19		50.57	62.06
3-Parameter Weibull	0.14	>0.500	0.949			3-Parameter Weibull	0.308	>0.500	0.015		
Smallest Extreme Value	0.178	>0.250				Smallest Extreme Value	0.624	0.09			
Largest Extreme Value	0.278	>0.250		34.61	73.06	Largest Extreme Value	0.352	>0.250		49.64	66.46
Gamma	0.206	>0.250				Gamma	0.35	>0.250			
3-Parameter Gamma	1.914	*	1			3-Parameter Gamma	0.32	*	0.152		
Logistic	0.157	>0.250				Logistic	0.341	>0.250			
Loglogistic	0.216	>0.250				Loglogistic	0.329	>0.250			
3-Parameter Loglogistic	0.158	*	0.359			3-Parameter Loglogistic	0.401	*	0.262		
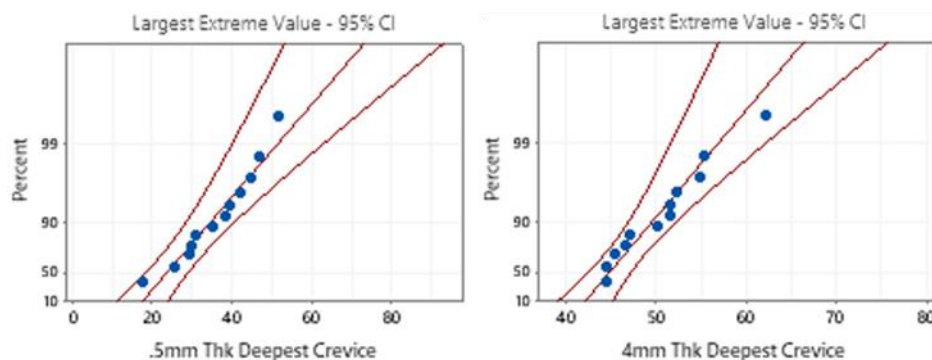
Figure 24. Graphical Fits for Largest Extreme Value Distribution

3.2.10 CT X-Ray

Similar to the metallurgical sections, CT x-ray data was collected and compared with the cut section data. Initial scans were acquired from a Lumafield Neptune CT with roughly 80µm resolution, but the resolution was found to be inadequate. The work was then moved to a Versa 520 micro CT at the University of Michigan Center for Materials Characterization. This machine offered excellent 1-2µm resolution but at the expense of scan volume and number of parts that could economically be processed. As a result, only one AG surface specimen, A7-.5mm, was scanned. The implied assumption is that A7-.5 is representative of all specimens in this build.

Due to scan size restrictions, a scan volume was chosen that was roughly centered in the part and included the specimens full 0.5mm thickness but only about 1mm of width and length (depth of scan). Capturing the full thickness provided two free surfaces, the AG top and AG bottom, for inspection. After acquiring the volume file, it was reviewed and a subset of (15) 2D slices chosen for further processing. Slices were chosen in an attempt to capture the deepest observed crevices yet with some distance between each slice so as to capture new defects. Similar to the cut sections, processing the slices involved manually choosing surface "midplanes" and measuring the deepest crevice depth relative to the midplane. The deepest crevice for the top and the bottom surface was measured.

Midplanes were chosen to be geometrically centered between the highest peak and deepest crevice for each surface and slice. This was somewhat different to the approach used in the metallurgical sections where 50% solid material was used as the midplane criterion and would be expected to lead to some mean offset in the results. In general, the CT midplanes likely resulted in some under reporting of the deepest crevices.

Figure 25 is a box plot of the 2D slice data. Unlike the metallurgically derived results, the CT data shows a difference in mean crevice depth between the top and bottom surfaces (see the confirming 2T test in Table 7). Interestingly, the deepest crevice across all slices was about the same for the top and all bottom surfaces. Because of the implied differences in distribution, analysis for distribution fit and extreme values was calculated separately for each surface and Table 8 summarizes those results.

As with the metallurgical data, reasonable fits were found using normal, Weibull and extreme value distributions. Also as with the metallurgical data, the extreme value distribution yielded the highest Confidence on Distribution, CD(95,99) values.
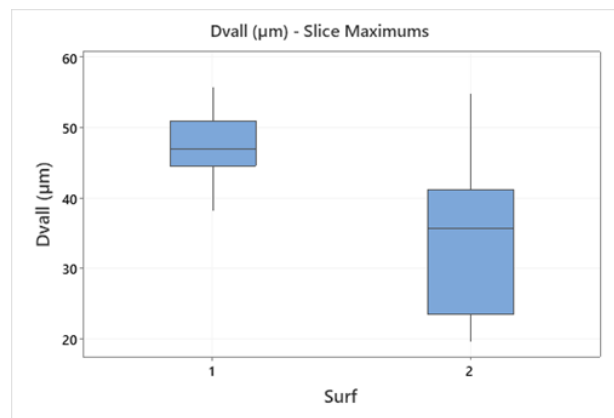
Figure 25.   Box Plot of CT Derived Surface Connect Defects

Table 7. 2T Test for Statistical Difference

	T.Test P-Value	Dv1 Ave (µm)	Dv2 Ave (µm)	Concl.
Diff. btwn Dv1 and Dv2?	0.00017	47.74	33.92	yes

Table 8. Distribution Tests for Metallurgical Crevice Depth, -Z & +Z Surfaces

A7-.5mm, Surface Connected Defects, Surface #1 (-Z during Fab)						A7-.5mm, Surface Connected Defects, Surface #3 (+Z during Fab)					
Distribution	AD	P	LRT P	CD(50,50)	CD(95,99)	Distribution	AD	P	LRT P	CD(50,50)	CD(95,99)
Normal	0.201	0.855		47.74	63.29	Normal	0.3	0.537		33.92	68.98
Box-Cox Transformation	0.184	0.892				Box-Cox Transformation	0.321	0.502			
Lognormal	0.246	0.708				Lognormal	0.339	0.451			
3-Parameter Lognormal	0.21	*	0.459			3-Parameter Lognormal	0.392	*	0.91		
Exponential	5.672	<0.003				Exponential	3.424	<0.003			
2-Parameter Exponential	2.048	<0.010	0			2-Parameter Exponential	0.639	0.194	0		
Weibull	0.211	>0.250		48.28	59.62	Weibull	0.302	>0.250		34.05	68.8
3-Parameter Weibull	0.196	>0.500	0.567			3-Parameter Weibull	0.446	0.299	0.108		
Smallest Extreme Value	0.247	>0.250				Smallest Extreme Value	0.475	0.226			
Largest Extreme Value	0.451	0.25		47.11	75.5	Largest Extreme Value	0.391	>0.250		32.15	86.32
Gamma	0.235	>0.250				Gamma	0.337	>0.250			
3-Parameter Gamma	2.849	*	1			3-Parameter Gamma	0.33	*	1		
Logistic	0.21	>0.250				Logistic	0.318	>0.250			
Loglogistic	0.229	>0.250				Loglogistic	0.381	>0.250			
3-Parameter Loglogistic	0.21	*	0.568			3-Parameter Loglogistic	0.391	*	0.957		

Across the distributions, mean CD(50,50) defect sizes of 32 and 48µm for -Z and +Z surfaces were similar to the values determined by sectioning, 36 and 51µm for the 0.5mm and 4mm specimens, respectively. The CD(95,99) results were also similar with the extreme value distribution numbers somewhat higher for the +Z facing surface, CD(95,99) = 86µm for the +Z surface than the same thickness sectioned data of CD(95,99) = 73µm.

Given the differences in sampling and technique, the differences in measured defect depth are small. This suggests that either method can be used to extract this information. The similar results also provide evidence that the measured values are in fact reasonably accurate.

Besides information on depth, the CT volume file also provides rich insight into the interconnected–ness of the surface defects. Many of the near surface defects that appear to be isolated in 2D slices are in fact connected at some point to the parts free surface. This interconnectivity and access to the free surface explains why HIP is ineffective in eliminating these defects.

3.2.11 Tensile and Fatigue Testing

Twelve AG flats (three per thickness), 12 M&P flats (three per thickness), and five T&P cylinders were pulled to failure using an optical extensometer to approximately 1% total strain, and frame displacement thereafter. The recorded data was then used to extract ultimate tensile strength (UTS), 0.2% yield strength (YS) and elongation at break.

All specimens failed within their gage length with a few of the flats near the transition between gage and grip radius. All tests were deemed valid.

A graphical summary of the data as a function of the nominal as-grown thickness is given in Figure 26. In these graphs the 0.5, 1, 2, and 4mm thickness specimens are the flats, the 15mm blanks became the T&P cylinders. The low variability of the T&P cylinders is immediately apparent. The cylinders show tight distributions and mean values for 0.2% YS, UTS, and elongation that are very near the values reported in MMPDS-04 for 17-4 wrought bar in the H900 condition (Table 9).

Statistics	0.5	1.0	2.0	4.0	15.0
N	6	6	6	6	5
Mean	165.7	167.78	166.88	166.87	169.78
StDev	21.921	12.396	6.9032	5.5403	0.97314
Minimum	137.1	155.2	159.3	160.5	168.3
Maximum	189.7	184.5	174.4	172.6	170.7
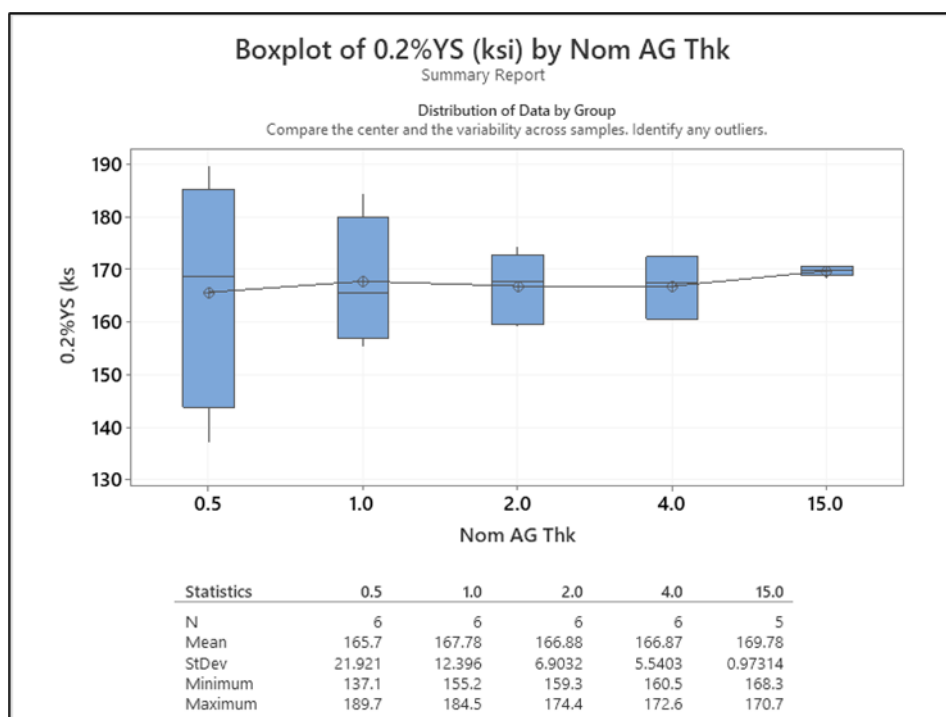
Figure 26.   Tensile Results Across All Specimen Thicknesses Compared

Table 9. Cylinder Tensile and MMPDS Results Compared

Source	BJ 17-4	BJ 17-4	BJ 17-4	MMPDS	Diff (%)
Basis	σave	SD	"S"	"A"	("S"-"A") /
			σave-3SD		"A"
HT	H900	H900	H900	H900	
Form	T&P Cyl	T&P Cyl	T&P Cyl	Bar	
Orientation	Z	Z	Z	L	
E (Msi)	29.4	0.65	27.5	28.5	-4%
0.2%YS (ksi)	169.78	0.87	167.2	170	-2%
UTS (ksi)	194.64	0.26	193.9	190	2%
ε_at_b (%)	16.0	1.10	12.7	10	27%

A graphical summary of the flat specimen data is provided in Figure 27. For the AG surface flats, all measures of tensile performance (0.2%YS, UTS, and e@b) increased as specimen thickness increased. Oddly, the same was not true for the machined flats. Here, strength (both 0.2%YS and UTS) decreased with increasing thickness.

A possible explanation for this behavior may be metallurgical condition, specifically differences in temperature and heating/cooling rates experienced during heat treat. The thinnest specimens, being most exposed, should show the greatest response to heat treatment. AG specimens, with high defect populations, may have shown degraded strength due to the lower ductility and greater defect sensitivity this condition imposes. In contrast, machined specimens (with fewer defects) may have shown higher strength due to a higher bulk material strength enabled by the thin-walled thermal conditions.

This behavior is aligned with both the higher specimen hardness and lower elongation at break measured in the AG and M&P, 0.5mm specimen populations. Additional metallurgical work would be needed to further confirm this theory.

Finally, it should be noted that the M&P specimens even at the 4mm thickness, were still higher in strength than their AG counterparts.
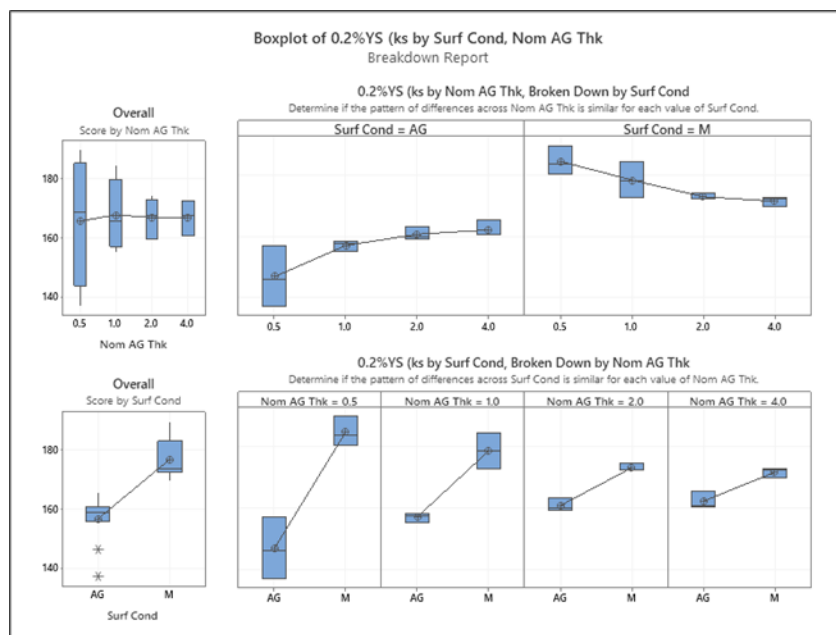
Figure 27.   Graphical Summary of Flat Tensile Results

Figure 28 presents the cylinder data and their combined fit for the two stress ratios (R) tested. In this image, solid symbols represent specimens run to failure, open symbols are terminated tests (run-outs). The specimens show excellent consistency as indicated by the tight clustering of duplicate specimens run in both the R=+.05 and -1 condition.

The fit was extracted using nonlinear regression and an equation of the form commonly used in the Metallic Materials Properties Development and Standardization Handbook. This was:

$$Log(N) = a1 + a2 * Log(Smax * (1 - R)^n - a3)$$

where

- a1, a2, n, and a3 are the extracted fit constants
- R is the stress ratio, Smin/Smax
- Smin and Smax are the minimum and maximum applied cyclic stresses, respectively.

In solving the above, a3 was constrained to be greater than the implied 1E7 cycle threshold of 65 ksi observed in these specimens. No other restrictions were applied. The fit was found to be relatively tight to the data with a maximum difference in log life of less than 4.5% for any single data point. Most points showed an error of only 1-2%.
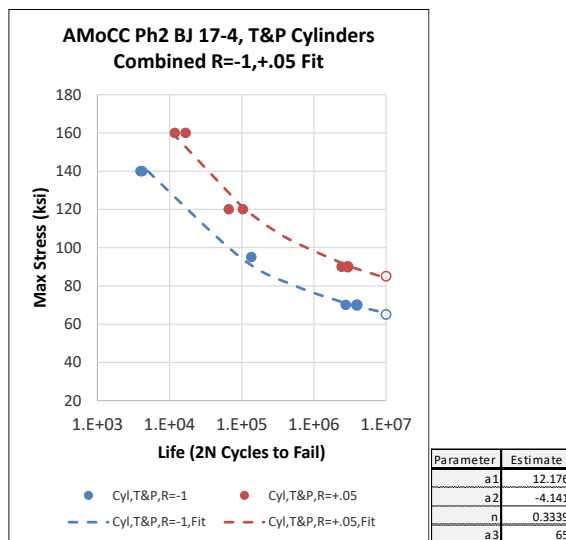
Figure 28.   HCF T&P Cylinder Data with Combined R Fit

Figure 29 shows the flat specimen data segregated by surface condition (three separate plots) with nominal (as-grown) thickness segregated within each plot. Simple power fits were added to these plots to help with visualization. Note that these are not design curves. A more thorough review and fitting process would be needed to meet that objective. The fit for the Rm1 specimens appear to be particularly poor and may be impacted by the limited stress range used for this surface condition. In general, scatter across the flat specimens was much higher than for the cylinders making extraction of quantitative outcomes more difficult. As a result, the focus here was on qualitative conclusions.

Some of the scatter may be explained by specimen distortion (or residual stresses) that occurred during the heat treat processes as discussed earlier. Another source of variability was sample pre–paration. This was especially true of the M&P flats. Like the AG and Rm1 specimens, the M&P parts were grown to near net shape and longitudinally polished on their 6/10mm wide surfaces without prior milling. Unfortunately, the polishing process was not sufficiently controlled leading to inconsistent and insufficient material removal. Failure origins were traced to remnant defects during fractography and essentially disqualified these specimens from representing the machined and polished state.

Qualitatively, the difference in fatigue performance between the AG and Rm1 surfaces was indiscernible suggesting that light chemical milling (0.0015" per surface) is not an effective technique to improve fatigue performance. Much higher rates of milling, upwards of 0.01 to 0.02" of removal would likely be needed to show significant improvement.
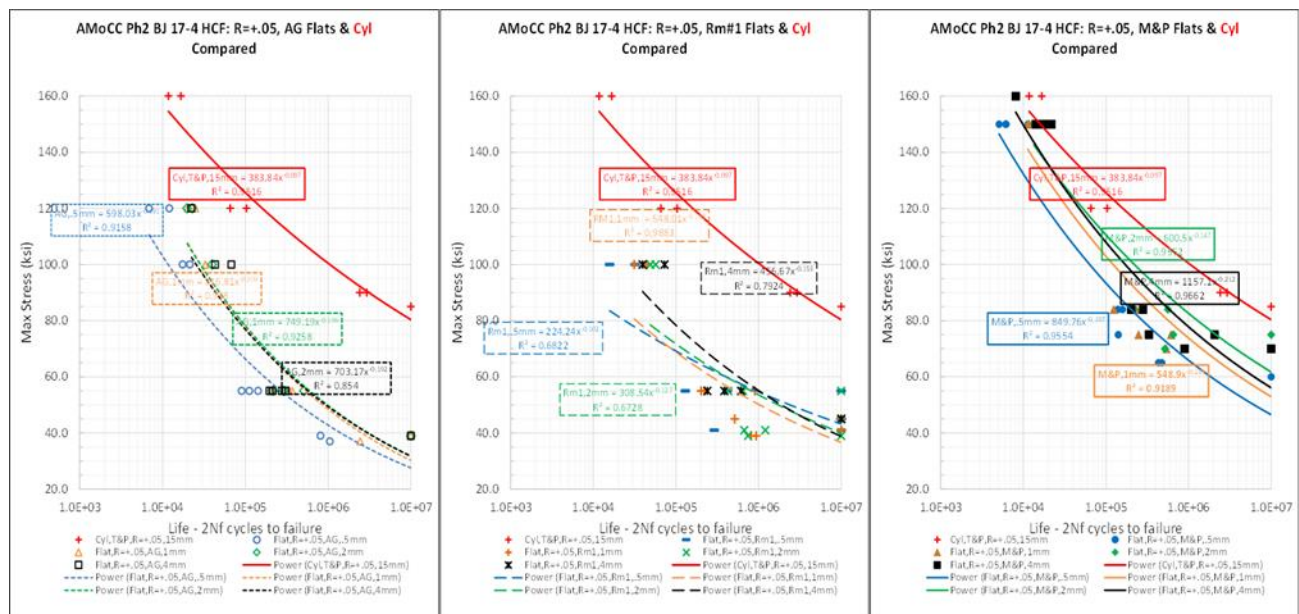
Figure 29. HCF Flats Fatigue Performance

With respect to thickness, the thinnest (0.5mm) specimens consistently showed the lowest fatigue life. For the other thicknesses, scatter within the data makes it difficult to discern any real differences. So qualitatively, it can be concluded that the average performance of the 1mm, 2mm, and 4mm specimens was roughly the same.

3.2.12 Fractography

Post-test fractography was performed on a subset of tensile and HCF specimens. For HCF, two (of 13) T&P cylinders, and 29 (of 136) flat specimens were examined. Here the fatigue fractography only is reported on.

With little to distinguish them in performance, one R=-1 and one R=+.05 low stress, high life cylinders were selected for examination. Flats were selected across the surface groups – AG, M&P, and Rm1 with preference within each group, given to either high or low life performers. Imaging involved low magnification optical and scanning electron microscopy under increasingly higher magnification. Both SE and BSE modes were used to help differentiate surface features. Where appropriate, energy-dispersive x-ray spectroscopy (EDS) was used to confirm the presence and elemental makeup of inclusions.

After imaging, individual images were reviewed to confirm crack initiation locations and extract relevant defect sizes. In general, the $a = \sqrt{A}$ methods of Murakami (Murakami, 2002) and teachings of Schönbauer (Schönbauer, 2020) were used to extract defect sizes with the following exceptions:

- A simple rhombus (four-sided parallelogram), ellipse, or half-ellipse for surface defects, was used to define defect boundaries and areas instead of free form shapes and the $\sqrt{10} * a$ method as developed by Murakami. Half-ellipses were used most frequently.

- Local fracture patterns rather than strict spacing rules were used to judge whether a group of defects were acting as a single large or multiple small defects.

Determining if closely grouped defects act collectively or individually is one of the difficulties associated with using the $\sqrt{A}$ method. Another is simply ignoring the effect 3D shape and orientation have on surrounding stress intensity. In this work, variation in shape and orientation are likely miti–gated in a statistical sense by the large number of similar surface defects present in the specimens. This leaves determining the "collective" or "effective" size of closely spaced defects is the largest likely contributor to variability in defect characterization.

Both of the examined cylindrical specimens showed fatigue cracks that originated at their surface, at a location also containing an exposed oxide inclusion. The inclusions were exposed at the time the specimens surface was machined. Slight surface imperfections associated with breakthrough at the inclusion may also have contributed to stress intensity, but the size of the local surface imperfections was small.

In contrast, all the flat specimens including the polished flats showed failures originating from surface crevice defects. Oxides and oxide inclusions were also observed at some surfaces and even some crack exposed interior locations, but in all cases, cracks only originated from external surfaces and where significant deviation in surface topography was also present. Specimens with surface or surface connected oxides included AG A7-1 and Rm1 C7-1, F5-.5, A8-.5, A8-2, F5-4. The Rm1 chem milled specimens had by far, the highest prevalence of surface oxides. This was consistent with the chemically aggressive baths these specimens were exposed to.

Interior inclusions were also observed in specimens AG C3-4, M&P B2-.5 and C1-2, and Rm1 C2-.5, and F3-1. Here passing cracks exposed the inclusions but the inclusions showed little to no interaction with the passing crack. A takeaway from these observations was that the oxides were much less harmful to fatigue than the surface topography from which the fatigue cracks originated.

In many specimens, closely spaced adjacent surface defects appeared to initiate multiple small cracks that quickly converged into a single larger crack front. AG Specimen A7-1 in Figure 30 shows such an instance. The degree of interaction (impact on stress intensity) at the time of crack started is unclear and gives rise to uncertainty as to what the "effective" size of the originating defect area was. As shown in Figure 30, the defect zone in this instance was treated as a single large defect with equivalent $\sqrt{A}$= 120µm.
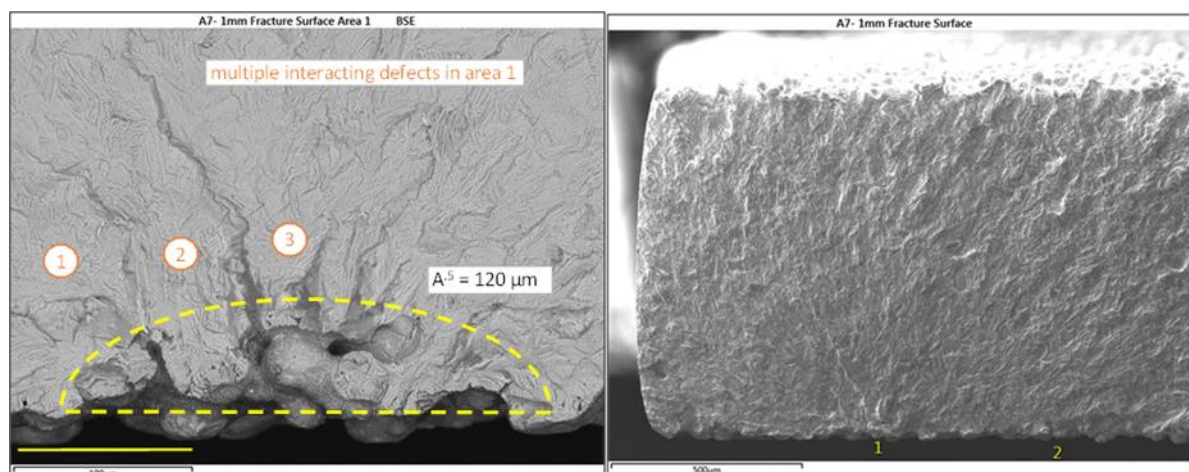
Figure 30.   Microcracks Emanating from Closely Clustered Surface Defects

Figure 31 shows the behavior of another AG specimen D4-.5mm. Here two distinct crack planes were formed. Combined defect area 1a imitated a crack that dominated over one portion of the specimen's cross-section while another distant defect location initiated a second crack that also grew to cover about one third of the cross-section. Final fracture occurred when the remaining uncracked material was insufficient to support the load. The amount of cross-section remaining at final fracture was approximately 50%. This was typical of all specimens, regardless of size and shape. The cross-section remaining at final fracture was usually in the range of 30-50%.
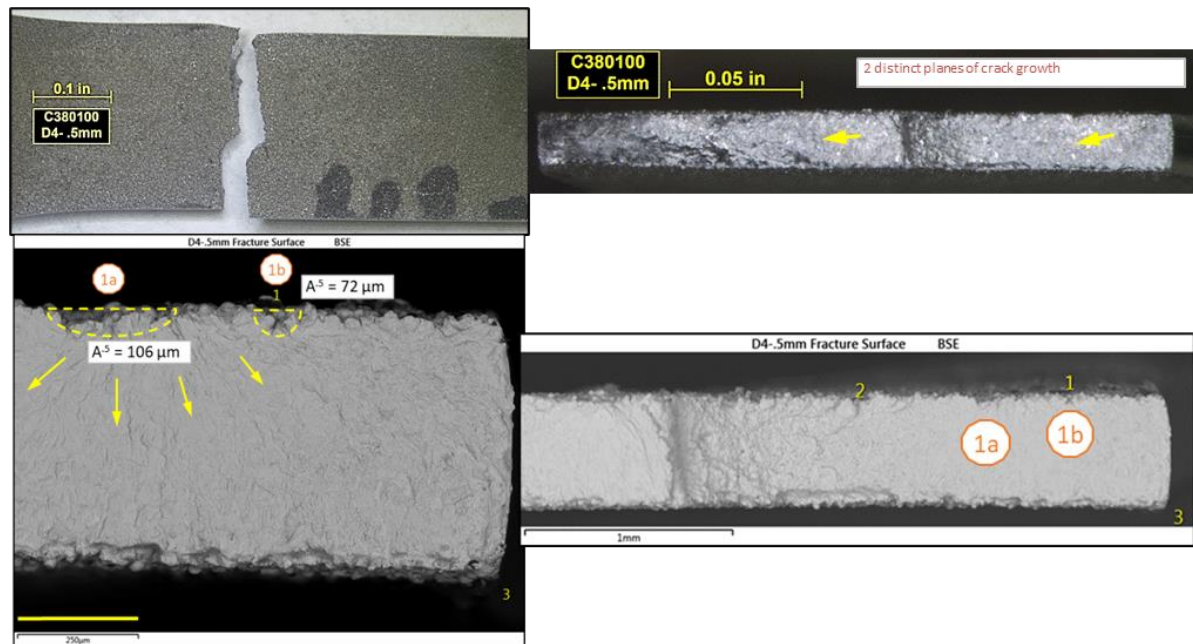
Figure 31.   Specimen Showing Two Distinct Crack Planes

The M&P flats showed significant populations of remnant surface crevices that were not fully removed in the polishing process. These remnant crevices were the source of all observed failures. As an egregious example, Figure 32 shows M&P specimen B2-.5mm that failed at its 10mm wide grip instead of the 6mm wide gage width. The failure is largely due to the diminish polish into the grip. Although an invalid test with respect to fatigue strength characterization, this specimen illustrates the impact remnants of the original surface defects still had on fatigue strength.
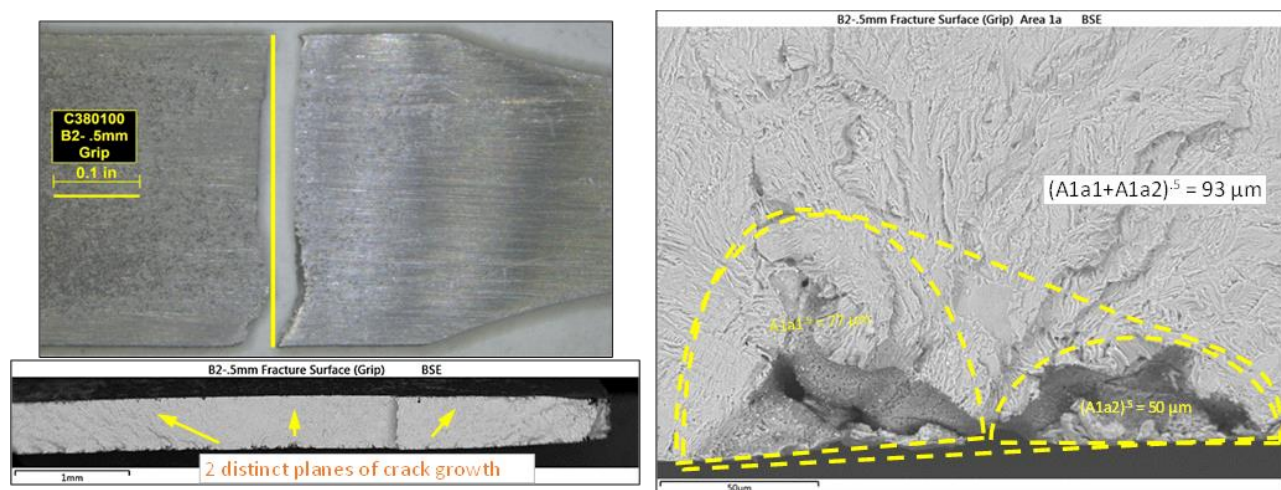
Figure 32.   M&P Specimen B2-.5mm

Figure 33 shows a second M&P specimen, in this case a more typical failure, but as with the others, this particular specimen also showed an interior inclusion that was uncovered by the passing crack front.
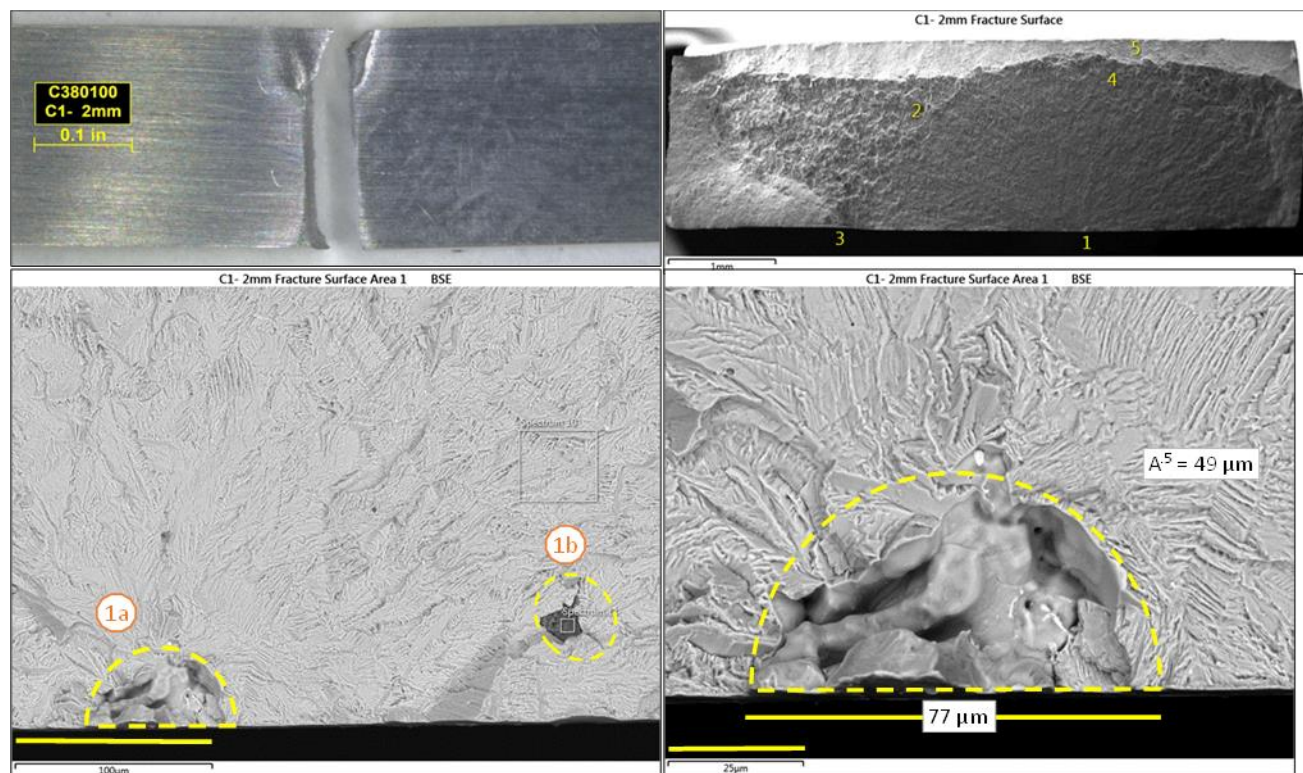
Figure 33.   M&P Specimen C1-2mm

3.2.13 Fatigue Crack Growth Model

Figure 34 compares the cylinder fatigue data (solid circles) with the combined R fit (dashed lines) and the Fatigue Crack Growth Rate (FCGR) model predictions. The FCGR model predictions are shown as bracketing symbols for the two defect sizes 5 (+) and 10 (-)µm, respectively. The com–bined R fit shows excellent agreement with the fatigue data. The FCGR model shows a poorer fit. Some of the disagreement in the FCGR model is attributed to selecting the model constants m, q, and D to best fit the curvature of the R= +0.05 flat specimen data.

The R=+0.05 flats data is compared to the FCGR model predictions. Here the FCGR predictions are plotted as constant defect size isoclines. Each plot contains one of the three flat specimen surface conditions. The R=+0.05 T&P cylinder data is also included for reference. Specimen thickness is not differentiated in these plots since it was not an independent parameter in the FCGR model. Thus, the FCGR model represents the data in some thickness average sense.

For the AG and Rm1 specimens, the FCGR model predictions appear to cover the range of measured defect sizes reasonably well. The experimentally measured defect sizes of 37 to 141 and 21 to 250µm for the AG and Rm1 chem milled conditions, respectively, largely fall between the 50 to 200µm model prediction isoclines. Similarly, the M&P specimens also show rough agreement. Those specimens had measured defects sizes of 16-108µm and they largely fall between the 15-80µm isoclines.
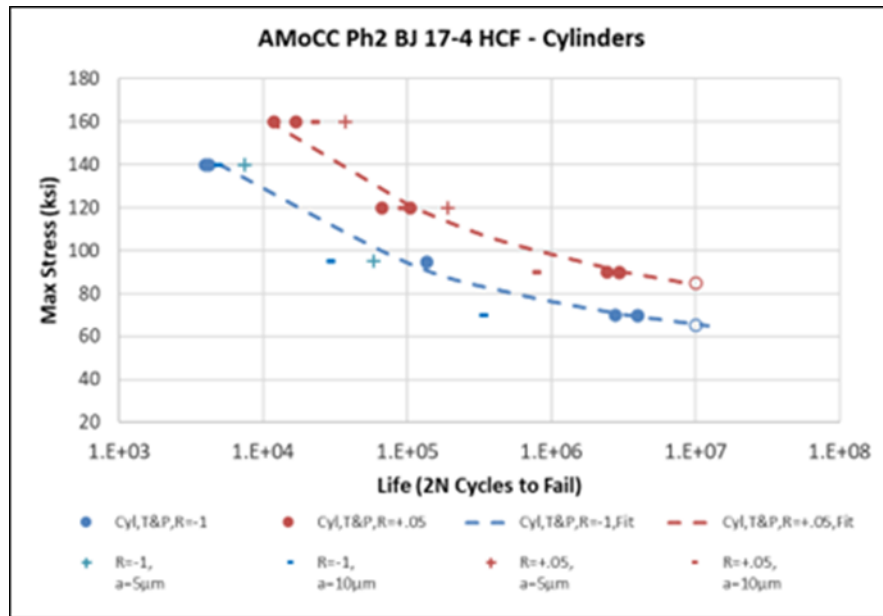
Figure 34.   FCGR Model Fit vs Cylinder Data

Figure 35 presents the data in another way. Here the FCGR relationship is used between "a" and fatigue life to predict defect size "a" based on experimental specimen life, 2Nf. That result is plotted against the measured defect size, $\sqrt{A}$.

Acknowledging the scatter, the AG and Rm1 specimens show rough correlation between FCGR predicted and actual measured defect size. The M&P specimens show a roughly linear correlation but with a distinctly different slope. It appears that the model is underpredicting measured defect size for the M&P specimens.

Comparing the T&P cylinders results, the solid (Combined R fit) and dashed (FCGR model) red lines in Figure 36, shows one of the limitations of the current FCGR model – it is unable to simultaneously accommodate both the cylinder and flat specimen data. As previously stated, the
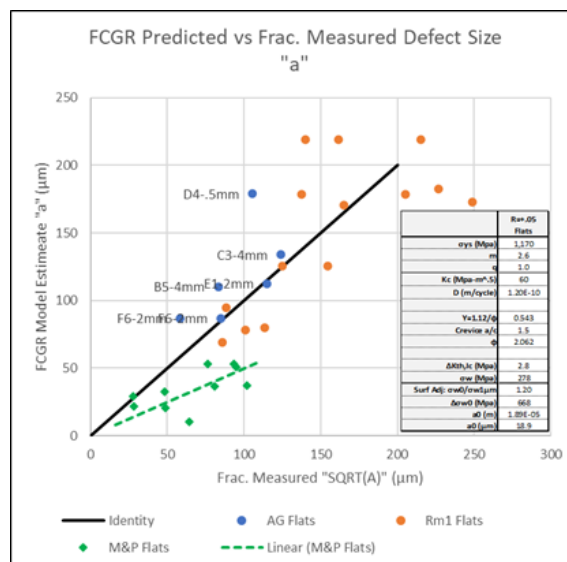
Figure 35.   FCGR Predicted vs Measured Defect Size
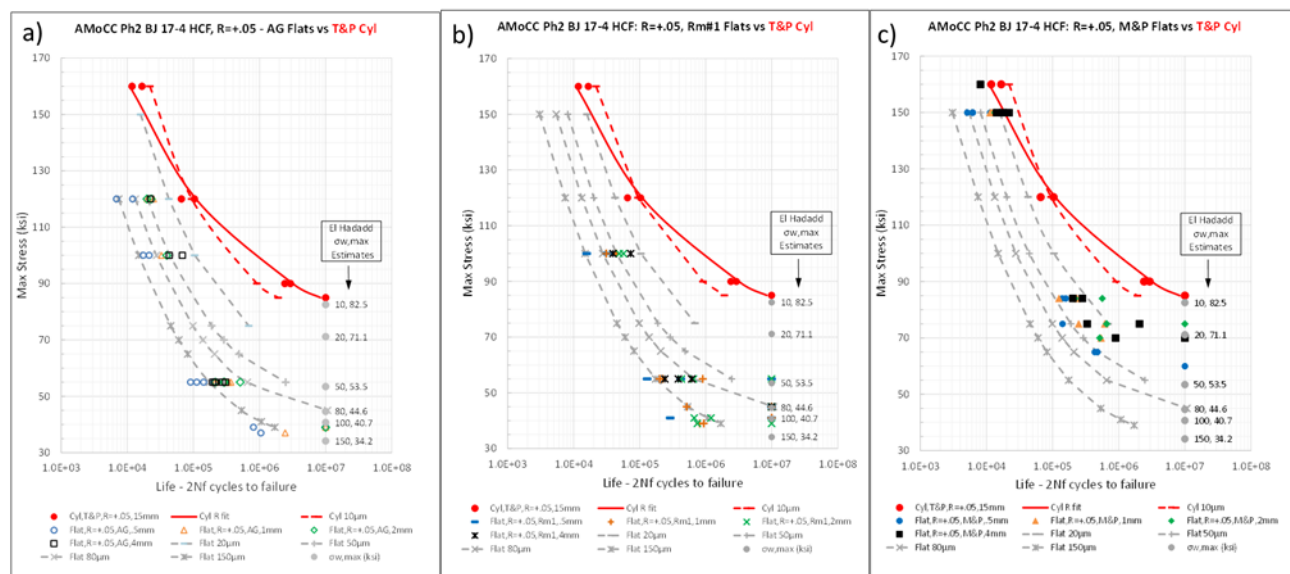
Figure 36. FCGR Defect Model vs a) AG Flats Data, b) Rm1 Flats Data, c) M&P Flats Data

model constants m, q, and D were purposely chosen to best represent the R=+0.05 flat specimen data. This included adjusting the parameters so that the defect isoclines were roughly orthogonal, that is independent of stress level. Minimizing this error for the flat specimen's results in a significant mismatch, not in average but in slope, to the cylinder data.

The converse was also true; adjusting the parameters to minimize the error for the cylinders improves the cylinder fit but results in a mismatch in slope for the flat specimens. The specimens are behaving as if the fatigue mechanism between these two populations is different, though this cannot be conclusively determined with the given set of data.

This is aligned, but by itself does not prove, the prior statements concerning the effect of defect shape and orientation on stress intensity. Geometrically similar defects should present similar stress intensities and fatigue behaviors; different defect types may have different stress intensities and hence produce different fatigue behavior.

3.2.14 Conclusions

The tensile and HCF behavior of binder jet produced 17-PH in the HIPed and H900 condition was measured for both machined cylindrical specimens at two stress ratios, R=-1 and R= +0.05, and flat specimens at one stress ratio, R=+0.05. The flat specimens were grown to four nominal thicknesses (0.5, 1, 2, and 4mm) and finished to three surface conditions, AG, lightly chemical milled (Rm1), and M&P. Ultimately the M&P flats were found to be deficient in surface quality due to inadequate control over the polishing process, nevertheless they represented a third intermediate state in surface quality. A summary of key observations and conclusions is as follows:

1. Tensile results for the turned T&P cylinders were very near published data in MMPDS for 17-4PH H900 plate. Tensile ductility showed a persistent effect due to thickness with the thinnest specimens behaved in a more brittle manner with significantly lower elongation at break (5 vs 15%). This effect was true regardless of surface condition. In contrast, tensile strength across the different thickness flats were both higher and lower than the cylinders. The strength of the thinnest machined flats were in some instances higher then the cylinders

while the strength of the thinnest as-grown flat specimens were consistently lower. This behavior was attributed to the effect part thickness may have had on temperature and resulting material condition, including defect sensitivity, during heat treat.

2. Fatigue performance of the T&P cylinders was found to be lower than MMPDS published data for unnotched 17-4PH bar in the H900 condition, but higher than the same material in a notched state with Kt=3. The T&P cylinder data was also found to be in line with at least one other reference for L-PBF manufactured 17-4 PH. Comparison of the cylinder data at two R ratios with the classical methods of estimating the effect of mean stress attributed to Soderberg showed the Soderberg construct to be non-conservative. That is, measured combined stress fatigue performance fell below that predicted by Soderberg.

3. Fatigue performance of the flat specimens including the M&P specimens was significantly below that of the cylindrical specimens, largely attributed to their poorer surface condition. The AG specimens showed to highest debit with the lightly chem milled (~0.0015" removed per side) specimens almost identical in performance. The M&P flats, because of inadequate surface preparation, showed high variance and ran between the results of the AG flats and T&P cylinders.

4. CT x-ray and metallurgical sectioning were used to measure surface crevice depth left by the sintering process. The methods and showed reasonably good agreement in measured values. Both methods provided mean depth of valley (Dv(50,50)) depths of 35-50µm and 95% confidence, 99% percentile (Dv(95,99) depths of 75-86 and 66-73µm, respectively, using an extreme value distribution. Separately, review of the CT volume file showed how interconnected the surface crevices were and that most if not all of the subsurface voids observed in 2D sections, were actually surface connected porosity.

5. Fractography for a subset of the fatigue specimens showed the failure origin to be at surface oxide inclusions for the two cylinders that were inspected, and surface crevices in all the flat specimens that were inspected. The M&P flats showed the origin to be remnant crevices not fully removed by polishing.

6. A short crack fatigue crack growth model was assembled and compared with both the cylinder and flat specimen fatigue data. In addition, the model was used to make predictions about expected defect size based on actual specimen fatigue performance. These predictions were then compared with defect size measurements taken during fractography. With appropriate constants, the model showed reasonable semi-quantitative correlation to both the AG and Rm1 flats data. Greater deviation was observed between the model and the M&P flats and T&P cylinders. It was concluded that defect "type" matters and that modifications to the model would be needed to accommodate a larger range of surface conditions.

3.3 Optimized AM AlSi10Mg and Steel Performance

3.3.1 High-Strength Al Alloys in Laser Powder Bed Fusion

This section details the test results of high-strength aluminum alloys conducted under the Eaton Aerospace Euclid work stream of the AMoCC project. Specifically, these results satisfy the requirements evaluation of High-Strength Aluminum Alloys for L-PBF. The three alloys down-selected for evaluation were Elementum 3D 7050-RAM2, Eckart A205, and APWORKS Scalmalloy.

High-strength aluminum alloys have proven to be an elusive target for L-PBF due to issues such as cracking during the process. Aluminum alloys in the 6000 and 7000 series are ubiquitous in the Aerospace industry and enabling their manufacture via AM will open new opportunities to improve part quality, cost, and lead time.

The work planned was intended to generate an initial set of data to determine the mechanical strength of three high-strength aluminum alloys specially developed for AM. The data collected came from tensile, high-cycle fatigue, and metallurgical specimens.

Test specimens were built in partnership with three material suppliers: Elementum 3D, Eckert, and APWORKS on their recommended platform and with their recommended parameters and heat treat. All mechanical testing was performed using accredited third-party external laboratories. Metallur–gical and post-test inspection of mechanical test specimens was performed in Eaton Aerospace labs in Euclid, OH.

Aluminum 7075-T73 was selected as a benchmark for this study following extensive internal reviews with Eaton Chief Engineering teams. An AM equivalent to this conventional wrought alloy would provide significant benefit to Eaton products by enabling more compact designs, improved product performance, and reduced weight.

Following the selection of 7075-T73 as the benchmark, a comprehensive review of available high-strength aluminum alloy powders was conducted. Key metrics were collected from each manu–facturer to determine the two alloys to include in this study. A sample of the comparison data is shown in Table 10.

Based on this data Eaton decided to proceed with A205 manufactured by Eckert GmbH, 7050-RAM2 manufactured by Elementum 3D, and Scalmalloy manufactured by APWORKS GmbH.

Table 10. Sample of Initial Material Down-Selection Evaluation

	Al 7075-T73 (plate)	A205	A7075-RAM2	A7050-RAM2	A2024-RAM2	Scal-malloy	Al 7A77.60L	Ti-6Al-4V (EBM)
UTS (ksi)	73	65.2	80	72.5	70	75.4	75	126
YTS (ksi)	60	56.6	75	67.5	51	69.6	71	106
Elong. (%)	7	10	3	4.5	8	13	6	9
$ / lb	$5	$90	$113	$78.20	$113	$159	Unknown	$45.50
Hardness (HRB)	87	95	90	88	78	82	-	108

Requirements were defined in a Statement of Work that asked suppliers to build a total of 74 specimens in multiple orientations using their material and build parameters that were validated for their material and on their preferred platform. Eaton did not dictate the thermal treatment and instead asked the suppliers to use a validated heat treatment that would achieve properties approaching the benchmark, wrought aluminum 7075-T73.

The Scalmalloy dataset was not as extensive because it was decided to add this material to the plan late in the project and specimen that had already been built were utilized for testing.

The A205 powder was an Al-Cu-Mg-Ag alloy with added ceramic TiB_2 particles. The powder itself consisted of individual spherical particles ranging in size from 20-63 microns. SEM images of the powder are shown in Figure 37 and Figure 38. These images show that the powder is generally spherical with a small percentage of non-spherical particles. It can also be seen that a small percen–tage of the particles contains agglomerates or satellites. These agglomerates and satellites are not uncommon in powdered metals, but if numerous and severe enough they can cause issues in L-PBF process.
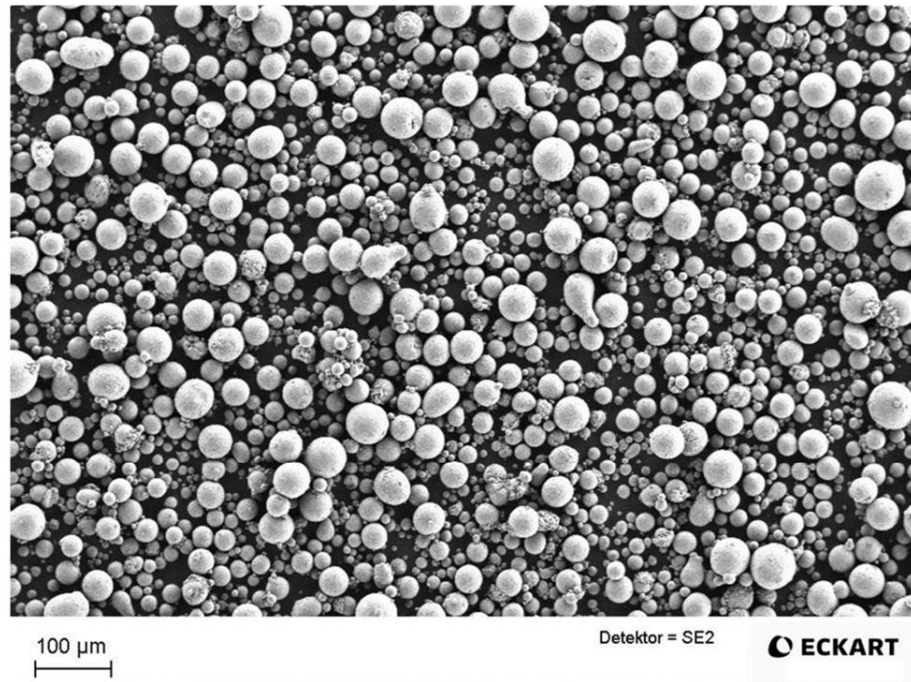
Figure 37. Macro SEM Image of A205 Powder
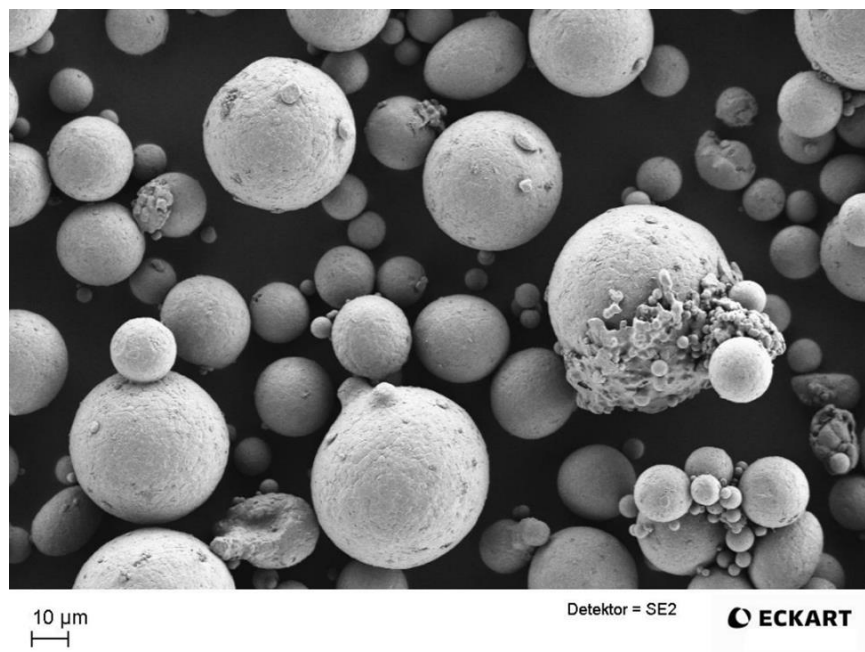
Figure 38. SEM Image of A205 Powder

This information, as disclosed to DOD, shall not be modified without the written consent of NCMS.
DISTRIBUTION STATEMENT A. Approved for public release. Distribution is unlimited. OPSEC#9316

51

Eckert conducted two builds of the layout shown in Figure 39 and Figure 40 at a partner supplier, Material Solutions, on an EOS M290 platform using powder provided by Eckert and parameters supplied by Eckert and specifically designed for the A205 material.
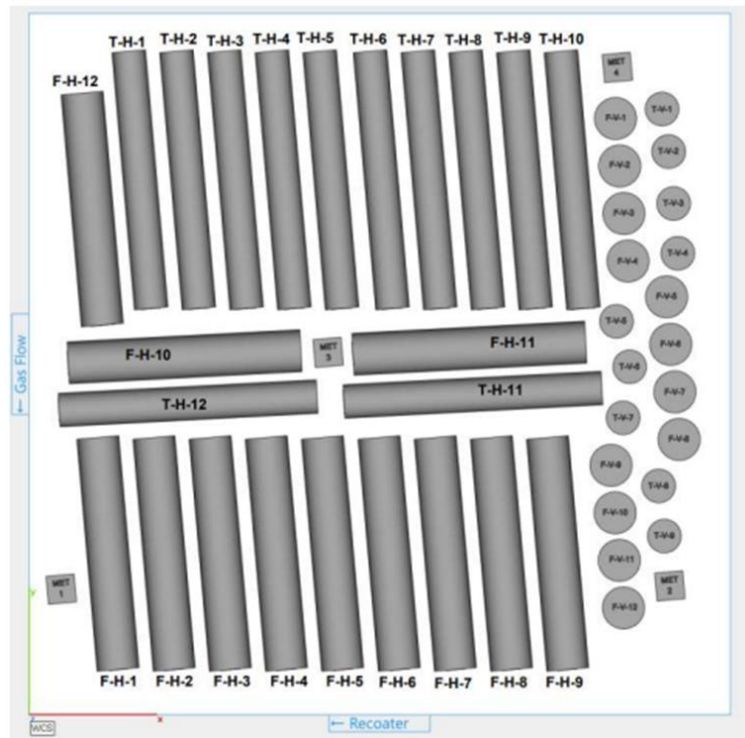
Figure 39.   Build Layout for A205 Material
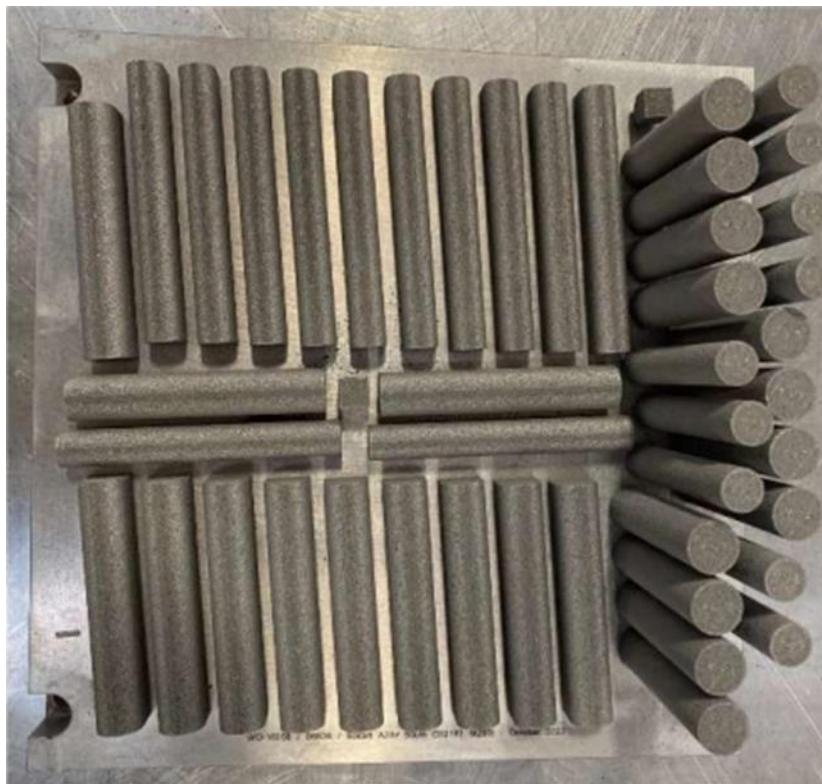
Figure 40.   Build Plate After Heat Treatment

A few of the basic parameter settings are listed below:

- 350W laser power
- 1,600mm/s scanning speed
- 100μm hatch distance
- 30μm layer thickness
- 200°C pre-heat
- 1.8m/s gas flow

Following the build the specimens were heat treated on the build plate per the instructions below:

Solution treatment
1. Place parts in a cold oven.
2. Ramp to 505°C (941°F) in not less than 100 minutes.
3. Hold at 505°C (941°F) for 2 hours (minimum); up to 4 hours for larger, more complex sections.
4. Ramp to 530°C (986°F), no delay.
5. Hold at 530°C (986°F) for 4 hours (minimum); up to 6 hours for larger, more complex sections.
6. Quench in 20-25% glycol (polymer) solution, max. quench delay 10 seconds; cold water quench may be used where maximum strength is required and there is little risk of distortion.

Artificial aging
1. Place parts in an oven.
2. Heat to 190°C (374°F).
3. Hold for 4-6 hours.
4. Cool to room temperature; it is acceptable to turn off the oven, open the doors and for the parts to be left to cool.

The mechanical strength of the A205 material was performed per ASTM E8 and is summarized in Table 11. The data is individually summarized for both horizontal and vertical orientated specimen due to the significant anisotropy exhibited by the material. Fourteen specimens were tested in each orientation.

The HCF performance of the A205 material was measured per ASTM E466 and is summarized in Figure 41. Unfortunately, the A205 material did not produce a normal fatigue curve when tested for either of the two growth orientations. Upon investigation of the suppliers, it was found that the

Table 11. A205 Mechanical Strength Summary

A205 Summary	# of Specimen	Ultimate Tensile Strength (ksi)	0.2% Offset Yield Strength (ksi)	Elongation (%)	Reduction of Area (%)	Young's Modulus (GPA)
Orientation	#	Average	Average	Average	Average	Average
Z	14	69.8	60.1	11.5	18.3	76.8
XY	14	62.5	51.2	8.7	13.7	77.8
Orientation	#	St. Dev.	St. Dev.	St. Dev.	St. Dev.	St. Dev.
Z	14	0.3	0.4	1.4	3.4	2.3
XY	14	1.8	2.7	1.0	2.4	2.5
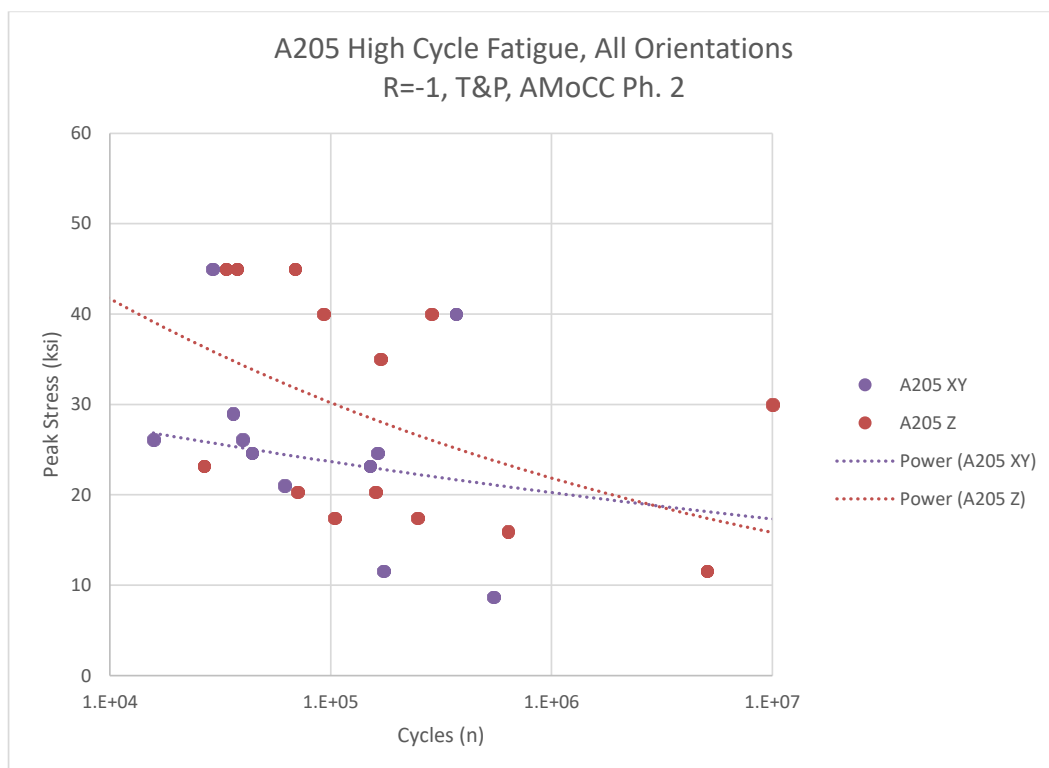
Figure 41.   HCF Performance of A205 Material in All Orientations

specimen were not properly polished prior to HCF testing. It is believed that the failure to longitudinally polish the specimen led to the significant scatter observed in the results. Another compounding factor is that the HCF testing was performed at a stress ratio of -1 and 50 Hz which is higher than Eaton's standard of 30 Hz. Eaton has observed in previous HCF testing of aluminum that specimen heating can become an issue at test frequencies over 30 Hz, however no specimen heating issues were reported by the test lab.

Elementum 3D conducted two 7050-RAM2 builds of the layout shown in Figure 42 on an EOS M290 platform owned and operated by Elementum 3D. The powder was supplied by Elementum 3D as were the parameters used for the build. The details of the parameters are considered proprietary and were not provided by Elementum 3D. They would be provided as part of the terms of a future powder purchase.

The 7050-RAM2 powder is a proprietary alloy from Elementum 3D that includes 2% ceramic particles to enable an alloy that mimics A7050 properties. The powder itself consists of individual spherical particles with a particle size distribution as measured by laser diffraction method as follows: D10 – 18.38µm, D50 – 30.96µm, D90 – 49.0µm. The ceramic is believed to be a titanium oxide based on SEM/EDS analysis.

Following the build the specimens were removed from the build plate and heat treated per the instructions below.

Hot Isostatic Pressing
- 454°C ±13°C (850 ±25°F) for 120 minutes minimum at 14.5ksi minimum (to be performed prior to heat treatment)

T74 Heat Treatment

Solution treatment
1. Heat in furnace to 475°C ± 5°C (887°F ± 9°F) with approximately 15°C (27°F) per min ramp rate.
2. Hold at 475°C ± 5°C (887°F ± 9°F) for 3.0 hours.
3. Immediately quench in cold water.

Notes: Controlled atmosphere is not required. Furnace ramp rate is not critical but should minimize overshoot. Quench timing is important, and the part should rapidly go from 475°C (887°F) to fully submerged in cold water. Complex and thin-walled parts may require a slower quench media to minimize distortion. Traditional 7050 heat treatment recommendations for thin-walled parts can be followed (hot water or a polymer quench).

Artificial aging
1. Heat furnace to 107°C ± 5°C (225°F ± 9°F). Place parts in furnace once reaching temperature 100°C ± 5°C.
2. Heat furnace to 107°C ± 5°C (225°F ± 9°F).
3. Ramp up at 15°C per minute (without removing parts) to 177°C ± 5°C (350°F ± 9°F).
4. Hold at 177°C ± 5°C (350°F ± 9°F) for 8 hours.
5. Air cool.

The thermal treatment regimen described above was found to be effective at dissolving gas porosity and L-PBF defects into the material.
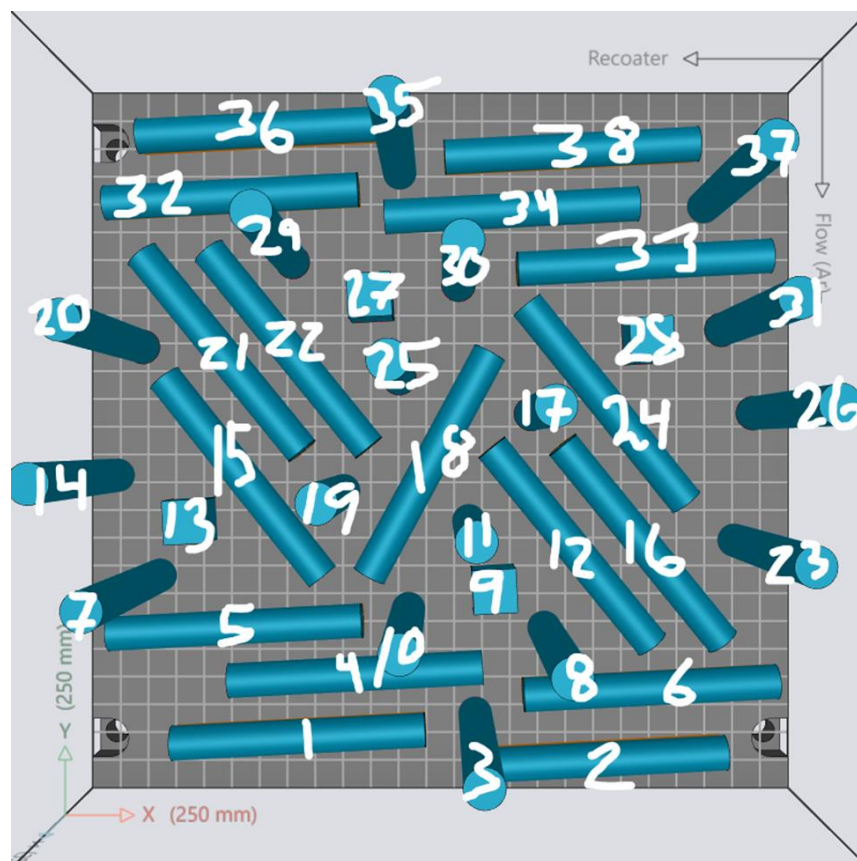
Figure 42.   Build Layout for 7050-RAM2 Material

The mechanical strength of the 7075-RAM2 material was performed per ASTM E8 and is summarized in Table 12. The data is individually summarized for both horizontal and vertical orientated specimen, but you will notice that unlike the A205 material the 7050-RAM2 material exhibits only minimal anisotropic performance.

Table 12. 7050-RAM2 Mechanical Strength Summary

A7050-RAM2 Summary	Ultimate Tensile Strength (ksi)	0.2% Offset Yield Strength (ksi)	Elongation (%)
Orientation	Average	Average	Average
Z	74.8	68.7	6.5
XY	73.8	67.4	6.4
Orientation	St. Dev.	St. Dev.	St. Dev.
Z	0.7	0.7	0.6
XY	0.5	0.5	0.7

The HCF performance of the 7050-RAM2 material was measured on turned and polished specimens per ASTM E466 and is summarized in Figure 43. The HCF curves produced by the 7050-RAM2 data exhibit minimal scatter and the results also exhibit minimal anisotropy, similar to the mechanical strength results. It should be noted that the 7050-RAM2 curves were generated with fewer data points than the A205 curves – 16 vs 40 respectively.
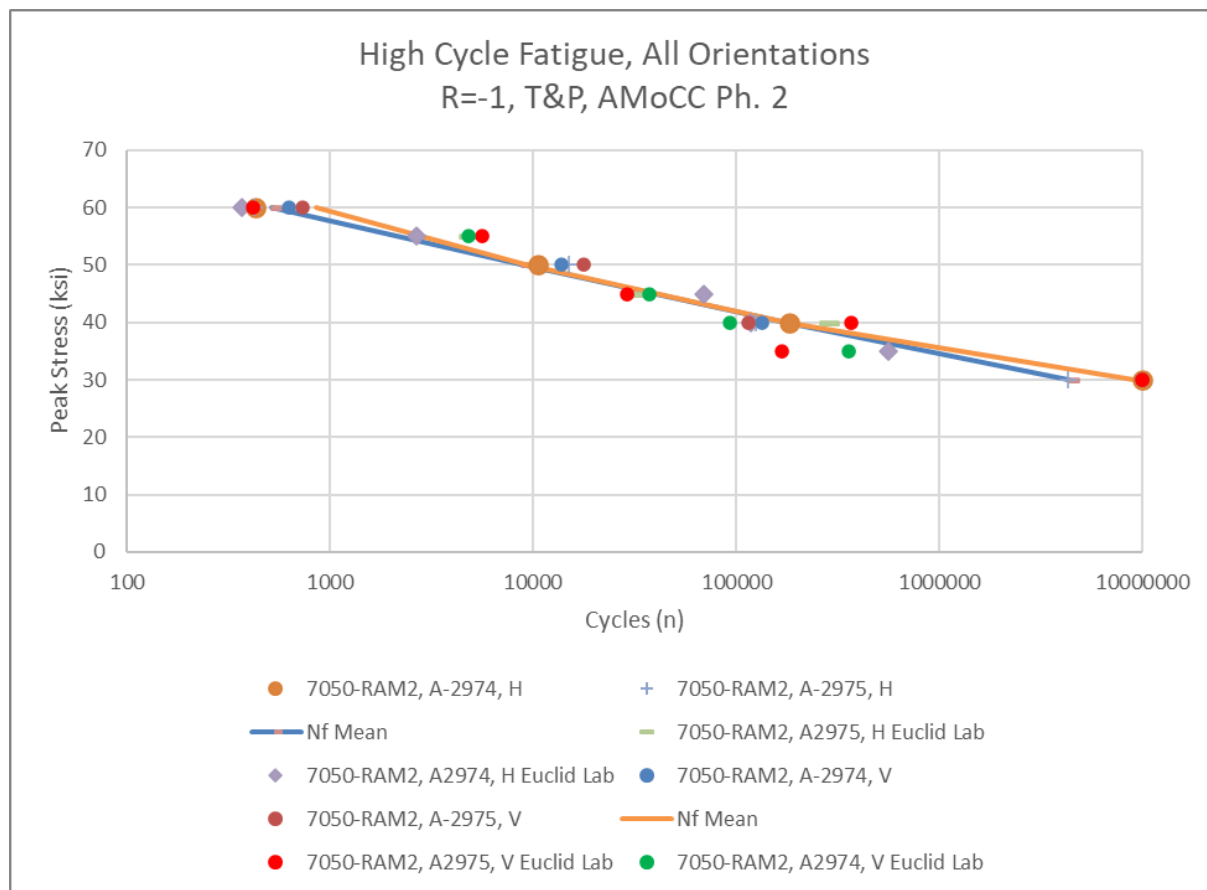
Figure 43.   HCF Performance of 7050-RAM2 Material in All Orientations

The Scalmalloy material was produced by Progressive Technology Group on their EOS M290 platform using parameters that were developed specifically for the Scalmalloy material. These parameters are considered proprietary and were not provided to Eaton. The powder was supplied by Carpenter.

The Scalmalloy powder is a proprietary alloy from APWORKS that includes up to 0.88% scandium to provide exceptional strength and corrosion resistance. The powder itself is produced in a nitrogen gas atomization process and sieved to achieve a 20-63µm nominal particle size.

Following the build, the specimens were removed from the build plate and subjected to a stress-relief heat treatment consisting of a 325°C hold for 4 hours. This simple heat treatment with no require–ment for HIP provides a significant operational advantage for Scalmalloy over both A205 and 7050-RAM2.

The thermal treatment regimen described above did not completely dissolve the porosity inherent in the material and left up to 0.15% porosity. This porosity can be improved by implementing a HIP step prior to the heat treat process if the porosity is found to be detrimental to material performance for any specific application. The porosity evaluation can be found in Figure 44.
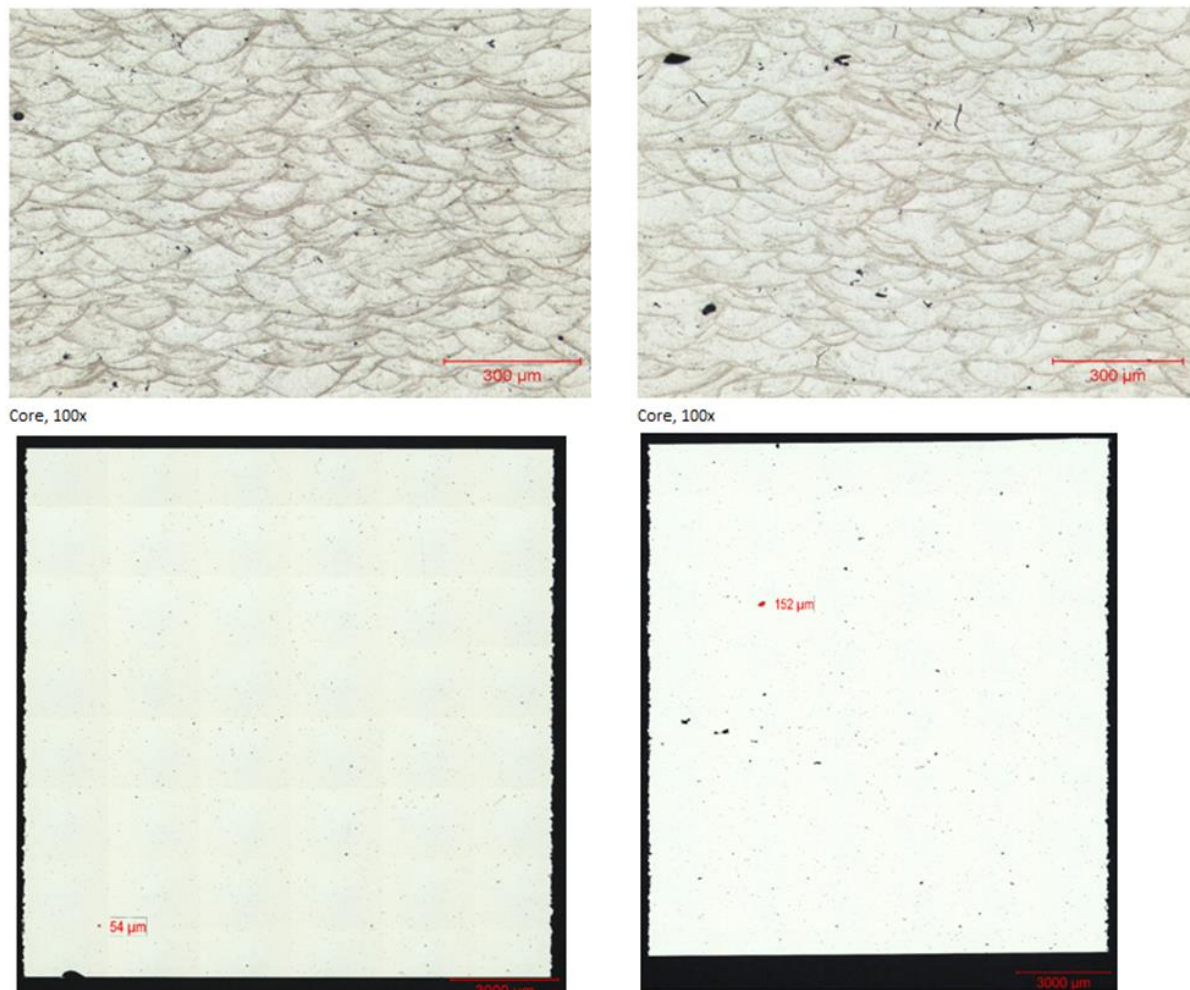
Figure 44. Optical Microscopy of Scalmalloy Material
The samples on the left have 0.1% porosity while the samples on the right have 0.15% porosity

The mechanical strength of the Scalmalloy material was performed per ASTM E8 and is summarized in Table 13. The data is individually summarized for both horizontal and vertical orientated specimen. Only four samples were tested in each orientation. Similar to 7050-RAM2, the Scalmalloy material in the stress-relieved condition did not exhibit significant anisotropy.

The HCF performance of the Scalmalloy material was measured on turned and polished specimens per ASTM E466 and is summarized in Table 14 and Figure 45. With only four specimen per orientation it is impossible to create a true fatigue curve for Scalmalloy, but what can be seen is that Scalmalloy appears to perform more similar to A205 than it does 7050-RAM2 as Scalmalloy does appear to exhibit anisotropic HCF behavior.

The 7050-RAM2 and Scalmalloy materials have higher mechanical strength and generally lower anisotropy than the A205 material at room temperature. Although high temperature mechanical strength was not tested in this study the literature does make it clear that the A205 material appears to be better suited for higher temperature applications between 125°C and 250°C than the 7050-RAM2 and Scalmalloy materials. The high temperature data provided by the technical data sheets can be found in Table 15. No high temperature tensile data was available for 7050-RAM2; however, one would expect that the presence of inert dispersants should help to retain its high-strength to elevated temperatures.

Table 13. Scalmalloy Mechanical Strength Summary

Scalmalloy Summary	Ultimate Tensile Strength (ksi)	0.2% Offset Yield Strength (ksi)	Elongation (%)
Orientation	Average	Average	Average
Z	75.4	70.3	9.5
XY	76.8	70.5	8.1
Orientation	St. Dev.	St. Dev.	St. Dev.
Z	1.4	0.3	2.8
XY	1.0	1.1	0.9

Table 14. Scalmalloy HCF Results

S/N	Orientation	Machine	Max Stress (ksi)	Cycles to Failure	Failure Location
Scalmalloy - SR, Vertical					
B7775-01-V	vertical	H129	14	161630	Gage Section
B7775-02-V	vertical	H139	10	10000000	Discontinued
B7775-04-V	vertical	H129	10	10000000	Discontinued
B7775-03-V	vertical	E15	6	2485410	Gage Section
Scalmalloy - SR, Horizontal					
S/N	Orientation	Machine	Max Stress (ksi)	Cycles to Failure	Failure Location
B7775-01-H	horizontal	H223	14	10000000	Discontinued
B7775-02-H	horizontal	H222	10	10000001	Discontinued
B7775-03-H	horizontal	H220	6	10000002	Discontinued
B7775-04-H	horizontal	H222	18	115474	Gage Section
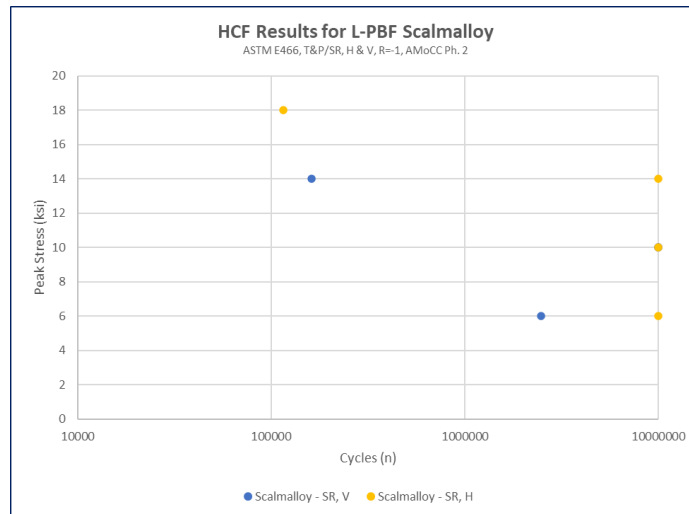
Figure 45. HCF Performance of Scalmalloy Material in Vertical and Horizontal Orientations

Table 15. High Temperature Mechanical Strength Comparison

	Ultimate Tensile Strength (ksi)		0.2% Offset Yield Strength (ksi)	
Temp. (°C)	A205	Scalmalloy	A205	Scalmalloy
100	61.4	58.0	54.4	55.0
150	53.5	45.7	51.3	40.0
200	48.0	23.6	45.1	20.0
250	32.5	11.3	31.2	10.3

The anisotropy of A205 is also evident in the HCF results shown in Figure 46. Similarly, the isotropic behavior of 7050-RAM2 is also apparent in the HCF results. Due to the significant anisotropy of A205 the overall performance of the material is pulled down which renders the 7050-RAM2 material as the best performing material in HCF. The Scalmalloy material, keeping in mind that only four specimens were tested in each orientation, does not exhibit significant anisotropy, but does appear to have the lowest HCF endurance limit of the three materials tested.
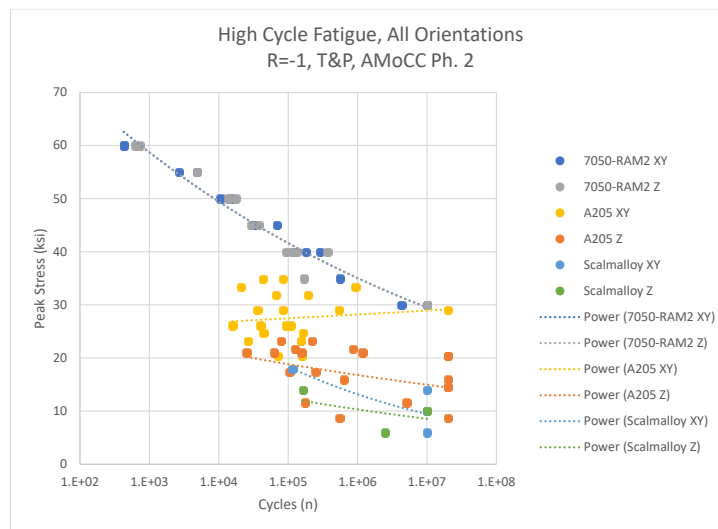
Figure 46. HCF Test Results for All Materials and All Orientations

Based on the results presented herein the Elementum 3D 7050-RAM2 material stands out as the best high-strength aluminum for L-PBF of the three materials evaluated. While the mechanical strength of 7050-RAM2 is slightly lower than that of Scalmalloy the high-cycle fatigue performance is significantly better than both A205 and Scalmalloy. Additionally, 7050-RAM2 is the lowest cost per pound at $78.20 making it the most likely of the three to yield a good business case.

It is recommended that further work be performed with 7050-RAM2 to better understand processing risks or limitations and to better characterize the performance of the material especially in the as-grown surface condition which was not part of this initial study. Additional information pertaining to optimization of steel performance is provided in Section 3.7.

3.3.2 High Productivity L-PBF

This section summarizes the efforts to study the options for improving the productivity of the L-PBF process for metals. It is understood that productivity improvements can only be realized at an equivalent quality level, characterized by the defect distribution and the microstructure attained by the process. In this study, only the impact of the defect distribution on the quality of the product will be addressed. The impact of post-processing, after the L-PBF process, to ameliorate the defect structure or attain a more desirable microstructure are not considered. The different metrics used to describe the defect structure can be related to the properties relevant to the application under con–sideration. Thus, the goal of this study was to obtain the relation between productivity and defect structure for various process parameters. While the material of choice has been the aluminum alloy AlSi10Mg, it was hoped that the conclusions drawn from this study will inform the improvement of productivity associated with other metallic powders, including steels.

The options investigated for improving productivity may be categorized as those related to:

- Redistributing the laser power by beam shaping
- Changing powder characteristics

Beam shaping is made possible by the nLight AFX-1000 ring mode laser that offers the ability to switch between seven modes of operation with different energy distribution ranging from a standard Gaussian distribution to a ring mode distribution with multiple peaks. The different indexes with the energy distribution between the center and the ring are shown in Figure 47. The various indexes allow one to control the temperature profile within the meltpool as indicated in Figure 48. This ability to prevent an overheating of the meltpool enables a greater energy input into the powder bed
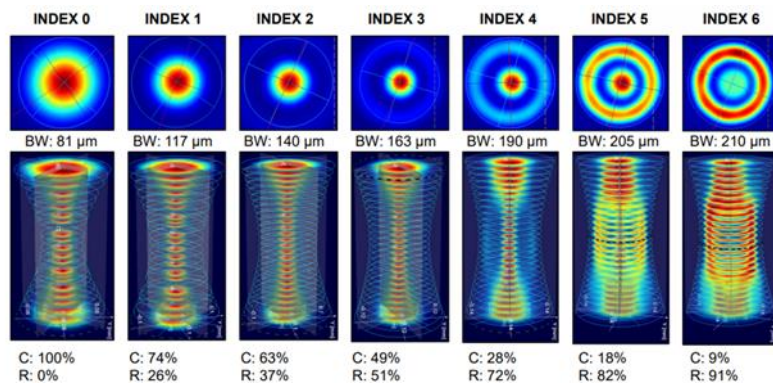
Figure 47.   Energy Distribution between Core and Ring for Different Modes of Operation of AFX Ring Mode Laser
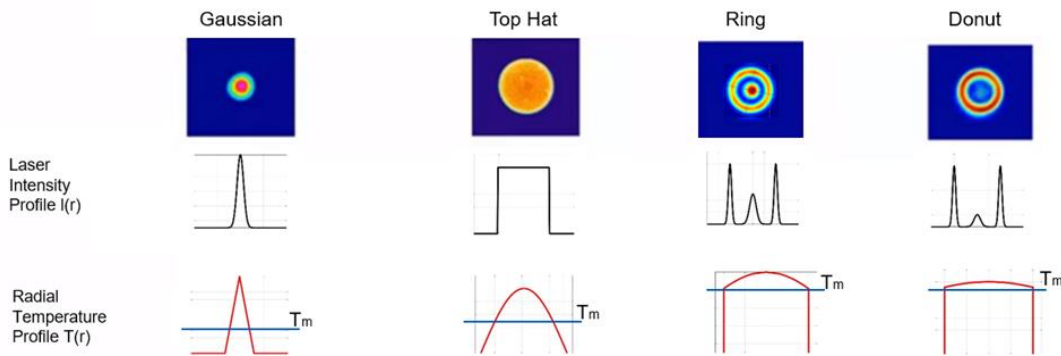
Figure 48.   Temperature Profiles Achievable with Different Energy Distributions in Beam

resulting in larger meltpools and consequently greater productivity. The ability to switch between modes in milliseconds affords the opportunity to achieve both productivity and feature resolution without compromise.

The potential for productivity increases would be determined from single line scan experiments to determine the melt volume swept as defined in Figure 49. This would be higher than the actual build rate used but would be proportional to the build rate achievable in practice and can hence be used as a relative measure of productivity.

The quality achieved was evaluated in terms of the defect distribution determined by x-ray CT scanning. Due to the excessive cost of performing x-ray CT scanning on a large number of specimens, down-selection of the specimens to the ones that provide the most information was done by determining the density by the Archimedes procedure. An example of the defect characterization obtained from an x-ray CT scan is depicted in Figure 50. The defects are characterized by the percentage porosity, a probabilistic estimate of the largest pore size and the amount of connected porosity. There are correlations between these characteristics, nevertheless they were determined, with a view to using them to relate the experimental conditions to the mechanical properties determined by tensile testing and fatigue testing in follow on studies.

The experiments to evaluate productivity improvements with the Nlight AFX, beam shaping laser were done in stages. An exploratory study was done on the AM Customized Machines (AMCM) platform. Following the exploratory study, the verification of the repeatability and transferability of the results was performed on an Open Additive PANDA Machine. Following this repeatability and transferability study, a verification of mechanical properties achievable and the impact of powder size distribution were performed on an Open Additive PANDA Machine.
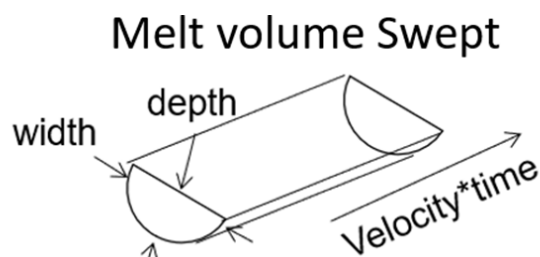
Figure 49.   Melt Volume Swept
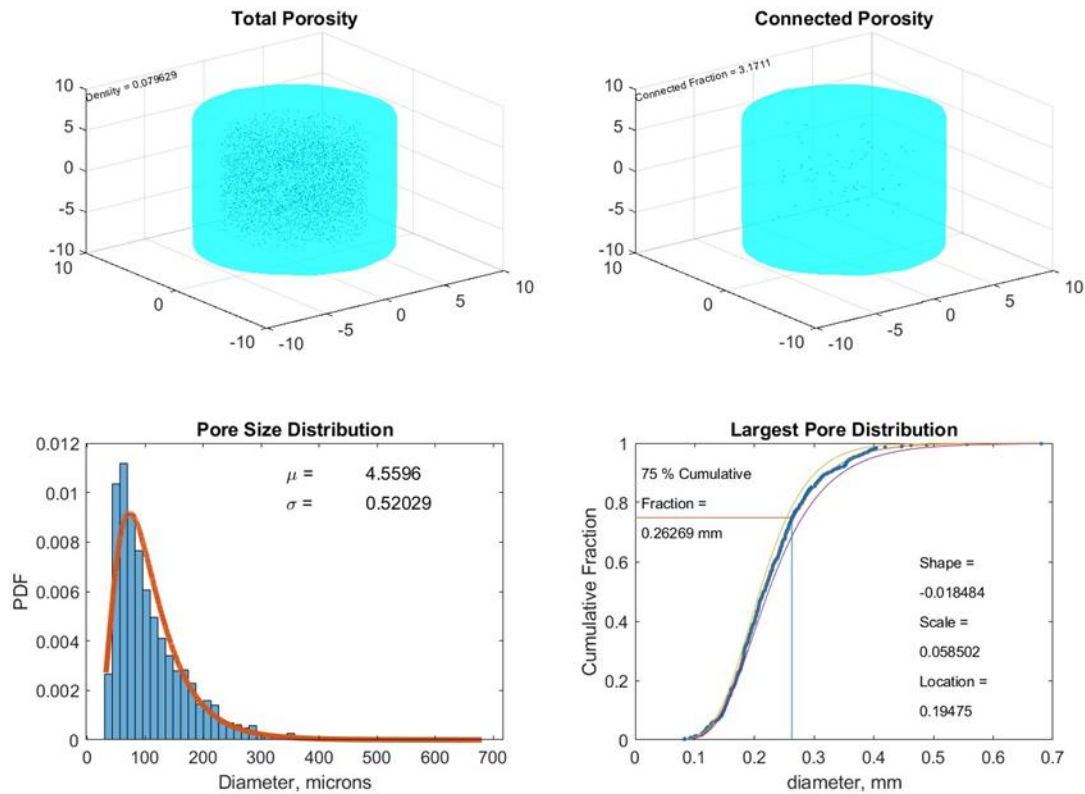
Figure 50. Example of Porosity, Largest Pore Size and Connected Porosity Determination from X-ray CT

For the exploratory study, a Design of Experiments (DOE) with parameters shown in Table 16 were employed. Two builds were completed, one with a 60-micron layer thickness and the other with an 80-micron layer thickness. In each of these builds, cylindrical specimens with 0.75" diameter and 0.75" height were built at each of the conditions shown in the DOE table for defect characterization by x-ray CT analysis. In addition to the cylinders, single line scan exposures were performed at the power, velocity and mode combinations listed in the DOE table.

Table 16. Experimental Conditions for Cylinder Builds and Single Line Scans

Power (Watts)	Hatch (µm)	Mode 0 (Gaussian) 800 mm/s	1200	1600	2000	Mode 4 (Top Hat) 800	1200	1600	2000	Mode 5 (Ring) 800	1000	1200	1600	2000	2200	2400	Mode 6 (Donut) 800	1000	1200	1600	2000	2200	2400
400	170	1	2	3	4																		
500	200	5	6	7	8																		
600	220	9	10	11	12	17	18	19	20	29		30	31	32			41		42	43	44		
750	240	13	14	15	16																		
800	260					21	22	23	24	33		34	35	36			45		46	47	48		
	280									55							65						
	180															59	58						69	68
	200																57							67
	240												60	56							70	66	
1000	280					25	26	27	28	37	53	38	39	40			49	63	50	51	52		
	300									54							64						
	320									61							71						
	360									62							72						

Figure 51.   Archimedes Density Variation for 60-Micron Layer Height Cylinders
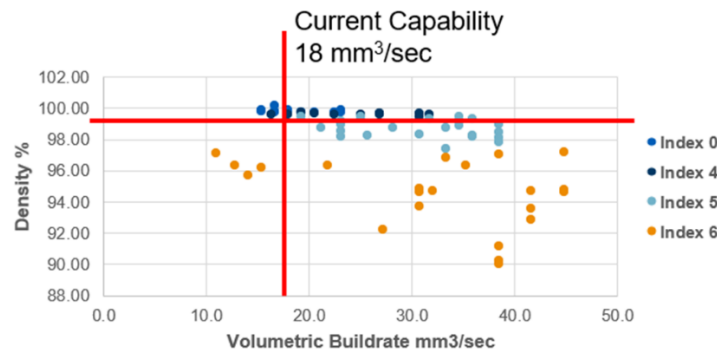
Figure 52.   Archimedes Density Variation for 80-Micron Layer Height Cylinders

The corresponding cylinder identification numbers for the cylinders selected for x-ray CT analysis are shown in Table 17 and Table 18 for the 60-micron layer thickness build and the 80-micron layer thickness build respectively. The conditions for the samples selected for x-ray CT analysis are overlaid as red dots on contour plots of the Archimedes density determination in Figure 53. It may be observed that contours of equivalent density move to decreasing hatch spacing as the scan velocity increases and the contours for the 60-micron layer thickness case are shifted to larger scan velocities and larger hatch spacings indicative of the density being related monotonically to the energy density. This implies that the defects are mainly due to lack of fusion defects.

Table 17.   Specimen Numbers Selected for X-ray CT Analysis for 60-Micron Layer Height Cylinders

sample	Index	Vth [mm³/s]	archimedes density [g/cm³]	arch. density [%] 60 µm layer
022	4.000	18.720	2.668	99.925
026	4.000	20.160	2.666	99.850
034	5.000	18.720	2.667	99.888
038	5.000	20.160	2.665	99.813
046	6.000	18.720	2.666	99.850
050	6.000	20.160	2.664	99.775
059	5.000	23.760	2.665	99.813
060	5.000	23.040	2.664	99.775
068	6.000	25.920	2.664	99.775
069	6.000	23.760	2.667	99.888
070	6.000	23.040	2.667	99.888

Table 18. Specimen Numbers Selected for X-ray CT Analysis for 80-Micron Layer Height Cylinders

sample	Index	Vth [mm³/s]	Archimedes density (scale calculation) [g/cm³]	Arch. density [%] 80 µm layer
022	4	24.96	2.658	99.55
026	4	26.88	2.662	99.70
034	5	24.96	2.660	99.63
038	5	26.88	2.659	99.59
046	6	24.96	2.656	99.48
050	6	26.88	2.662	99.70
053	5	22.4	2.663	99.74
054	5	19.2	2.664	99.78
060	5	30.72	2.656	99.48
061	5	20.48	2.662	99.70
062	5	23.04	2.664	99.78
063	6	22.4	2.660	99.63
064	6	19.2	2.663	99.74
069	6	31.68	2.659	99.59
070	6	30.72	2.661	99.66
071	6	20.48	2.664	99.78
072	6	23.04	2.668	99.93
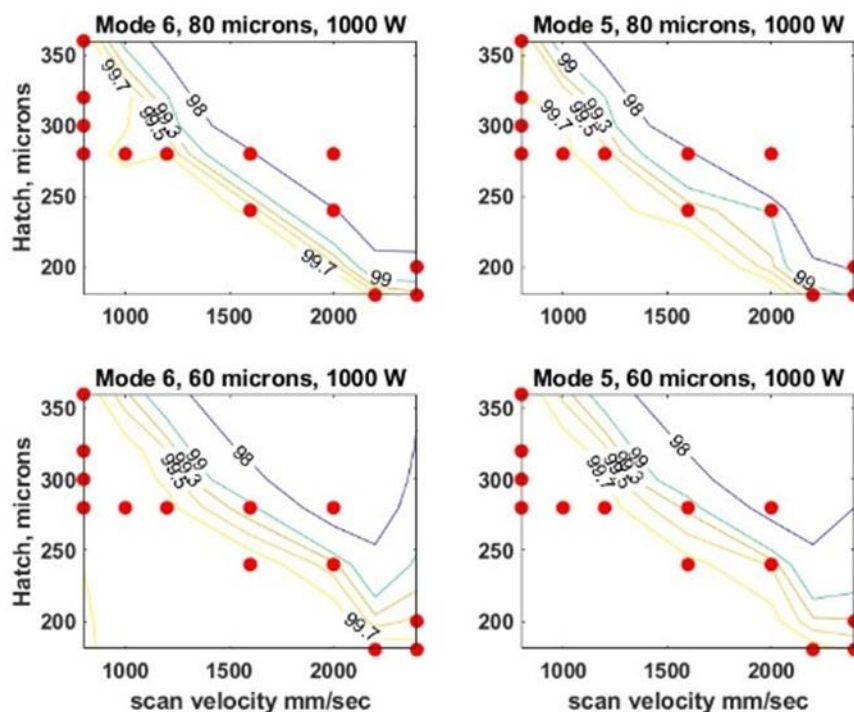
Figure 53.   Contour Variation of Archimedes Density Variation

For the specimens that were CT scanned, the relations between the three quality metrics of density, largest pore size estimate and amount of connected porosity are depicted in Figure 54 and Figure 55. The largest pore size estimate is determined by fitting an extreme value distribution to the largest pores determined in inspection volumes that the sample is divided into. Porosity is considered connected if the separation between centers of circumscribing spheres around neighboring defects is smaller than the sum of the radii of the individual defects. From Figure 54 and Figure 55, it may be observed that the relations between the quality metrics are monotonic hence any of them could serve

as a measure of quality. Therefore for this exploratory study, the amount of connected porosity was taken as the measure of quality and the relationship between productivity and quality as determined from the x-ray CT analysis of the cylinders is depicted in Figure 56. The conditions identifying the productivity quality boundary are identified in terms of (layer thickness/specimens #/Nlight beam shaping mode) in Figure 56. From the conditions identified on the boundary, the three conditions with the best quality were identified to determine repeatability of results and for further investigation by determining mechanical properties. The parameters for the three conditions are identified in Table 19.
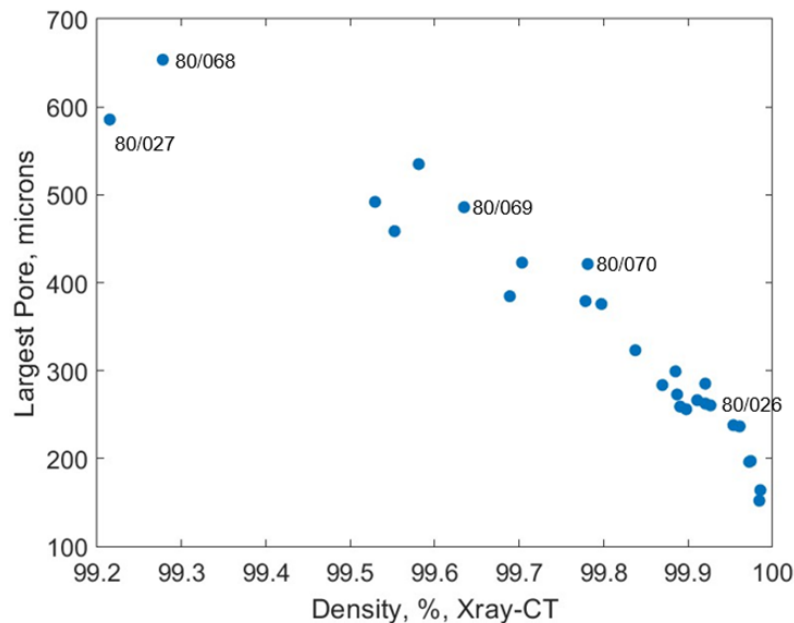
Figure 54.   Relation Between Density and Estimate of Largest Pore Size
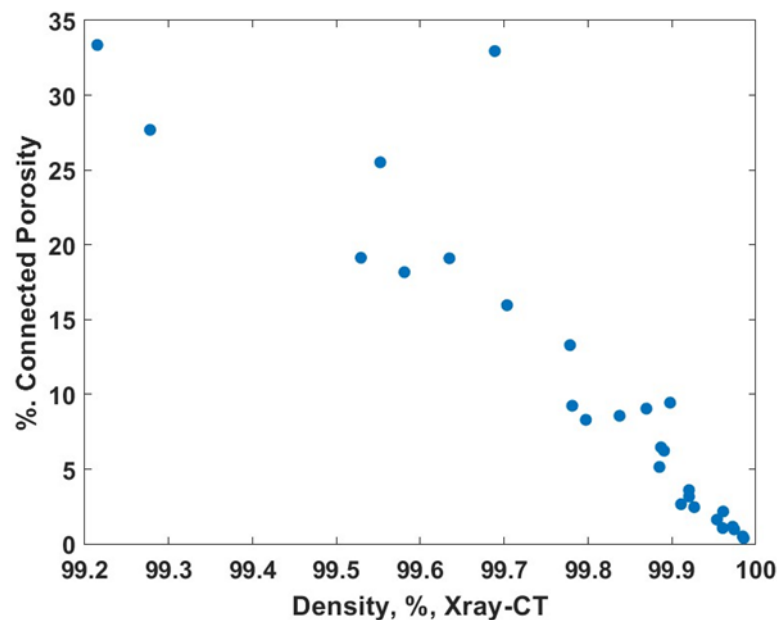
Figure 55.   Relation Between Density and Connected Porosity
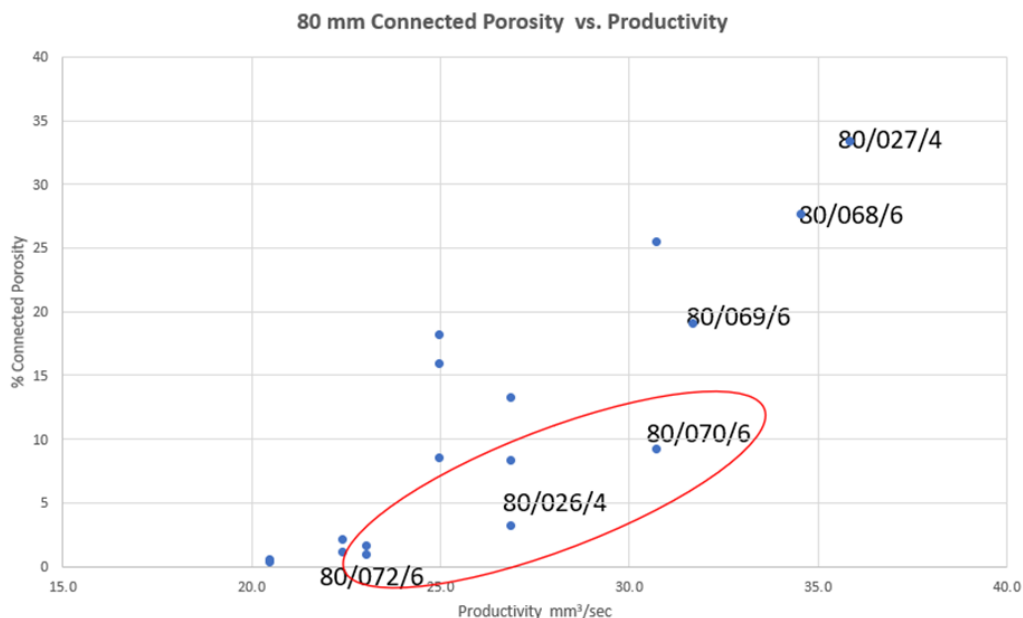
Figure 56. Productivity Quality Variation

Table 19. Parameters for Three Down-Selected Conditions

Parameter #	Power (W)	Velocity (mm/s)	Hatch microns	Layer microns	Mode
1	1000	800	360	80	6
2	1000	1200	280	80	4
3	1000	1600	240	80	6

A repeatability study was conducted to see if the results obtained on the AMCM machine platform could be transferred to another platform. A successful repetition of the results on another platform would imply that the results obtained are indeed attributable to the beam shaping capabilities of the ring laser and not due to any benefits of the platform used. In addition to verifying repeatability and transferability the possibility of improving productivity at higher layer thicknesses was also investigated. The alternate platform selected was an Open Additive PANDA machine with an AFX ring mode laser. The build plate consisted of segmented cylinders, 1 through 4, with 16 segments each, solid cylinders, 5 through 8 and pads for single line scans. The build plate layout is shown in Figure 57. The segmented cylinders contained 16 segments each, with the build parameters for each segment presented in Table 20. The conditions for the solid cylinders to determine repeatability are identical to the those selected in the exploratory study given in Table 21. The builds were done with two different powders, supplied by EOS and Uniformity labs to compare the effect of powder size distributions on quality.

The x-ray CT results from the segmented cylinder builds were used to determine the impact of particle size distribution on quality. To make this comparison, the porosity was taken as the quality metric. Figure 58 depicts the comparison of quality between the EOS and Uniformity labs powders. Plotted in Figure 58 is the porosity for identical parameters for the two powders. It may be observed that more points fall below the line where quality is identical indicating that the quality achievable from the Uniformity labs powder is also better.
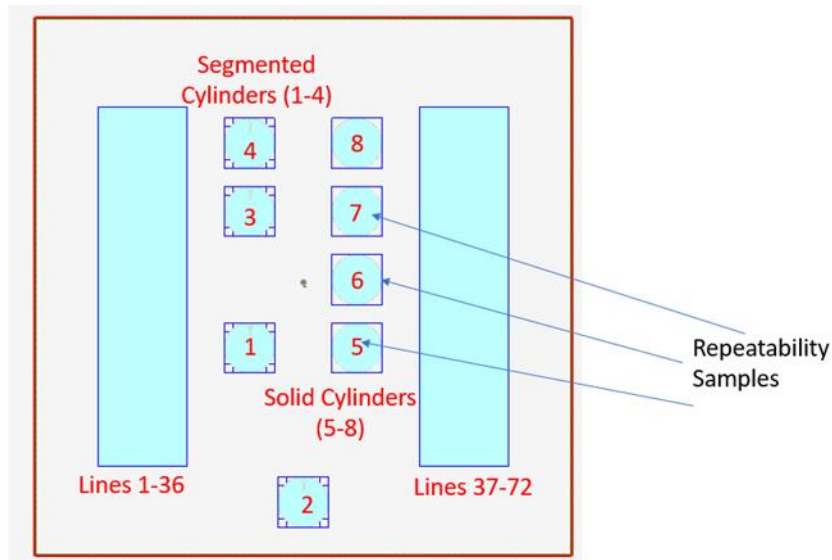
Figure 57.   Layout for Builds on Open Additive PANDA Machine

Table 20. Parameters for Segmented Cylinder Builds

	Mode Setting 0 Cylinder # 1/1C				Mode Setting 4 (Top Hat) Cylinder # 2/2C				Mode Setting 5 Cylinder # 3/3C				Mode Setting 6 (Donut) Cylinder # 4/4C			
	800 m/s	1200 m/s	1600 m/s	2000 m/s	800 m/s	1200 m/s	1600 m/s	2000 m/s	800 m/s	1200 m/s	1600 m/s	2000 m/s	800 m/s	1200 m/s	1600 m/s	2000 m/s
400 W	(170)-1	(170)-2	(170)-3	(170)-4	X	X	X	X	X	X	X	X	X	X	X	X
500 W	(200)-5	(200)-6	(200)-7	(200)-8	X	X	X	X	X	X	X	X	X	X	X	X
600 W	(220)-9	(220)-10	(220)-11	(220)-12	(240)-1	(240)-2	(240)-3	(240)-4	(240)-1	(240)-2	(240)-3	(240)-4	(240)-1	(240)-2	(240)-3	(240)-4
800 W	(240)-13	(240)-14	(240)-15	(240)-16	(260)-5	(260)-6	(260)-7	(260)-8	(260)-5	(260)-6	(260)-7	(260)-8	(260)-5	(260)-6	(260)-7	(260)-8
1000 W	X	X	X	X	(280)-9	(280)-10	(280)-11	(280)-12	(280)-9	(280)-10	(280)-11	(280)-12	(280)-9	(280)-10	(280)-11	(280)-12
1200 W	X	X	X	X	(300)-13	(300)-14	(300)-15	(300)-16	(300)-13	(300)-14	(300)-15	(300)-16	(300)-13	(300)-14	(300)-15	(300)-16

Table 21. Process Conditions for Single Line Scan Experiments

	600 m/s	800 m/s	1000 m/s	1200 m/s	1400 m/s	1600 m/s	1800 m/s	2000 m/s	2200 m/s	2400 m/s	2600 m/s	2800 m/s
Mode 4/ 1200 W	1	2	3	4	5	6	7	8	9	10	11	12
Mode 5/ 1200 W	13	14	15	16	17	18	19	20	21	22	23	24
Mode 6/ 1200 W	25	26	27	28	29	30	31	32	33	34	35	36
Mode 4/ 1200 W	37	38	39	40	41	42	43	44	45	46	47	48
Mode 5/ 1200 W	49	50	51	52	53	54	55	56	57	58	59	60
Mode 6/ 1200 W	61	62	63	64	65	66	67	68	69	70	71	72
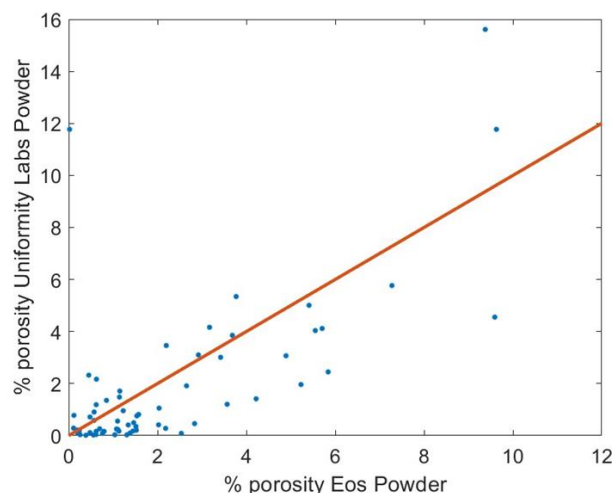
Figure 58. *Comparison of Porosity EOS Powder vs Uniformity Labs Powder*

The repeatability of results while moving from an AMCM platform to the Open Additive PANDA platform is summarized in Table 22. The three conditions selected as promising in Table 19 from the exploratory study were repeated with EOS powder on the Open Additive PANDA platform. The solid cylinders #5, #6 and #7 on the build plate, identified as "OSU 5", "OSU 6". and "OSU 7", are those used for determining repeatability. These cylinders "AMCM 8072", "AMCM 8026" and "AMCM 8070" correspond to OSU 5, OSU 6 and OSU 7 respectively in Table 22. It can be observed that OSU 6 and OSU 7 match AMCM 8026 and AMCM 8070 respectively across all three quality metrics of porosity, estimate of largest pore size and amount of connected porosity. However OSU 5 and AMCM 8072 do not match as the metrics for AMCM 8072 are an order of magnitude better than those of OSU 5. Hence the experiments to determine repeatability are inconclusive and more experiments are required draw statistically significant conclusions on repeatability.

Table 22. Quality Metrics for Comparison of AMCM and Open Additive PANDA Machine Platforms

Cylinder #	Power (W)	Velocity (mm/s)	Hatch microns	Layer microns	Diameter, mm	Mode	% porosity	Connected %	Max pore Size mm
OSU 5	1000	800	360	80	15	6	0.64	39	0.432
AMCM 8072	1000	800	360	80	15	6	0.025	0.97	0.197
OSU 6	1000	1200	280	80	15	4	0.05	2.82	0.201
AMCM 8026	1000	1200	280	80	15	4	0.079	3.17	0.262
OSU 7	1000	1600	240	80	15	6	0.23	12.30	0.337
AMCM 8070	1000	1600	240	80	15	6	0.218	9.29	0.421

Notwithstanding the conclusion regarding the repeatability of the parameters on the Open Additive PANDA machine, it was decided to obtain mechanical properties based on the conditions selected in Table 19. The layout of the build is shown in Figure 59. The color coding of the specimen location shows where corresponding to each of the three conditions were built. Twelve specimens, four from each parameter set in Table 19, were tested for tensile properties and the results are summarized in

Table 23. Specimens at locations (7,15,17,29) corresponding to Parameter 1, specimens at locations (8,23,26,36) corresponding to Parameter 2 and specimens at locations (9,16,28,29) corresponding to Parameter 3 were tested. The YS and UTS values are lower than typical values obtained on lower wattage Gaussian laser systems. However, the elongations obtained were greater than 10%, which is remarkable for as-printed AlSi10Mg material. Given the low porosity levels encountered with these parameters, this opens up the possibility of obtaining material with acceptable strength and ductility in the as-printed condition if the right parameters are chosen.
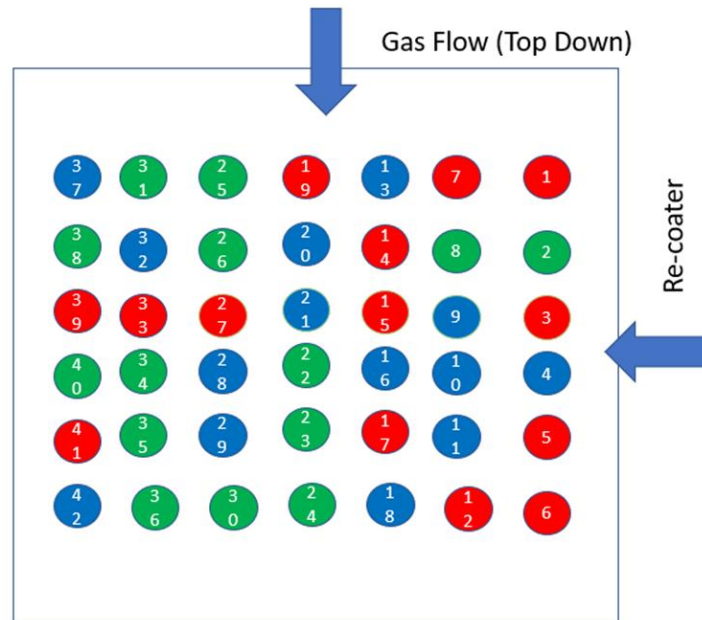
Figure 59. Layout of Specimens for Mechanical Property Evaluation

Table 23. Summary of Tensile Property Evaluation Results

Parameter #	Power (W)	Velocity (mm/s)	Hatch microns	Layer microns	Mode	Yield Strength (ksi)	UTS (Ksi)	Elongation %
1	1000	800	360	80	6	17.8	38.425	11.25
2	1000	1200	280	80	4	18.075	39.05	12
3	1000	1600	240	80	6	20.1	39.275	9

The significant conclusions that can be drawn from the high productivity work are that beam shaping technology of the AFX ring mode laser can be used to double the productivity obtained by 400W Gaussian systems with comparable quality. Printing rates of about 28-30mm3/second may be achieved. Furthermore, the particle size distribution of the powder employer can also be tailored to improve productivity and quality. The Uniformity labs powder can be expected to provide a 15% improvement in productivity. Additionally, superior elongation >10% may be expected for AlSi10Mg in the as-printed condition when using the AFX ring mode laser which opens up the possibility of obtaining acceptable properties in an as-printed condition, without the necessity of additional heat during heat treatment.

3.4 AM L-PBF Aluminum Component

The objective of this work reported in this section is to document the results of the Finite Element Analysis (FEA), Low Cycle Fatigue (LCF) test, dimensional and material inspection performed on the Eaton additive port and pressure plate P/N 859339, S/N 1. The prime intent of the testing was to evaluate the performance and characteristics of the additive port and pressure plate manufactured via L-PBF.

Analysis and LCF testing were conducted on an additive port and pressure plate P/N 859339, S/N 1, in general accordance with Eaton Specification 02-2771. The testing was intended to be a test until failure (crack initiation) based on a FEA simulation completed prior to the start of testing. However, the additive port and pressure plate P/N 859339, S/N 1 completed the LCF test. The testing did not result in any crack initiation.

The Eaton additive port and pressure plate P/N 859339, S/N 1 successfully completed the LCF test. The lack of crack formation indicate that the combination of materials properties and analysis approach used was conservative. Additional test time (test to failure) would help understand the analytical approach and lead to better utilization of the benefits of additive manufactured components (i.e., weight reduction, geometry complexity, etc.). It is recommended the testing documented herein be accepted as demonstration of conservative material properties being used in the FEA. Further testing is recommended to evaluate the actual cycles to crack initiation. AM port and pressure plates should continue to be evaluated for future production components.

The test unit was Eaton additive port and pressure plate P/N 859339, S/N 1. In practice, this component is part of a vane pump cartridge assembly that routes inlet and discharge flow to and from the pumping components. All components used were fabricated, inspected, and tested in accordance with the requirements of 859339. The test specimen was based on an existing machined design with various changes to utilize the benefits of AM. Some of the additive design features are shown in Figure 60 and described below. Comparison of the additive and wrought designs can be seen in Figure 61.

- Utilizing a "teardrop" core shape to ensure the component is self-supporting during the build process (i.e., no additional supports needed for a successful build).

- Utilizing 45° build angles to ensure the component is self-supporting during the build process (i.e., no additional supports needed in this location for a successful build).
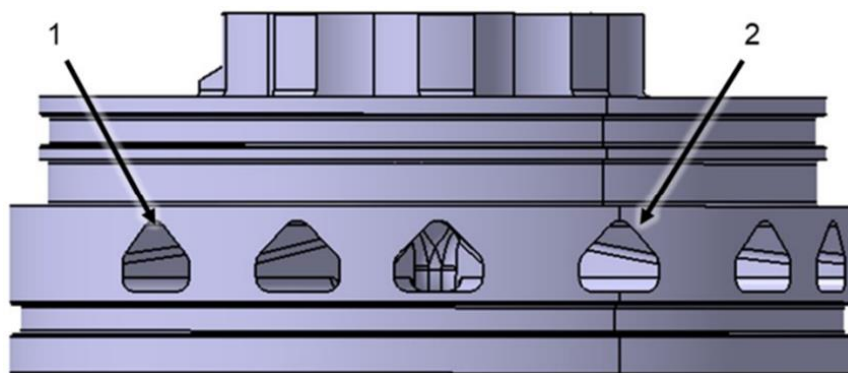
Figure 60. Additive Design
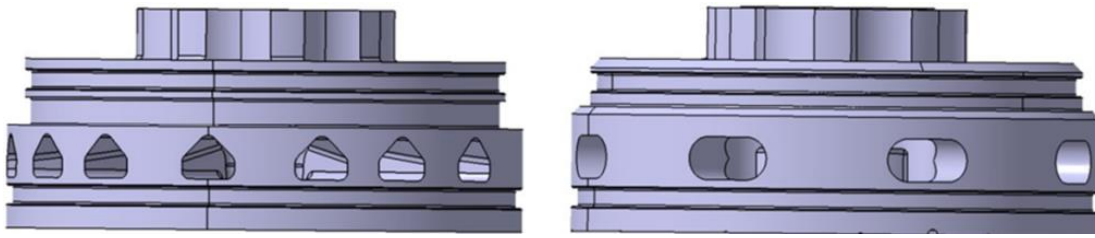
Figure 61.   Additive Design (left) and Wrought Design (right)

The component was manufactured from AlSi10Mg additive aluminum on the EOS M400-4 L-PBF machine. Following printing, the component underwent HIP and heat treatment processes in accordance with Eaton's qualified processes. The additive aluminum part had a tungsten carbide coating applied to the face via a cold spray process. The part was coated via VRC's Gen 3 system with nitrogen carrier gas. The coating material is VRC WC02 which is a wear resistant tungsten carbide-based powder. Chipping of the cold spray coating near the Outer Diameter (OD) and Inner Diameter (ID) of the part was observed during the machining process and is shown below in Figure 62 and Figure 63.
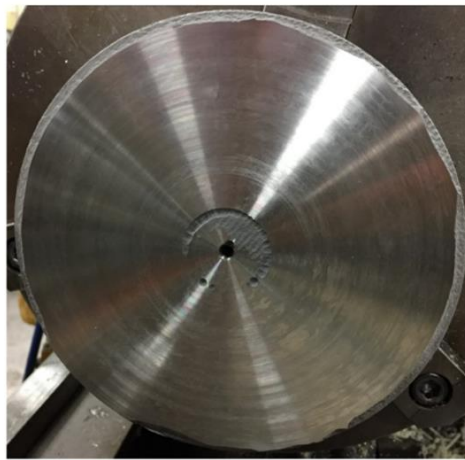
Figure 62.   In-Process Machining (1)
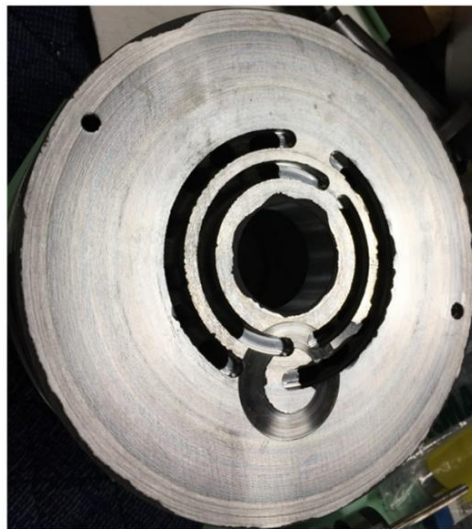
Figure 63.   In-Process Machining (2)

The test facility was in accordance with the requirements of 02-2771. Mobile SCH524 medium was used for the test. Testing was performed in test cell 33-30B at Eaton Euclid.

For the duration of testing, the maximum pressure rise was 50 to 300 psid above the required 2,000 psid due to test stand control of pressure and temperature. After 39,086 cycles, the minimum pressure on the test stand increased from a maximum of 20 psig, as required by Eaton Standard 02-2771, to a maximum of 60 psig for the duration of testing. The deviations listed above resulted in a more severe pressure cycle than required by 02-2771.

The test specimen underwent cyclic testing from 0 psid to 2,000 psid, minimum. A sample of the condition is shown in Figure 64. The test specimen was inspected for evidence of cracking in the high-stress location at various test intervals. The summary of pressure cycle count and inspection intervals is documented in Table 24. In total, the specimen underwent 141,246 cycles. At no time during the intermediate inspections was there any evidence of cracking in the high-stress location. A photograph of a typical intermediate inspection can be seen in Figure 65. The Eaton additive port and pressure plate P/N 859339, S/N 1, was subject to Fluorescent Penetrant Inspection (FPI) after completion of 80,479 and 141,246 cycles. FPI confirmed no cracking or indications within the printed structure.
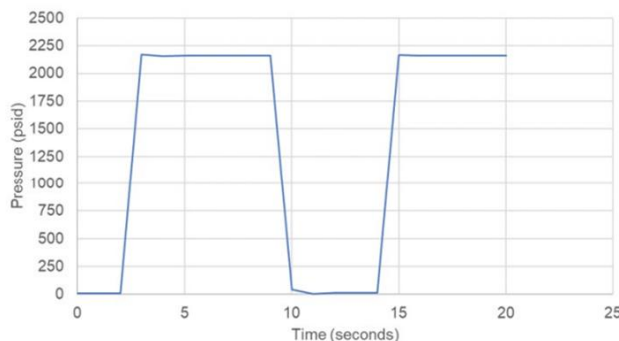
Figure 64.   Data Sample of Test Condition

Table 24.   Test Summary

No.	Description	Total Cycles Completed
1	Inspection	-
2	Pressure Cycle	2,572
3	Inspection	-
4	Pressure Cycle	9,906
5	Inspection	-
6	Pressure Cycle	16,643
7	Inspection	-
8	Pressure Cycle	27,212
9	Inspection	-
10	Pressure Cycle	39,086
11	Inspection	-
12	Pressure Cycle	59,780
13	Inspection	-
14	Pressure Cycle	80,479
15	Inspection	-
16	Pressure Cycle	111,177
17	Inspection	-
18	Pressure Cycle	141,246
19	Inspection	-

Figure 65.   Typical Intermediate FPI of AM AlSi10Mg
Port and Pressure Plate Component

3.5 Optimized AM EBM Titanium Component Design (L-PBF vs EBM)

The aim of this section is to outline the results and information gathered in the study and comparison of the Arcam Spectra-L EBM machine and the TRUMPF TruPrint 5000 L-PBF machine. Both machines are explicitly made for the purpose of 3D printing metal parts using titanium powder. This powder is distributed evenly across a build round plate and either laser or electron beam energy is used to melt and fuse the particles together.

3.5.1 Test Equipment

The first machine used was the Arcam Spectra L as shown in Figure 66. The Spectra L machine is a GE Additive machine which is described as having increased productivity and part cost reduction by up to 20% over other EBM machines. This is mainly driven by the speed at which it prints. It is advertised to be up to 30% faster than previous Arcam machines.

Figure 66.   Arcam Spectra L Machine
for EBM

A feature of the Arcam machine is that it allows for tightly packed parts which can be built using free-floating supports in sintered powder. Supports are primarily used for heat dissipation and are advertised to be easily removable after builds.

The Spectra L also features enhanced surface finish and consistent material properties for both thin and bulky parts. This is mainly due to the improvements in the melt process. Additionally, the build volume is the largest of the type coming in at Ø350mm x H430mm (13.7" x 16.9").

The second machine used was the TruPrint 5000 by Trumpf as shown Figure 67. The TruPrint is a Trumpf machine which is described as highly productive. Its biggest selling point is the 500°C preheating capability which essentially allows for builds to be completed hot, mitigating potential stress problems. Movement due to stress build up during printing is usually a problem for dimensional conformance.

Unlike the Arcam machines, supports cannot be built floating and need a connection point. In L-PBF processes, the supports are typically attached to the build plate or adjacent features. This is expected to make support removal a little more difficult.

The machine is advertised as fully automatic. Once the build cylinders are put into the TruPrint, the machine initiates the full process automatically. The melt happens using three 500W full field lasers simultaneously.

The TruPrint 5000 machine build volume is cylindrical coming in at Ø300mm x 400mm H (Ø 11.8" x 15.74" H).

Figure 67. TruPrint 5000 for L-PBF

3.5.2 Manufacturing Method

The Design for Additive Manufacturing (DfAM) was completed using CREO modeling software. The parts were changed to reduce sharp edges and remove squared features. It is often the case in additive that sharp corners and square features lead to potential issues when printing. The goal for this case study was to reduce/eliminate these as much as possible and use the exact same model for both methods of printing. Figures below show the transitions of the selected part geometry from initial design to a fully DfAM part.

The part shown in Figure 68 is a manifold. The left image is the original version of the part and the right image shows the part after DfAM modifications. To adapt it to the print process, the majority of the part's sharp edges were changed from sharp to radius.
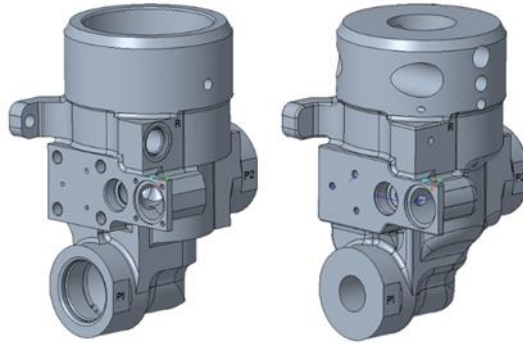
Figure 68.   Original (left) and DfAM (right) Manifold Models

The part in Figure 69 is a hydraulic manifold. The left image is the original version of the part, and the right image is the DfAM model. To adapt it to the print process the majority of the part's sharp edges were changed to a radius.
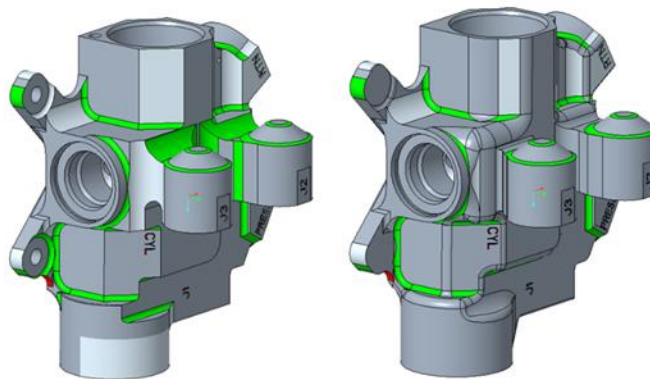
Figure 69.   Original (left) and DfAM (right) Hydraulic Manifold Models

The part in Figure 70 is a rotating hydraulic component. The left image is the original version of the part and the right image shows the DfAM model. To adapt it to the print process the majority of the part's sharp edges were changed from sharp to radius.
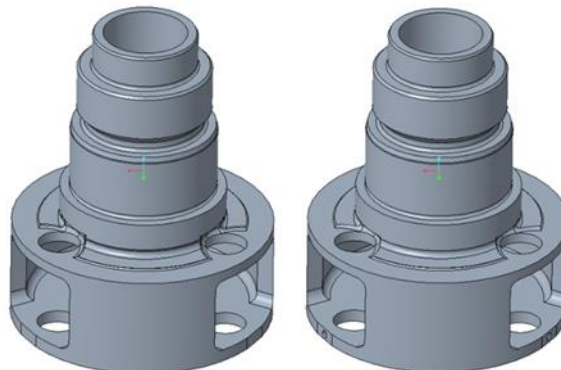
Figure 70.   Original (left) and DfAM (right) Rotating Hydraulic Component Models

The part shown in Figure 71 is an actuation lever. The original version of the part remained intact, and voids were filled to adapt it to the print process. Most the part's sharp edges were changed from sharp to radius.
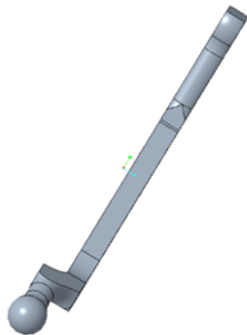
Figure 71.   Actuation Lever

Each part was optimized for 3D printing irrespective of which machine the parts would go into. Metal AM machines share most DfAM part geometry guidelines. Guidelines such as avoiding sharp edges and building geometry that is as much self-supporting as possible. Self-supportive geometry means features that are not strictly horizontal and greater than 45 degrees. This was completed for each part above to the extent possible and without modifying major geometries. The same parts were used for both L-PBF and EBM, and thus neither the L-PBF or EBM performed better.

3.5.3   Build Strategy, Machine Setup, and Operation

All parts utilized primarily block supports. These supports were all extended and connected to either the build plate or the part itself. Where possible some supports in the L-PBF models were angled to avoid supports adherence to the part itself. The supports were also generous as to avoid movement during the printing phase of the process. It can be shown that the supports are very similar or identi–cal for both applications, and thus neither EBM nor L-PBF has a distinct advantage in terms of support design. EBM does have a slight advantage in terms of number of builds. Since the EBM machine allows stacking, all of the parts could be fit into one build, and touch time on the machine was lower.

In AM, each machine has unique setup requirements to prepare the machine for a build. Some setup tasks are similar across different machine platforms, while other tasks are completely platform specific. Even for setup tasks that are common across all machines, such as powder loading, the way the tasks are executed are likely not identical and will have slight variations. A description of the setup tasks for both machines is highlighted below.

For EBM, the inside of the machine must be cleaned before every new build starts. A scraping tool is used to remove all black and flaking metallization from the door, protection shutters, chamber ceiling, and any other affected surfaces and then cleaned with isopropyl alcohol (IPA). Any powder and metallization flakes are vacuumed out of the machine. A cleaned build tank is then loaded into the machine. The Spectra L utilizes two different types of build plates: round and rectangular. The build for this project used a round build plate. The build plate is visually inspected for warpage or damage and all areas of the build plate are cleaned with IPA. The plate is loaded by aligning the through hole with any of the four alignment pins on the build platform, then aligning the slotted side

of the build plate with the opposite alignment pin. The amount of powder needed for a build is calculated based on the build height and volume, as well as an additional safety factor to ensure that there is more than enough powder for the build. The Spectra L uses a dual powder hopper system, so both hoppers were filled to be within 10 kg of each other and were then loaded into the machine.

Before each EBM build, the recoater rake teeth are inspected for damage. If the teeth appear to be bent, missing, or otherwise damaged, the teeth are removed and replaced with a new set. Once the rake teeth have been deemed acceptable or a new set has been installed, the assembly is reinserted into the machine. The build plate is moved until it appears to be approximately 0.5mm below rake teeth. Powder is fetched from one side then the rake is moved to the opposite rest position. Using a gloved hand, the build plate is covered with a thin layer of powder. The build plate is then moved upwards in increments of 0.1mm or less and the rake is sent to the opposite side rest position. The powder should appear speckled across most of the build plate if it is leveled correctly. If this is not the case, the build plate is adjusted using the two leveling wheels. This process is repeated until the build plate is properly leveled. When the plate is leveled, it is dropped down and the continuous fetch operation is run to fill the table and build chamber area with powder until the powder bed appears smooth. Powder is vacuumed from the top of the build plate, taking care to not disturb the surrounding powder bed. The metallization cone and protection foil are removed from the last build and new ones are inserted into the machine column. The heat shield is assembled and cleaned, then inserted into the machine. The chamber seal and sealing surface are cleaned and the chamber door is closed.

To prepare the Spectra L machine for the build process, the build file is loaded onto the machine and the powder for the build is confirmed. At this point, the vacuum process is begun. Once completed, the machine can be started. The process of preparing a build plate and cylinder, loading powder, and prepping the inside of the machine takes approximately 1.5 hours. The process of vacuuming the machine takes approximately 1.25 hours. Therefore, the entire process of preparing the Spectra L for a build takes approximately 2.75 hours to complete.

For L-PBF, initially the build plate is verified to have a smooth surface and meet designated flatness requirements. This helps with ensuring that the first few layers adhere correctly. The plate gets cleaned thoroughly with IPA, then the plate is loaded into an empty build cylinder that is sitting in the setup/depowdering station. Once the plate is set on the piston in the depowdering station, it's lowered all the way down to the bottom of the build cylinder. Then the cylinder is removed from the setup station, and a cleaned cylinder lid is placed on top. The build chamber must be properly cleaned before a new build can be started. The build chamber is vacuumed to remove any powder remaining from the previous build, as well as any soot buildup at the back of the chamber. The viewing window is wiped with IPA. The lasers and camera glass are carefully cleaned using lint-free lens wipes and high-purity IPA. From the setup/depowdering station, the cylinder is manually moved into the machine using the electric lift. Once set in the machine, the door is closed, and the cylinder is docked by following the load prompts on the machine's interface software. Once docked, the build plate is leveled inside the machine using a level and X and Y leveling screws underneath the plate. This adjustment is done prior to preheating since a level is used on the build plate surface directly.

In L-PBF, the amount of powder needed for a build is calculated based on the build height and volume, as well as an additional safety factor to ensure that there is more than enough powder for the build. All powder is sieved before going into the machine, whether the powder is virgin or reused.

For this project, virgin powder from powder lot 201-G0142 was used for both L-PBF builds. Once the virgin powder was sieved and deposited into a powder cylinder, the filled cylinder was loaded into the machine. A carbon fiber brush style recoater was used in the TruPrint 5000 for these builds. Before each build, the recoater assembly is removed from the machine to inspect the condition of the recoater brush. If the previous build failed or had part superelevation, the recoater brush may be damaged or missing bristles, in which case it needs to be replaced with a new brush. Once the recoater has been deemed acceptable, it is placed back into the machine.

The TruPrint 5000 has a filter system that collects the soot and condensate created during the building process. If the bin is full, it must be replaced before the next build can be started. Because the condensate is extremely reactive when exposed to oxygen, additional PPE must be worn and certain precautions have to be taken. The operator performing the bin swap must put on a fire-resistant jumpsuit, heat resistant gloves, fire-resistant hood, and a respirator. An additional operator must also be standing in the room with a Class D fire extinguisher at the ready in the case of an unexpected fire or reaction. The full bin is slowly removed from the machine and sealed with a lid, and an empty bin is installed into the machine. Once the build plate is leveled, powder cylinders are loaded, and the recoater is reinstalled, the process environment is ready to be prepared for the build. During this step, the build file is loaded onto the machine via network connection. By hitting the "Prepare Process Environment" button on the interface, the machine begins to preheat the build plate and purge the build chamber of oxygen. Although the machine can preheat the build plate up to 500°C, it was only preheated to 450°C for these builds to help reduce powder caking during depowdering. When the build plate and build chamber reach the necessary preheat temperature and oxygen concentration, the first layer can be set. Powder is dispensed and the recoater is sent back and forth until the gaps around the build plate are filled in with powder and a full layer of powder has been deposited on the build plate. The build plate is raised in small increments and then recoated again until an acceptable first layer of powder is achieved. Once the first layer is set, the build can be started. The process of preparing a build plate and cylinder, loading powder, and prepping the inside of the machine takes approximately 2 hours. The process of preheating and purging the build chamber of oxygen takes approximately 1 hour. Therefore, the entire process of preparing the TruPrint 5000 for a build takes approximately 3 hours to complete.

To compare the two platforms (L-PBF and EBM), it is apparent that the setup and preparation of these two machines is very similar in many aspects. For both, the initial setup consists of obtaining clean plates and securing the plates onto the machines. For both, it is important to start with clean and flat plates to mitigate any potential adhesion problems with the initial layers. Both machines require the correct amount of powder to be calculated based on build height and volume to ensure adequate coverage throughout. Similarly, both machines require careful inspection of the rake which is responsible for evenly distributing the bed of powder onto the build plate. The process of leveling the build plate is similar in that small increments up or down are completed until there is visual indication of even distribution of powder across the build plate. Lastly the start process of each machine is similar in that both require some pre-setup time to be ready to start the build.

The slight differences between the machines are as follows:

- For the Trumpf machine, the laser lens and camera glass need to be cleaned prior to any new build. The Spectra L does not have a lens, but it does require cleanup of buildup around the heat shield.

- The powder distribution system for the Spectra L is dual in nature and goes from right to left, then left to right. This process is repeated as the build grows. For the Trumpf machine, it goes from right to left and passes through two cylinders which are filled with powder. In the process it picks up the powder and lays it out evenly. It then returns to its previous position before melting occurs.

- The process of heating and purging both machines differ slightly in time but by only 0.25 hours.

Based on these similarities and differences, it can be concluded that the EBM process presents less challenges in setup and safety concerns, given that the EBM process does not contain any reactive process steps. In this example, two L-PBF builds were required compared to one EBM to produce the same number of parts. The EBM process is therefore more economical in terms of build setup, safety, and human touch time per part and shows a slight advantage.

3.5.4 Post-Print Handling and Depowdering

When the EBM build finishes, the machine must cool to below 80°C before the build cylinder can be removed from the machine. The cooled cylinder is removed from the machine and put into the recovery station where it is bulk depowdered.

After bulk depowdering, the parts are removed from the build cylinder and taken to the wet downdraft table in the post-processing area. Here, parts go through fine depowdering and support removal. After all supports and powder are removed from the parts, they are cleaned in an ultrasonic cleaner before proceeding to the next step.

When the L-PBF build finishes, the build cylinder is removed from the machine and placed into the cooling cabinet. Because the machine allows you to remove the build cylinder as soon as the build has completed, the cylinder can be as hot as 500°C. For this reason, the completed build is placed into a cooling cabinet, where the temperature of the cylinder is monitored by sensors, until it cools to below 60°C. After cooling, the build cylinder is loaded into the depowdering station and prepared for bulk depowdering of the build.

The depowdered build is removed from the build cylinder and any residual powder is blown off the plate using compressed air. A visual inspection of the build is completed, and photos of the build are taken. Because parts have to be connected directly to the build plate in L-PBF, the parts must be cut off of the build plate using a bandsaw or wire EDM. Due to limitations in the Charleston site's in-house capabilities, the build plates for all builds completed on the TruPrint 5000 are sent out to an external vendor to have the parts cut from the plate using a wire EDM.

When parts are returned from being cut off the plate, the supports are removed, and the parts are cleaned in an ultrasonic cleaner before moving to the next step.

The post-print handling for each machine is very similar. Both builds require time to cool down before bulk depowdering can start. Both machines have an external machine that helps with bulk depowdering.

Based on the similarities and differences, it can be concluded that due to external processing being required for the L-PBF Ti64 process, the EBM machine has a slight advantage. All processing can

be completed internally. Both processes are dependent on time to cool and require manual intervention to remove the powder cake onto a separate machine for major depowdering.

Bulk depowdering of the EBM parts is completed in the Powder Removal System (PRS) after the build cools and is removed from the machine. The PRS is used to blast the loose and semi-sintered powder away from the parts in the build cylinder. The PRS can be run in both automatic and manual modes, both of which are typically used for every build. As much powder as possible is removed by automatic blasting, then a technician manually blasts the parts to remove any powder left behind. The process of loading the build into the PRS and running the automatic and manual cycles takes approximately 3-4 hours on average, where the first 3 hours are automatic blasting and the last 0.5-1 hours are manual blasting.

After bulk depowdering is competed in the PRS, parts are removed and fine depowdering takes place in the wet downdraft table. Fine depowdering involves cleaning any trapped or sintered powder from the passages or surfaces of the parts using wires, picks, etc.

Depowdering of the EBM build was straightforward and relatively easy when compared to other EBM builds that have been printed in the Charleston lab. Much of this can be attributed to the lack of complex geometries and passages in the parts that would typically trap sintered powder. The standard automatic/manual blasting combination was run in the PRS, taking around 3 hours in total. Fine depowdering of the parts took approximately 30 additional minutes to clear sintered powder from some of the smaller part passages.

Bulk depowdering of the L-PBF parts is completed in the Trumpf depowdering station after the build cools and is removed from the machine. The depowdering station runs automatically after the build cylinder is loaded and all necessary depowdering attachments have been secured to the cylinder. The build cylinder is turned upside down in the depowdering station, and the loose powder is sucked out of the cylinder through a hose that is connected directly to the sieve. An ultrasonic probe is attached to the bottom of the build plate to facilitate the removal of powder from the parts. The process of prepping the cylinder for depowdering and running the automatic depowdering cycle takes approximately 30 minutes.

After bulk depowdering, the build plate is removed from the cylinder and fine depowdering takes place in the wet downdraft table. Fine depowdering involves cleaning any trapped or sintered powder from the passages or surfaces of the parts using wires, picks, etc.

Depowdering of Build 1 was very straightforward and simple. The automatic depowdering cycle run in the depowdering station removed the majority of powder from the parts, and the trace amounts left on and around the parts was blown off using compressed air.

Depowdering of Build 2 was more difficult and time consuming. While the automatic depowdering cycle removed all of the loose powder from the build cylinder, there was a significant amount of sintered powder that remained around the parts near the base of the build plate, as seen in Figure 72. This powder had to be manually broken up and chipped away by hand, which took approximately 45 additional minutes. The two parts from Build 2 also required approximately 15 minutes of fine depowdering once removed from the build cylinder in order to clear sintered powder from the passages of the parts.
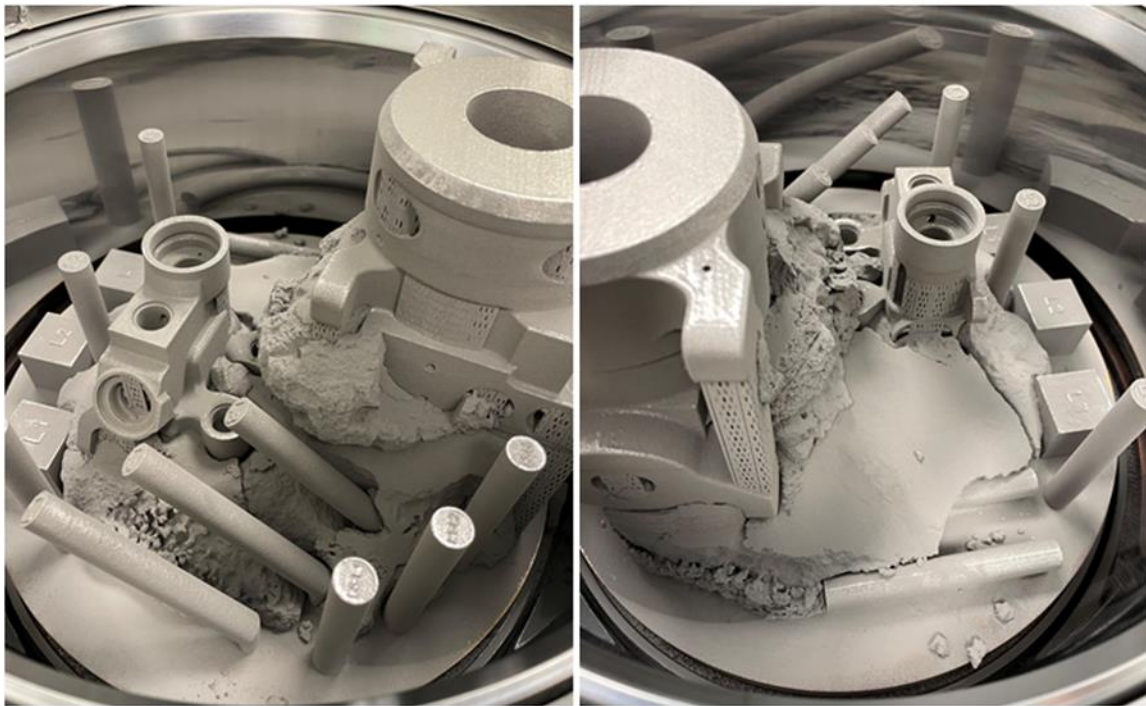
Figure 72. L-PBF Build 2 Sintered Powder

The process of post-build depowdering for both machines is very similar and typical of AM machines. Both machines use an external depowdering unit to aid in the bulk depowdering, which is automated. Post bulk depowdering, both machines require manual input for fine depowdering.

Based on the similarities and differences, it can be concluded that both the Trumpf machine and Arcam machine perform similarity in depowdering, with no clear advantageous process. Hands-on time depowdering the parts was 75 minutes for the L-PBF Trumpf parts and 90 minutes for the EBM parts. Given that there were two L-PBF builds for the one EBM build, the time difference can be considered negligible.

3.5.5 Support Removal and Thermal Processing and Chemical Milling

Given the similar times for the EBM parts and the L-PBF parts, EBM has a slight advantage. The EBM parts were able to achieve 100% support removal, while the L-PBF parts were unable to achieve full support removal. In a production setting, there may be design opportunities to eliminate the need for internal supports, but for the study purposes, the L-PBF process did not perform as well as the EBM process.

There is no advantage with one process versus the other in terms of thermal processing. The thermal processing of both parts was kept identical to compare both dimensional output and material property results.

EBM part #48992 was sent to chemical milling at an external supplier site, Precision Aerospace Corporation, in Rancho Cucamonga, CA. The part was chemically milled according to the following specifications: *Chemical mill with acceptance criteria IAW SAE AMS-C-81769, except for surface roughness requirements. Material removal requirement to be 0.019-0.021" per surface, from all*

surfaces. Material removal to be verified on an easily accessible flat surface or diameter. Record all post-chemical milling measurements. (SAE Standard AMSC81769, 2008).

Parts were visually inspected, and 3D scanned once received back from chemical milling. It was discovered that the EBM part had an area in which the chemical milling broke through the wall.

L-PBF part #48992 was sent to chemical milling at an external supplier site, Precision Aerospace Corporation, in Rancho Cucamonga, CA. The part was chemically milled according to the following specifications: *Chemical mill with acceptance criteria IAW SAE AMS-C-81769, except for surface roughness requirements. Material removal requirement to be 0.019-0.021" per surface, from all surfaces. Material removal to be verified on an easily accessible flat surface or diameter. Record all post-chemical milling measurements.*

Parts were visually inspected, and 3D scanned once received back from chemical milling. Because the L-PBF parts were not deburred or blended after supports removal, significant improvements were observed on the supported surfaces.

Neither the L-PBF nor the EBM process showed any advantages in chemical milling.

The chemical mill processing of both parts was kept identical to compare both dimensional output and material property results as well as any potential surface finish improvement.

Because both parts were not modeled with additional stock to account for the 0.020" chem mill removal amount, breakthrough was observed in at least one part. There were no initial plans of chemical milling. This process was introduced after the parts were already modeled for printing, so it can be concluded that this was a result of modeling and not the results of the process.

3.5.6 Dimensional Verification and Inspection

EBM parts were 3D scanned using a Keyence blue light scanner after support removal, HIP, chemical milling, and sectioning. Scans were exported as .stl files and then compared to the original as-grown CAD files using the Geomagics Control X software, an image for a representative part of which is shown in Figure 73.

Surface roughness measurements were taken on the parts using a Keyence optical profilometer after support removal, HIP, chemical mill, and sectioning. Surface roughness was measured using both areal average roughness (S_a) and R_a on the optical profilometer. Surface roughness results for the EBM parts can be found in Table 25 and Table 26. Table 25 shows the measurement results on the external surfaces of the parts. Table 26 shows the measurement results on the internal surfaces of the two parts that were sectioned.

L-PBF parts were 3D scanned using a Keyence blue light scanner after support removal, HIP, chemical milling, and sectioning. Scans were exported as .stl files and then compared to the original as-grown CAD files using the Geomagics Control X software, a representative image of which is shown in Figure 74.
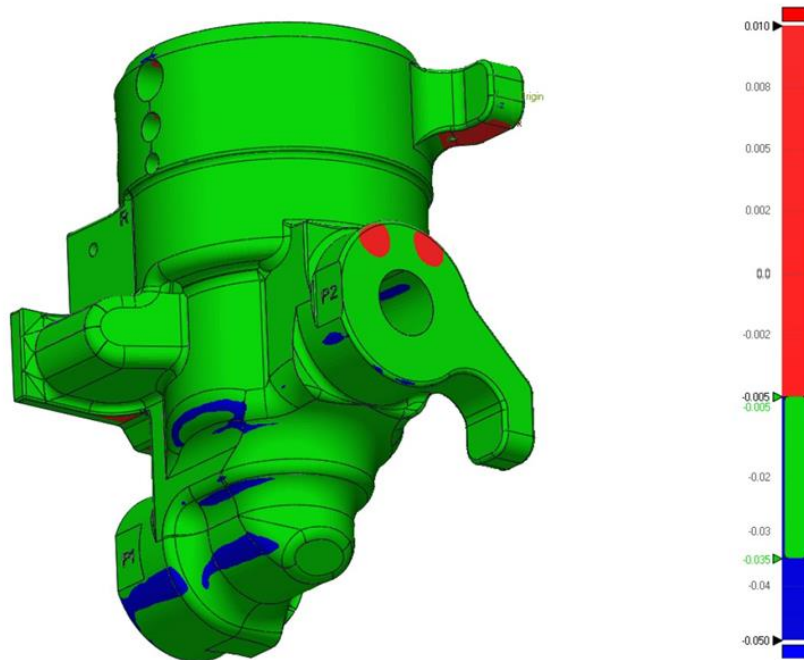
Figure 73. EBM PN 48992 to CAD Post-Chemical Milling
Scale bar is in inches

Table 25. EBM External Surface Roughness

Part	Condition	S_a (µin)	S_z (µin)	R_a (µin)	R_z (µin)	Surface Orientation
48992	HIP'd	913.7	17875.6	692.0	4352.2	Vertical
48992	HIP'd	247.0	4714.2	156.4	902.5	Horizontal
48992	Chem Milled	166.6	10712.6	81.3	525.1	Horizontal
48992	Chem Milled	217.5	2250.0	93.9	477.2	Vertical
50814	HIP'd	894.1	14802.0	723.1	4655.0	Vertical
50814	HIP'd	221.7	3390.6	54.0	344.2	Horizontal
57719	HIP'd	925.9	19156.3	614.0	3897.5	Vertical
57774	HIP'd	424.0	24704.3	82.4	500.2	Horizontal
57774	HIP'd	932.9	13166.1	660.0	4136.6	Vertical

Table 26. EBM Internal Surface Roughness

Part	Condition	S_a (µin)	S_z (µin)	R_a (µin)	R_z (µin)
50814	HIP'd	2136.0	37278.0	759.0	4588.8
50814	HIP'd	1317.1	28247.2	730.0	4500.0
48992	Chem Milled	218.6	2927.2	90.6	470.6
48992	Chem Milled	758.3	11229.5	87.7	468.2
48992	Chem Milled	1091.3	15167.3	104.2	499.6
48992	Chem Milled	306.0	4948.8	87.8	467.1

This information, as disclosed to DOD, shall not be modified without the written consent of NCMS.

83
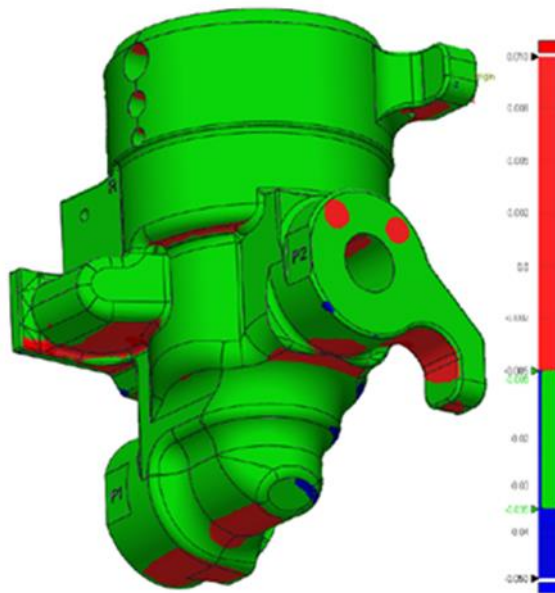
Figure 74. L-PBF PN 48992 to CAD Post-Chemical Milling

Surface roughness measurements were taken on certain L-PBF parts using a Keyence optical profilometer after support removal, HIP, chemical mill, and sectioning. Surface roughness was measured using both S_a and R_a on the optical profilometer.

Surface roughness results for the L-PBF parts can be found in Table 27 and Table 28. Table 27 shows the measurement results on the external surfaces of the parts. Table 28 shows the measurement results on the internal surfaces of the two parts that were sectioned.

Table 27. L-PBF External Surface Roughness

Part	Condition	S_a (µin)	S_z (µin)	R_a (µin)	R_z (µin)	Surface Orientation
48992	HIP'd	452.6	6539.4	370.5	2020.8	Vertical
48992	HIP'd	317.6	5822.8	242.2	1275.7	Horizontal
48992	Chem Milled	102.4	1325.6	49.1	289.9	Vertical
48992	Chem Milled	165.8	2136.2	64.1	355.4	Horizontal
50814	HIP'd	469.9	7813.4	373.0	2224.5	Vertical
50814	HIP'd	171.0	5036.2	84.1	501.8	Horizontal
57719	HIP'd	356.9	7558.0	271.8	1730.0	Vertical
57774	HIP'd	202.7	2563.4	127.8	736.2	Horizontal
57774	HIP'd	544.7	9525.2	327.5	1703.0	Vertical

Table 28. L-PBF Internal Surface Roughness

Part	Condition	Sa (µin)	Sz (µin)	Ra (µin)	Rz (µin)
50814	HIP'd	872.8	20052.4	343.2	1894.4
50814	HIP'd	1072.1	20953.9	339.5	1814.9
48992	Chem Milled	272.4	4804.7	65.7	374.6
48992	Chem Milled	475.1	9394.5	53.5	321.6
48992	Chem Milled	451.6	10284.6	60.0	348.1
48992	Chem Milled	126.6	1612.6	53.6	316.8

The dimensional results can be broken down into three distinct subsections for comparison: post-print, post-HIP and post-chemical milling.

Post-print, the dimensional results of EBM show that most dimensions meet a ±0.015" profile tolerance. There are locations which deviate as much as ±0.030" profile, but these are minimal and can be mitigated in subsequent builds. In comparison, the post-print L-PBF results show that the Trumpf machine outperformed the Spectra L in meeting the ±0.015" profile tolerance. The scan shows minimal areas of deviation of as much ±0.030" profile for all parts. In addition, most deviations are on the positive side, which makes it easier to work down into compliance through other forms of finishes. The results show a small advantage of the Trumpf machine over the Spectra L in meeting dimensional requirements post-print. Additional development could be used to develop better dimensional outcomes for both parts.

Post-HIP, the dimensional results for both the EBM and L-PBF show that there is minimal to no dimensional deviation due to movement of parts during the process. HIP is most often a process that distorts parts due to stress relief of the build process. This stress is minimized when parts are built at temperature. Since both machines build at temperature, the results go in line with very little move–ment since the stresses are already minimized during the build process. The results show no effect on this process for either machine.

Post-chemical milling, the dimensional results show very little deviation due to the chemical process. Neither process had a clear advantage or disadvantage of going through the chemical milling process.

Comparing surface roughness for EBM and L-PBF processes, the results show a clear advantage for the Trumpf L-PBF machine in surface finish. Post-print, the surface finish is better in L-PBF than EBM. However, post chemical mill, EBM receives a substantial improvement which results in the post-chemical milling EBM surface finish being close to the L-PBF post-chemical milling finish. L-PBF delivers a better surface finish post-print and post-chemical mill.

3.5.7 Material Testing

Tensile bars were printed on the EBM build with the purpose of being tested after completion of the build. One vertical, one horizontal, and one oblique (45° angle) tensile specimens were printed. The tensiles were all tested in the post-HIP condition. All tensiles were tested at an external supplier site, NSL Analytical, in Cleveland, OH. Test results can be found in Table 29.

Tensile bars were printed on the L-PBF build with the purpose of being tested after completion of the build. The TruPrint machine print uses three lasers, one of each tensile type (vertical, horizontal, oblique) was printed per laser. Additionally, three vertical coupons were printed using stitching. Stitching is when multiple lasers lase the same part, as opposed to a single laser lasing the entire part. The tensiles were all tested in the post-HIP condition. All tensiles were tested at an external supplier site, NSL Analytical, in Cleveland, OH. Test results can be found in Table 30.

The temperature processing for both L-PBF and EBM parts were kept the same. Post-print, the parts were processed to a standard HIP cycle most often employed on titanium material. This was done to allow a direct material comparison.

Table 29. EBM Tensile Testing Results

Specimen	Tensile Strength (PSI)	Yield Strength (PSI)	Elongation (%)	Reduction in Area (%)
Vertical Tensile (Top)	144,000	131,000	17	40
Vertical Tensile (Bottom)	141,000	130,000	19	47
Horizontal Tensile	138,000	123,000	12	23
45° Tensile	141,000	131,000	18	40

Table 30. L-PBF Tensile Testing Results

Specimen	Tensile Strength (PSI)	Yield Strength (PSI)	Elongation (%)	Reduction in Area (%)
Vertical Tensile SN L1	156,000	147,000	16	46
Vertical Tensile SN L2	153,000	141,000	16	46
Vertical Tensile SN L3	149,000	131,000	18	48
Horizontal Tensile SN L1	154,000	143,000	13	31
Horizontal Tensile SN L2	153,000	142,000	12	28
Horizontal Tensile SN L3	154,000	143,000	13	30
45° Tensile SN L1	151,000	136,000	15	41
45° Tensile SN L2	152,000	142,000	14	33
45° Tensile SN L3	151,000	140,000	15	46
Stitched Vertical Tensile SN L1/L2	152,000	141,000	16	49
Stitched Vertical Tensile SN L2/L3	153,000	137,000	15	46
Stitched Vertical Tensile SN L3/L1	155,000	146,000	16	49

The limited tensile specimen testing results show an advantage of tensile strength from L-PBF when compared to EBM. The YS is also higher in the L-PBF print. Elongation is comparable.

3.5.8 Conclusions

The AM of Ti64 parts using L-PBF and EBM technology was completed using the Spectra L (EBM) and the Trumpf TruPrint 5000 (L-PBF) machines. All parts were modified using best DfAM practices to make them easier to print. The same parts were printed using both technologies. Similarly, the support strategy was kept the same for ease of comparison. These parts ranged from medium-sized bulky manifolds (approximately 6" x 6" x 6") to thinner walled rotating parts (3" x 3" x 3").

For the machine setup and preparation as well as the post-print handling, it was found that both technologies require similar input and time to operate. EBM has a slight advantage over the L-PBF due to being able to stack parts, as this project only required one EBM build and two L-PBF builds to complete. Depowdering the parts can be considered equivalent on these parts for both processes.

The support removal required for these parts is where the EBM process showed significant advantages over the L-PBF process. All supports were able to be removed from the parts in EBM, but multiple supports remained inside of the parts in L-PBF. This indicates that on complex internal geometry, where the parts haven't been initially designed for AM, the EBM process offers more design flexibility and increased part success.

Dimensional results play a large role in the selection of AM technologies. The results show similar dimensional outcomes of the parts, with a slight advantage going to the L-PBF components. Both EBM and L-PBF processes would likely benefit from additional DfAM work on these components, which would further reduce the L-PBF advantage. Since the L-PBF process left internal supports on the part, these areas would be not fit for use in the field, and therefore the part would not function as intended. No significant advantage or disadvantage could be seen dimensionally for both the bulky manifold parts and the smaller lever part, indicating equivalent dimensional processes. The results do show a better surface finish using the L-PBF process. This outcome is reduced through chemical milling, but it can be concluded L-PBF parts have a better surface finish vs similar EBM parts.

In this study the tensile material performance shows a slight advantage using the Trumpf TruPrint 5000 L-PBF machine when compared to the Arcam Spectra L EBM machine. Additional materials testing is required to not only build out statistically significant datasets, but also determine if the type of powder, machine or AM process is the largest contributor to material performance. Increased material performance using L-PBF machines coupled potentially allow for more margin in designs where both L-PBF and EBM are options.

In conclusion, both the EBM and L-PBF processes were able to produce parts in a very similar fashion. The overall design freedom that is enabled using EBM along with the reduced per part human interaction and touch time slightly pushed the EBM to be favored over L-PBF for the geometries studied. To continue to build on this work, more material testing could be conducted using a variety of machine types and powder types. Additionally, more varied geometry could be used to better correlate geometry to the optimum AM process.

3.6 AM EBM Titanium Component

This section describes the manufacturing, testing and analysis of Ti-6Al-4V (Ti64) parts produced using EBM. Parts (manifolds) of three material conditions were produced and tested. The material conditions tested were: no chemical milling, 0.010" chemical milling and .020" chemical milling. This project built on the activities performed on Phase I of this project. During Phase I, all EBM parts were produced using an Arcam Q20+ machine. For Phase II of the project, these parts were produced using an Arcam Spectra L EBM machine. In addition to the variable of changing the machine, during Phase II the HIP schedule was varied and used between the two identical part lots to compare material performance.

In addition to the fatigue testing studies, a comprehensive dimensional study was performed throughout the full build volume of two separate Arcam Spectra L machines. Three full height builds containing 30 parts each were completed on each machine. Identical build files were used for all builds, and the components within each build were spread throughout the volume to create a full survey. Thirteen (13) features on each produced part were measured in the as-grown state, and compared to parts within the same build, on the same machine, and on the other identical machine.

The outcomes and observations of this section will answer the requirements of the AMoCC project deliverable as well as feed into multiple ongoing Eaton development activities.

3.6.1   Component Design

One of the common uses for AM technology at Eaton is hydraulic manifolds. The part designed for this project can be considered a small, representative sample of likely manifold geometry, which learnings can be broadly applied across multiple product lines. The AMoCC Phase II project built on the learnings from Phase I. During Phase I, the produced parts were designed near the unlimited life area of the fatigue curve, which led to non-failure of multiple manifolds during fatigue testing, very high cycle counts and test time, if the parts did fail. For Phase II, the parts were redesigned to increase the localized stress, by reducing wall thickness, and inducing failure faster. The final design configuration can seen in Figure 75 and a comparison of the high stress location wall thickness of the Phase I design and the Phase II design can be seen in Figure 76.
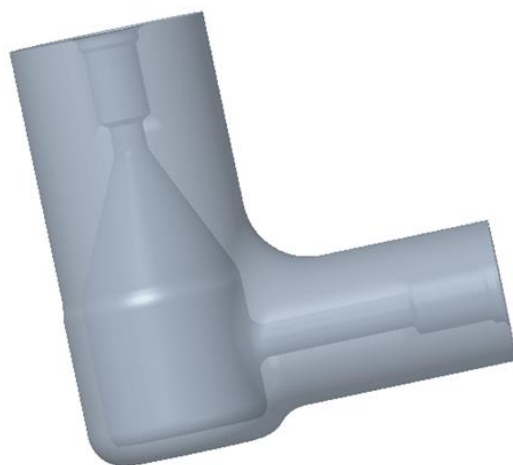
Figure 75.   AMoCC Phase II Manifold Design
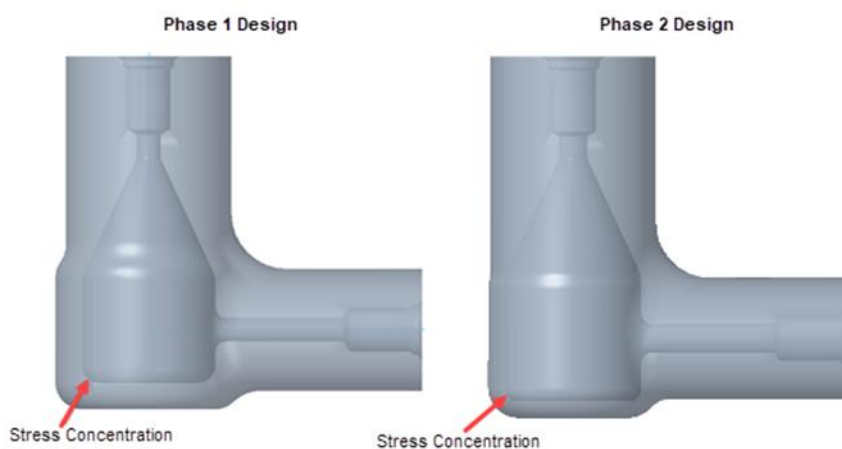
Figure 76.   Stress Concentration Wall Thickness Comparison,
Phase I Design vs Phase II Design

As introduced above, the objective of the AMOCC Phase II project was to determine the effect of removing material from the surface of a Ti64 part, using chemical milling, on fatigue performance. Specifically, the AMOCC Phase II project looked at parts produced on the Arcam Spectra L Electron Beam Powder Bed Fusion machine. Three different levels of chemical milling material removal were performed, 0" (or as-grown), 0.010" and 0.020". In order to ensure the chemical milling level was the only variable in manifold performance, three separate as-grown configurations were created.

One was the base (as-grown) model, the second was the base model with an additional 0.010" material added to each surface and the third was the base model with 0.020" added to each surface. Doing this ensured that the wall thickness remained the same even after chemical milling. Uniform wall thickness would also ensure the stress experienced by the manifold at the stress concentration would be uniform. One part number was used to machine and inspect all manifolds. Table 31 shows the Eaton part number associated with each configuration and outlines the part hierarchy.

Table 31. Manifold Drawing List

Part Number	Description	Hierarchy
99643-60025	Manifold, Machined	1
99643-60022-101	Manifold, Post Chem Mill (0.020")	2
99643-60022-100	Manifold, As-Grown (0.020")	3
99643-60023-101	Manifold, Post Chem Mill (0.010")	2
99643-60023-100	Manifold, As-Grown (0.010")	3
99643-60024-100	Manifold, As-Grown (No Chem Mill)	2

3.6.2 Manufacturing

As described above, this project consisted of manufacturing multiple manifolds using EBM with Ti64 material. All components were produced using an Arcam Spectra L machine, with the same build theme. For the hydraulic fatigue testing effort, eight manifolds in each configuration were printed, 24 manifolds in total. This effort was then duplicated for the second HIP schedule with another 24 manifolds being produced. In addition to printing, the parts went through depowdering and support removal, HIP, grit blasting, chemical milling, 3D scanning, FPI, machining and radiography.

For the dimensional repeatability study two separate Spectra L machines were used. One geometry was chosen and repeated throughout the build chamber. These parts only went through printing, depowering, support removal and inspection steps. Additional details can be found below.

In addition to doing a comparison between the Arcam Q20+ and Arcam Spectra L machines, a comparison was also run between two different HIP schedules. The initial, first batch, requirement call out is listed in Figure 77, and the updated HIP schedule is listed in Figure 78.

HIP IN APPROVED ORIENTATION, UNDER AN INERT ATMOSPHERE AT 14750 PSI +/- 250 PSI AT 1650°F +/- 25°F FOR 2 HRS +15/-0 MIN. THE PART SHALL BE COOLED UNDER INERT ATMOSPHERE IN THE AUTOCLAVE TO BELOW 800°F. COOL FROM 800°F AT ANY RATE. CARBON LINED FURNACES SHALL NOT BE USED.

Figure 77. First Batch, HIP Requirement Note

WRAP PARTS IN 300 SERIES STAINLESS STEEL FOIL PRIOR TO HIP. HIP IN ORIENTATION SHOWN, UNDER AN INERT ATMOSPHERE (ARGON) AT 14750 ± 250 PSI AT 1650°F ± 25°F FOR 2 HRS +15/-0 MIN. THE PARTS SHALL BE COOLED UNDER INERT ATMOSPHERE IN THE AUTOCLAVE TO BELOW 800°F AT A RATE NOT TO EXCEED 18°F/MIN. COOL FROM 800 °F AT ANY RATE. CARBON LINED FURNACES SHALL NOT BE USED.

Figure 78. Second Batch, HIP Requirement Note

Identical builds were run on two Spectra L machines located in Eaton's Charleston-based Digital Design and Additive Manufacturing Center (DDAMC). Each machine ran the build three times, allowing comparisons to be made about each machine's repeatability to itself and to the other machine. Job information is found in Table 32. Since the Spectra L is a new machine, there is little

This information, as disclosed to DOD, shall not be modified without the written consent of NCMS.

89

DISTRIBUTION STATEMENT A. Approved for public release. Distribution is unlimited. OPSEC#9316

to no data related to this in the industry, especially regarding machine-to-machine variation. Below is a table of the builds that were run along with any special considerations that took place for each build. Spectra L SN 1522 shall be henceforth referred to as "Obi 1" and Spectra L SN 1512 shall be referred to as "Obi 2".

Table 32. Job Information

Job Number	Machine	Date	Special Notes
EB-D23-043	Obi 1	9/18/23	
EB-D23-048	Obi 1	10/2/23	NOTE: This build was run using an old support strategy and the data should NOT be compared.
EB-D23-052	Obi 1	10/16/23	
EB-D23-037	Obi 2	8/14/23	NOTE: This build had less specimens and had to be stopped at ~315mm due to machine mechanical issues. Data until that point shall be used
EB-D23-045	Obi 2	10/16/23	
EB-D23-047	Obi 2	10/23/23	

As noted above, the engineer who created the build file mistakenly forgot to remove an older revision of the file from the machine. An older version was run on Obi 1 build that did not have sufficient support material added and therefore had swelling in the parts. Since these parts had swelling, they should not be considered when doing a repeatability study, as the build file and support structures were different.

The machines were setup by certified machine operators following standard operating procedures to reduce variation from machine setup. Each machine had a dedicated chiller and helium supply. A photo of the printing environment can be seen in Figure 79. The machines were strategically placed so that the columns were far enough apart that the machines did not interfere with each other.

To represent the entire build volume, geometric specimens described above (99643-60022-100) were placed strategically throughout X, Y, and Z. The Spectra L printers have a maximum diameter of 350mm and a maximum height of 430mm. A photo of the build setup can be seen in Figure 80.

Figure 79.   Additive Manufacturing Facility
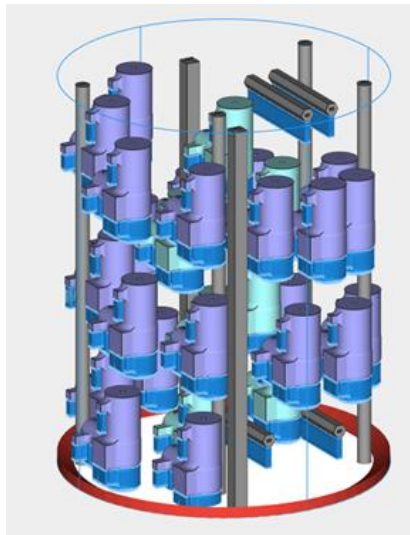
Figure 80.   Repeatability Build Layout

The build contained 30 manifolds of total volume 319,000 cubic millimeters. With added support structures, the total volume of the build was 381,000 cubic millimeters. Per standard protocol, witness coupons were added to the build. The build contained two full height vertical square bars, four full height vertical cylindrical parts, and 4 horizonal specimens placed at the bottom and top of the build. A photo containing only the coupons can be found in Figure 81.
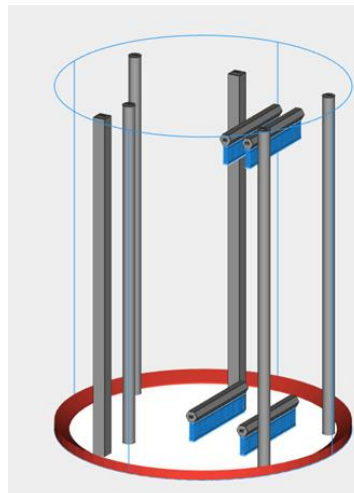
Figure 81.   Coupons in Build Layout

Each specimen was supported in the same fashion. The three overhangs were supported using a lighter, less-aggressive strategy that consisted of a border and fins as shown in Figure 82.

The remainder of the body was supported using a dense block strategy that better aids in heat dissipation. These supports support a large volume of part and therefore need to be more aggressive to properly dissipate the heat and prevent distortion. The supports were deliberately picked to go up the sides of the part to prevent distortion. Per standard protocol, the file output was checked for various issues that are common when producing triangulated models. This part had no issues, as shown by the diagnostics that were run.
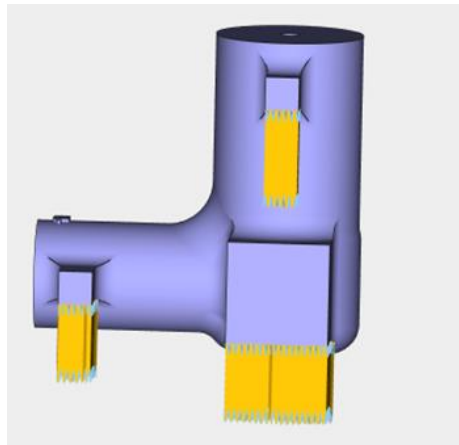
Figure 82.   Specimen Support Strategy

It should be noted that Spectra L machines are highly sensitive to the size of the part and the thermal profile. This geometry was chosen because it allowed the entire build volume to be sampled and represents a common part size printed at the facility. The results of this study will not be applicable to all parts of any size.

The job was configured using the Arcam Spectra L configuration in Materialize Magics. Parts were assigned a melt theme and supports were assigned a wafer theme, which was recommended by Arcam to be used for support material.

After configuration, the build was processed into an .abp file which was uploaded to both machines. After the build, the parts were taken to the post-processing area for support removal and deburring. A photo of the support removal area can be seen in Figure 83. Once all six builds were processed, the parts were taken to on-site inspection. A Zeiss Contura 3 was used for inspection with a trained programmer. The program took 8 minutes and 50 seconds per part. All reports were compiled into a single report table for analysis.

Figure 83.   Post-Processing Area

3.6.3 Hydraulic Impact Fatigue Testing

Similar to the objectives in Phase I of the AMoCC project, fatigue testing, specifically hydraulic impulse, was conducted to compare and contrast part material performance. Hydraulic impulse testing is common in hydraulics and the outcomes of this work will have broad applications for EBM Ti64 manifolds throughout the business. All testing was conducted at the Eaton Los Angeles Engineering Test Lab.

Each batch of parts was tested in three separate groups. One group of eight that was tested were the as-grown samples, serial #024 A-H and #024 A2-H2. The second group of eight that was tested were the 0.010" chemical milled material removal samples, serial #023 A-H and #023 A2-H2. The last group of eight that were tested was the 0.020" chemical milled material removal samples, serial #022 A-H and #022 A2-H2.

Each of the groups were tested using the same setup and test stand. The testing consisted of impulse pressure spikes following a pre-determined curve, found in EEWO-BC-01192023-001 Rev – for the first batch of parts and EEWO-BC-08282023-001 Rev – for the second batch of parts. The manifolds were continually cycled, with cycles being counted, until a leak was observed and recorded. When a leak was found, the testing was paused, the failed manifold was removed and the remaining mani–folds continued testing. This process was repeated until all eight of the manifolds in the group had failed.

After testing was completed on the first batch of parts, the manifolds were sent to the Eaton Materials Lab for failure investigation and fractography. Due to the length of testing, only the S/N 024 manifolds from the first batch were able to be sent for evaluation.

A custom setup was designed and built to test the AMoCC manifolds in the Eaton Los Angeles Engineering Test Lab. This setup and stand conducted the required impulse testing using MIL-PRF-83282 hydraulic fluid. In addition, this test stand also included multiple fluid sensors which, when exposed to liquid, stopped test cycling. Using these sensors prevented over cycling when a failure was detected in a test group.

A summary of the test cycle results is shown in Table 33, Table 34, and Table 35. Table 33 shows the test results from the first batch of parts tested for the AMoCC Phase II project, with the initial HIP schedule. Table 34 shows the second bath of parts tested for the AMoCC Phase II project, with the revised HIP schedule. Table 35 shows the results previously presented in AM-ER-0041 detailing the AMoCC Phase I test results. Table 35 is only included in this report as a basis of comparison and no additional testing or experimentation relating to Phase I of the project was completed.

Phase II of the AMoCC project did not include as much analysis work as Phase I. The analysis work from Phase II consisted of validating the updated high stress area wall thickness.

After testing was completed on the first group of fatigue manifolds, all the failed manifolds were sent to the Eaton Euclid Materials Lab for evaluation. Sectioning, failure location studies, FPI and detailed macro, micro and SEM images were taken for each of the studied manifolds.

Table 33. AMoCC Phase II, Initial HIP Schedule, Impulse Testing Summary

Part Serial Number	Surface Condition	Impulse Pressure	Cycles at Failure	Average Cycles at Failure
AMOCC Phase II First Batch				
024 A	As-Grown	450-4500-450 psi	Did Not Test	63,357
024 B	As-Grown	450-4500-450 psi	58,852	
024 C	As-Grown	450-4500-450 psi	58,396	
024 D	As-Grown	450-4500-450 psi	68,824	
024 E	As-Grown	450-4500-450 psi	63,938	
024 F	As-Grown	450-4500-450 psi	74,259	
024 G	As-Grown	450-4500-450 psi	56,763	
024 H	As-Grown	450-4500-450 psi	62,465	
023 A	0.010" CM	450-4500-450 psi	Did Not Test	96,491
023 B	0.010" CM	450-4500-450 psi	102,115	
023 C	0.010" CM	450-4500-450 psi	100,193	
023 D	0.010" CM	450-4500-450 psi	90,749	
023 E	0.010" CM	450-4500-450 psi	91,104	
023 F	0.010" CM	450-4500-450 psi	96,271	
023 G	0.010" CM	450-4500-450 psi	Did Not Test	
023 H	0.010" CM	450-4500-450 psi	98,514	
022 A	0.020" CM	450-4500-450 psi	Did Not Test	150,113
022 B	0.020" CM	450-4500-450 psi	133,845	
022 C	0.020" CM	450-4500-450 psi	138,721	
022 D	0.020" CM	450-4500-450 psi	155,667	
022 E	0.020" CM	450-4500-450 psi	Did Not Test	
022 F	0.020" CM	450-4500-450 psi	145,748	
022 G	0.020" CM	450-4500-450 psi	164,509	
022 H	0.020" CM	450-4500-450 psi	162,185	

Table 34. AMoCC Phase II, Updated HIP Schedule, Impulse Testing Summary

Part Serial Number	Surface Condition	Impulse Pressure	Cycles at Failure	Average Cycles at Failure
AMOCC Phase II Second Batch				
024 A2	As-Grown	450-4500-450 psi	61,084	80,239
024 B2	As-Grown	450-4500-450 psi	88,520	
024 C2	As-Grown	450-4500-450 psi	84,065	
024 D2	As-Grown	450-4500-450 psi	86,633	
024 E2	As-Grown	450-4500-450 psi	77,385	
024 F2	As-Grown	450-4500-450 psi	77,703	
024 G2	As-Grown	450-4500-450 psi	78,004	
024 H2	As-Grown	450-4500-450 psi	88,520	
023 A2	0.010" CM	450-4500-450 psi	Did Not Test	Did Not Test Due To Project Timing and Test Stand Availability
023 B2	0.010" CM	450-4500-450 psi	Did Not Test	
023 C2	0.010" CM	450-4500-450 psi	Did Not Test	
023 D2	0 010" CM	450-4500-450 psi	Did Not Test	
023 E2	0.010" CM	450-4500-450 psi	Did Not Test	
023 F2	0.010" CM	450-4500-450 psi	Did Not Test	
023 G2	0.010" CM	450-4500-450 psi	Did Not Test	
023 H2	0.010" CM	450-4500-450 psi	Did Not Test	

Table 34. AMoCC Phase II, Updated HIP Schedule, Impulse Testing Summary (continued)

AMOCC Phase II Second Batch				
Part Serial Number	Surface Condition	Impulse Pressure	Cycles at Failure	Average Cycles at Failure
022 A2	0.020" CM	450-4500-450 psi	No Failure	
022 B2	0.020" CM	450-4500-450 psi	No Failure	
022 C2	0.020" CM	450-4500-450 psi	No Failure	>706,162
022 D2	0.020" CM	450-4500-450 psi	No Failure	
022 E2	0.020" CM	450-4500-450 psi	No Failure	No Failures During Testing
022 F2	0.020" CM	450-4500-450 psi	No Failure	
022 G2	0.020" CM	450-4500-450 psi	No Failure	
022 H2	0.020" CM	450-4500-450 psi	No Failure	

Table 35. AMoCC Phase I Impulse Testing Summary

AMOCC Phase 1 Test Data				
Part Serial Number	Surface Condition	Impulse Pressure	Cycles at Failure	Average Cycles at Failure
874 A	As-Grown	0-4500-0 psi	690,650	
874 B	As-Grown	0-4500-0 psi	615,083	
874 C	As-Grown	0-4500-0 psi	706,186	
874 D	As-Grown	0-4500-0 psi	673,971	647,310
874 E	As-Grown	0-4500-0 psi	833,522	
874 F	As-Grown	0-4500-0 psi	322,641	
874 G	As-Grown	0-4500-0 psi	721,345	
874 H	As-Grown	0-4500-0 psi	615,083	
873 A	0.010" CM	0-6000-0 psi	No Failure	
873 B	0.010" CM	0-6000-0 psi	No Failure	
873 C	0.010" CM	0-6000-0 psi	430,213	>418,756
873 D	0.010" CM	0-6000-0 psi	No Failure	
873 E	0.010" CM	0-6000-0 psi	409,166	Not all testing was able to be completed
873 F	0.010" CM	0-6000-0 psi	408,711	
873 G	0.010" CM	0-6000-0 psi	491,182	
873 H	0.010" CM	0-6000-0 psi	354,508	
793 A	0.020" CM	0-6000-0 psi	No Failure	
793 B	0.020" CM	0-6000-0 psi	No Failure	
793 C	0.020" CM	0-6000-0 psi	No Failure	
793 D	0.020" CM	0-6000-0 psi	No Failure	No Failures During Testing
793 E	0.020" CM	0-6000-0 psi	No Failure	
793 F	0.020" CM	0-6000-0 psi	No Failure	
793 G	0.020" CM	0-6000-0 psi	No Failure	
793 H	0.020" CM	0-6000-0 psi	No Failure	

3.6.4 Repeatability Study

In addition to the fatigue study detailed above, a dimensional repeatability study was performed to determine the in-build, in-machine and between machine dimensional variability in the EBM process. Three full height builds containing 30 parts each were completed on each machine. Identical build files were used for all builds, and the components within each build were spread throughout the volume to create a full survey. Thirteen features on each produced part were measured in the as-

grown state, and compared to parts within the same build, on the same machine, and on the other identical machine.

As described previously, a Zeiss Contura 3 was used to measure each of the parts. A sample report that was output is shown in Table 36. A report was generated for each part before being compiled into a single document that contained all data from all builds.

Table 36. CMM Dimensionally Output Example

Calypso Measuring Result					
Measurement Plan 60022-100_1_Manifold Chem-Milled Stock_11-16-23	**Date** 17-Nov-23	**Order** EB-D23-037			
Drawing No. 60022-100	**Time** 10:33:20	**Part No.** 3			
Operator Master	**CMM**				
Characteristic	**Actual**		**Upper Tol**	**Lower To**	**Deviation**
1,1 1.915_Y		1.8641811	0.03	-0.03	-0.0508189
2,1 Ø.210		0.1975186	0.03	-0.03	-0.0124814
3,1 1.895_Y		1.8632827	0.03	-0.03	-0.0317173
4,1 Ø1.100		1.0819628	0.03	-0.03	-0.0180372
5,1 2.000_Z		1.9761824	0.03	-0.03	-0.0238176
6,1 1.040_Z		1.0201355	0.03	-0.03	-0.0198645
7,1 1.040_X		1.035343	0.03	-0.03	-0.004657
8,1 2.000		-2.0002016	0.03	-0.03	-0.0002016
9,1 .340		0.3437416	0.03	-0.03	0.0037416
10,1 .340		0.3310867	0.03	-0.03	-0.0089133
11,1 Ø1.500		1.4769408	0.03	-0.03	-0.0230592
12,1 1.695_Y		1.6660144	0.03	-0.03	-0.0289856
13,1 .210		0.2168937	0.03	-0.03	0.0068937

For this study, the measured deviation from the nominal feature dimension was viewed as more critical and therefore is presented in the tables below. It should be noted that as described above, Build 2 from machine Obi 1 was found to be an error, and thus not included in the dimensional analysis. Table 37 shows the height of the part off of the build plate along the Z-axis. Both the feature type and height off of the build plate are possible variables that could lead to part-to-part variation. As previously mentioned, the orientation of all parts remained constant relative to the machine and all the supports were identical.

Taking the information from earlier in this section, multiple dimensional studies and comparisons were conducted.

Looking at Obi 1 Build 1, the standard deviations of the recorded nominal measurement deviations ranged from 0.0016" to 0.010". Obi 1 Build 3 had a similar deviation pattern with the standard deviation of the recorded measurement deviations ranging from 0.0019" to 0.0055". This indicates, even tighter part repeatability and overall, more uniform parts. It is worth noting that, all three of the highest deviations for both builds occurred on unsupported side skin surfaces. All three of these feature dimensions were from an unsupported upskin, to a supported downskin. This tends to go against the assumption that supported surfaces would show greater dimensional inconsistency due to the support removal process.

On the Obi 2 machine a similar pattern can be seen with standard deviations ranging from 0.0013" to 0.0060" in Build 1, from 0.0012" to 0.0055" on Build 2 and from 0.0017" to 0.0065" on Build 3. The data also shows that both of these features are on side skins on the part. In a similar pattern to the Obi 2 machine, the unsupported upskin to supported down-skin measurements showed to have the lowest variability. Features 6, 10, and 11 all showed some of the lowest average standard devia–tions with Feature 13, a horizontal OD feature, also showing very high repeatability part-to-part.

Table 37. Repeatability Part Height Off of Build Plate (z-axis), Lowest to Highest

SN	Z Location (Height Off of Build Plate, mm)	Height Rank	SN	Z Location (Height Off of Build Plate, mm)	Height Rank
1	10.000	1	11	175.000	14
24	10.000	1	12	190.000	15
2	25.000	2	13	205.000	16
3	40.000	3	14	220.000	17
28	40.000	3	25	231.777	18
4	55.000	4	15	235.000	19
5	70.000	5	16	250.000	20
6	85.000	6	26	263.140	21
7	100.000	7	17	265.000	22
7.5	115.000	8	18	280.000	23
29	120.552	9	19	295.000	24
8	130.000	10	20	310.000	25
9	145.000	11	21	325.000	26
23	146.578	12	22	340.000	27
10	160.000	13	27	340.392	28

All of the builds exhibited very high repeatability, as measured by standard deviation of the recorded measurement deviations. The average for each build was between 0.0012" and 0.0015" indicating a very tight pattern of repeatability across the build plate build-to-build.

3.6.5 Conclusions

Since the part design and wall thickness of the test samples was modified from Phase 1 of testing to Phase II, to induce faster part failure, it is inconclusive if the EBM machine influences the material properties, and thus, the part performance of the test samples. Additional studies are needed to complete a machine-type comparison.

A comparison between the HIP cycle of the Phase II builds can be completed. Looking at the average cycles to failure of each part surface condition, the second batch of parts, with the revised HIP cycle, performed better. In the as-grown condition the improvement is less dramatic. In the as-grown state, failures are often associated with surface condition and not material integrity. The conclusion is much more dramatic for the 0.020" chemical milled samples. The first batch of test parts failed with an average of 150,113 cycles. The second, revised HIP, batch showed no failures even after more than 706,162 cycles. The testing had to be stopped due to project timing, however the results are conclusive showing a more than 4X cycle count improvement by changing the HIP schedule.

To conclude the fatigue study, surface condition of EB-PBF is shown to be a dominant contributor to part fatigue life. In addition, the HIP cycle in which the Ti64, EB-PBF parts are run through also has an impact on overall part fatigue performance. This data will continue to inform the design activities and direction for EB-PBF usage throughout the organization.

As discussed above, the repeatability study conducted shows a very high part-to-part, build-to-build, and machine-to-machine dimensional repeatability relative to the overall expected part tolerances. Additional work is needed to determine steps, including scale factor adjustment, support modifica– tion and part orientation, that can be taken to reduce the average part deviation, which wasn't considered in this study. The size of the part being studied also limits the conclusions. There may be a change in reliability if the part is not near the size of the test geometry (near 3" x 3" x 3").

Overall, this study will give confidence that using the same build file, the EB-PBF process is repeatable across the entire build and between machines.

3.7 Improved Material Properties and Dimensional Accuracy in Binder Jetting

3.7.1 17-4PH Steel in Binder Jetting

In this section, binder jetting work on steels is detailed. 17-4PH steel cylinders were manufactured through binder jet processing, controlling two parameters: (a) binder jet parameters (layer thickness and binder saturation) and (b) the direction of the cylindrical axis with respect to the build orien– tation (X and Z). The two binder jetting conditions selected were – (i) Condition A, where the 17-4PH part was built with 50µm layer thickness and 60% binder saturation, and (ii) Condition B, with 40µm layer thickness and 50% binder saturation. Fabrication took place on an ExOne™ commercial binder jet machine (25Pro). The green part was obtained by depowdering the part from the print bed. Subsequently, the green specimen underwent debinding and sintering in a furnace to achieve its final form. The specimens in the as-sintered condition are hereafter referred to as 'as-received' material. A subset of the as-received specimens was further processed by hot isostatic pressing to reduce/ eliminate isolated porosity, and one set of HIPed specimens (Condition A in the Z orientation) was subjected to the H900 heat treatment specified for 17-4PH steel.

The bakelite-mounted specimens for metallography were polished by mechanical griding on emery paper followed by polishing using diamond suspension. A final vibratory polishing step was performed in 50nm colloidal alumina as polishing media. Optical micrographs were taken in the as-polished condition to ascertain porosity content in the specimens. X-ray diffraction was conducted on selected specimens for evaluating the phases present in the material. Metallographic etching was performed using Kallings reagent (1.5g $CuCl_2$ + 33ml hydrochloric acid + 33ml methanol + 33ml water).

Figure 84 displays the microstructure of the as-received 17-4PH material fabricated using different parameters. Porosity in Condition A specimens (X and Z orientations) ranged between 6.4-7.5%, whereas Condition B specimens exhibited a comparatively lower porosity of 3.4-3.5% in the as-received state. Optical micrographs of etched samples reveal a lath morphology microstructure (what is likely to be Widmansttäten ferrite or perhaps acicular bainite), with a low volume fraction of δ-ferrite at triple junctions (identified by red arrows in Figure 84b. The grain size across all four as-received specimens was consistently observed to be in the range of 40-50µm, indicating that the binder jetting parameters did not exert a substantial influence on the final microstructure.

Figure 85 presents the microstructure of 17-4PH steel processed through HIP. The porosity in the HIPed material varies from 0.5-1.1%, suggesting that HIP serves as a pertinent step in enhancing the densification of binder jet produced 17-4PH samples. Micrographs indicate substantial grain growth
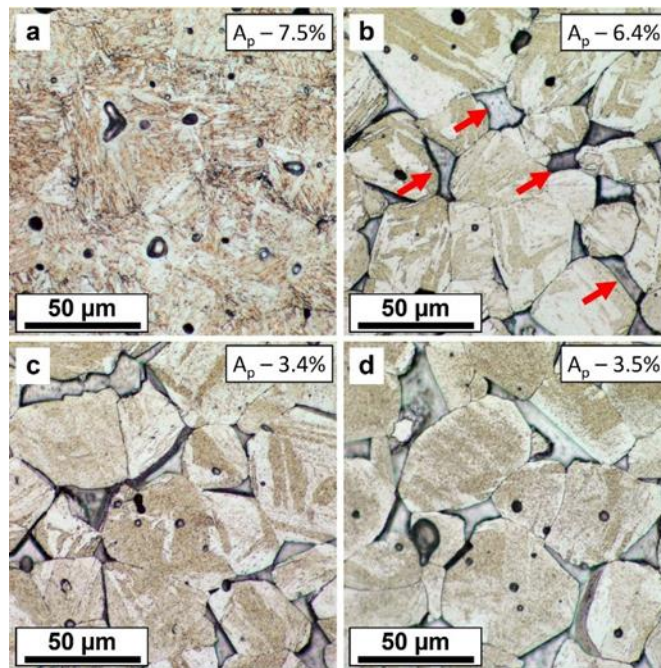
Figure 84.   Optical Micrographs of As-Received 17-4PH Printed
*(a) X and (b) Z Orientations using Condition A Respectively
and (c) X and (d) Z Orientations using Condition B
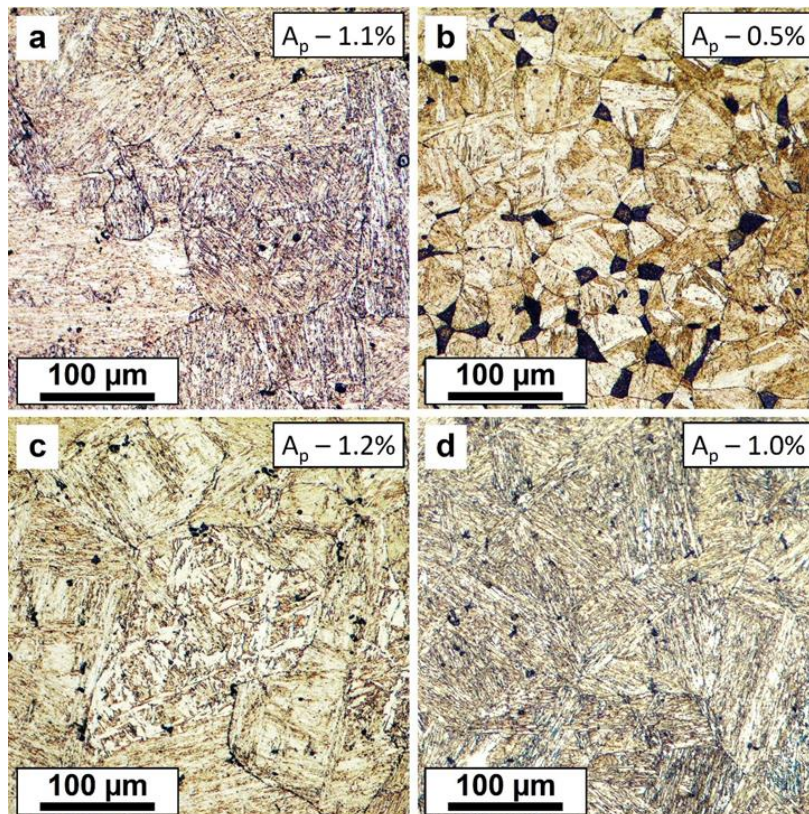A_P denotes the porosity content observed in the specimen*

Figure 85.   Optical Micrographs of As-HIPed 17-4PH Printed
*(a) X and (b) Z Orientations using Condition A Respectively and
(c) X and (d) Z Orientations using Condition B*

during HIP, resulting in a final grain size ranging from 120-180µm. The microstructure remains largely acicular, with a noteworthy reduction in the volume fraction of δ-ferrite after hot isostatic pressing. An exception to this trend is evident in Figure 85b, where the microstructure displays the presence of δ-ferrite and a relatively fine grain structure (~50µm), resembling the characteristics of the as-received material.

Figure 86 shows the microstructure observed in 17-4PH after H900 heat treatment. The microstructure is identified as either martensitic/tempered martensitic and appears similar in morphology to that in the HIPed condition although it is doubtful that the microstructure is martensitic in the HIPed condition (perhaps bainitic).
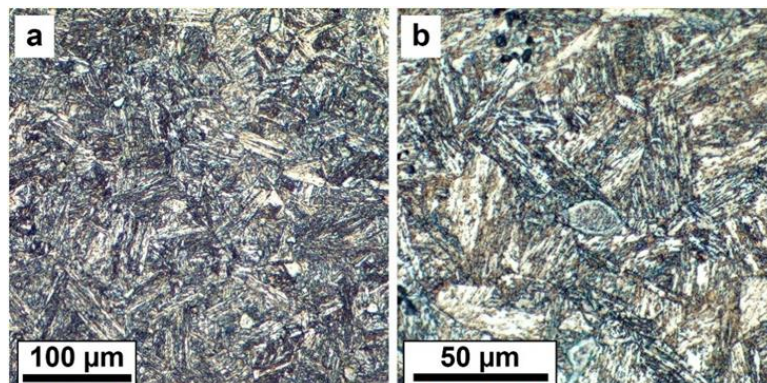

Figure 86. Optical Micrographs of 17-4PH Z Orientation of Condition A in Z Orientation After H900 Heat Treatment

The tensile behavior of binder jet processed 17-4PH steel was evaluated according to ASTM E8 standard (ASTM E8, 2016). Specimens having a round cross-section were machined from the binder jetted steel cylinders. Tensile specimens had gage length of 25.4mm with a diameter of 6mm. Tensile testing was conducted using an INSTRON universal testing machine with a 100 kN load cell capacity with an extensometer attached to the specimen. Specimens were tested in duplicate per condition for ensuring repeatability. Table 38 summarizes the tensile data of the various tested specimens.

Table 38. Summary of Tensile Tests Conducted on Binder Jet Produced 17-4PH Steel

Specimen Name	Binder Jet Condition	Yield strength (MPa)	Ultimate tensile Strength (MPa)	Elongation to failure (%)
X1	A	269	947	2.6
X2	A	259	939	2.7
X1	B	390	1162	3.3
X2	B	373	1155	3.5
Z1	A	374	800	0.9
Z2	A	328	711	0.9
Z1	B	478	1032	2.4
Z2	B	476	1053	1.9
X34-HIP	A	316	1242	4.0
X35-HIP	A	569	1276	6.6
X44-HIP	B	264	1091	5.2
X45-HIP	B	287	1122	5.3
Z26-HIP	A	445	1129	6.1
Z27-HIP	A	347	1174	5.1

Table 38. Summary of Tensile Tests Conducted on Binder Jet Produced 17-4PH Steel (continued)

Z26-HIP	B	209	998	5.2
Z27-HIP	B	201	942	5.3
Z61-H900	A	1046	1307	18.2
Z63-H900	A	1027	1308	17.8

Figure 87 highlights the tensile curves of 17-4PH steel. The tensile data for the as-received and HIPed 17-4PH, as seen in Figure 87a-d, exhibit a distinct kink at the onset of plasticity. Consistent with prior findings on binder jet produced 17-4PH, this observed plateau in stress at the onset of plasticity is indicative of the formation of Lüders bands where unstable retained austenite likely
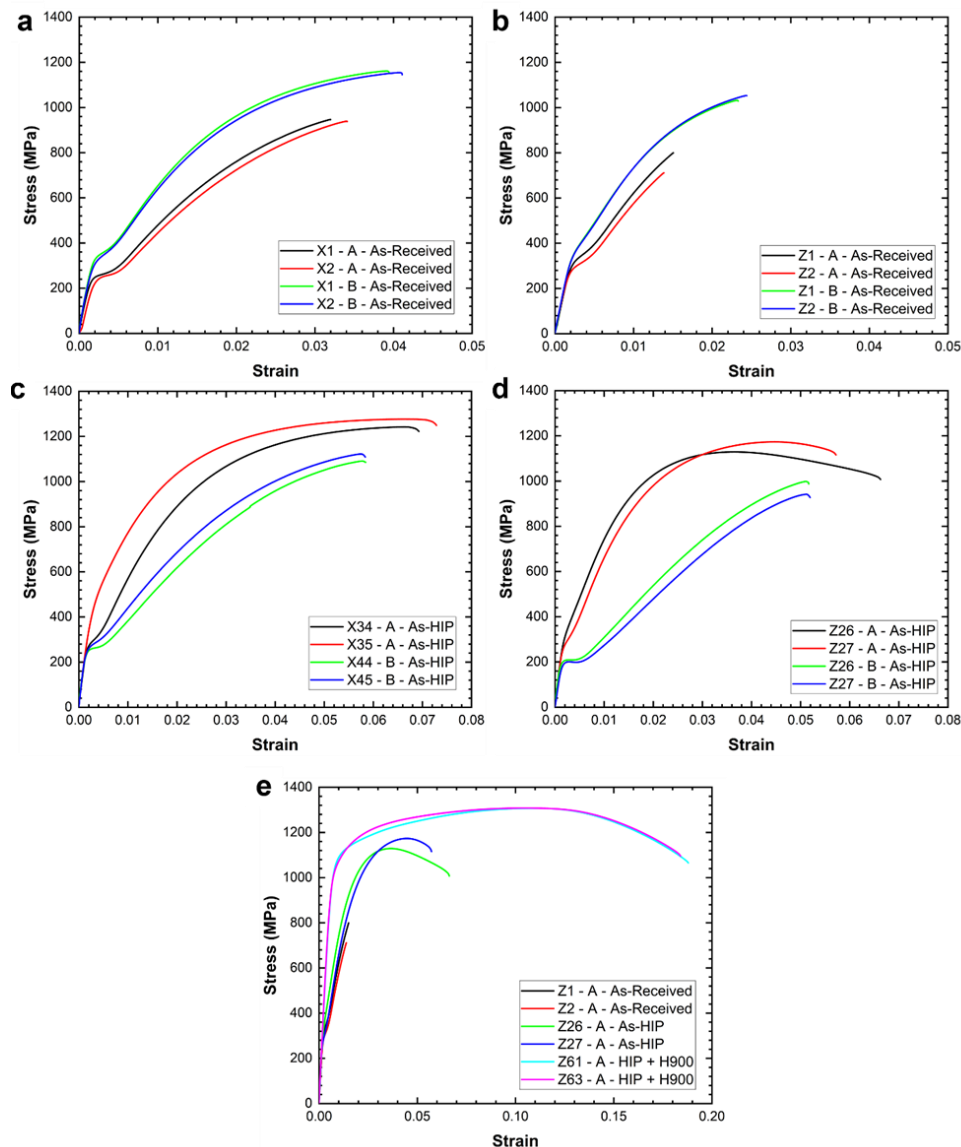
Figure 87. Tensile Curves of Binder Jet Produced 17-4PH
(a) X Oriented Specimens in As-Received Condition, (b) Z Oriented Specimens in the As-Received Condition, (c) X Oriented Specimens in the As-HIPed Condition, (d) Z Oriented Specimens in As-HIPed Condition and (e) Z Oriented Specimens in the H900 Condition Compared to HIPed and As-Received Material

This information, as disclosed to DOD, shall not be modified without the written consent of NCMS.

DISTRIBUTION STATEMENT A. Approved for public release. Distribution is unlimited. OPSEC#9316

101

transforms to martensite during plastic deformation. Considering that the initial 17-4PH powder for binder jet processing was produced through gas atomization using nitrogen gas, it is possible that a certain amount of nitrogen is dissolved in the initial powder which is known to stabilize the austenite phase.

The stress-strain curves for the as-received material (Figure 87a,b) reveal low elongation to failure ranging between 0.9-3.5%. The tensile data distinctly showcase the influence of build orientation and chosen parameters on the tensile response. Table 38 and Figure 87a,b demonstrate that, regardless of build orientation, specimens fabricated using Condition B parameters exhibit higher flow stresses and marginally higher elongation to failure.

The HIPing of binder jet produced 17-4PH did not exhibit a clear influence on flow stresses, although the process did marginally improve ductility to 4.0-6.6%, as evident in Figure 87b,c. This enhancement is associated with a reduction in specimen porosity and an increase in grain size. Figure 87e emphasizes a notable improvement in flow stresses and elongation to failure in Z-oriented specimens built using Condition A. In contrast, H900 specimens displayed an average YS of 1036 MPa and an average elongation to failure of 18%, surpassing specimens tested in the HIPed or as-received condition. Notably, the tensile curves of 17-4PH in the H900 condition do not exhibit a kink at the onset of plasticity after the initial elastic loading. Therefore HIP and heat treatment can be considered indispensable post-processing steps for optimizing the mechanical properties of binder jet produced 17-4PH parts.

The fatigue response of 17-4PH steel was assessed in accordance with the ASTM E466 standard. Specimens, featuring a continuous radius between ends, were machined from the 17-4PH cylinders, with the smallest cross-section having a diameter of 4mm. To mitigate the influence of surface roughness, the specimens underwent polishing to achieve a mirror finish using diamond slurry (9 and 3µm) for the removal of machining marks. Figure 88 shows a typical fatigue test specimen used for the study.

Fatigue testing was carried out in a force-controlled, tension-compression mode (R=-1) on an MTS Bionix universal testing machine equipped with a 25 kN load cell at 20 Hz test frequency. A fatigue test was deemed run-off if the test specimen did not fail within 10 million cycles at the chosen stress amplitude.
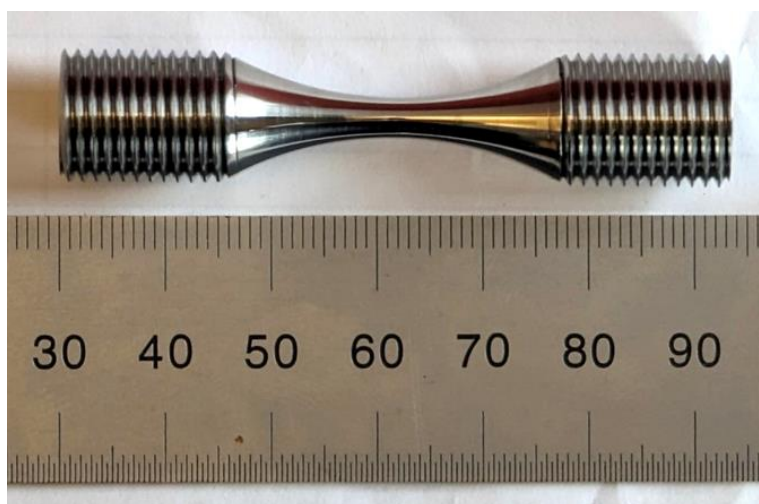

Figure 88.   Fatigue Test Specimen of Binder Jet Produced 17-4PH Steel

Figure 89 presents the S-N curves derived from the fatigue testing of binder jet produced 17-4PH steel. In Figure 89a, the fatigue response of 17-4PH in the as-received condition is compared. Notably, *X* and *Z*-oriented specimens of Condition B exhibited slightly higher endurance stresses of 375-400 MPa, while specimens in Condition A showed endurance stresses of 250-275 MPa. This trend aligns with the observations in the tensile data, where specimens built using Condition B displayed higher flow stresses (Figure 87a,b).

In Figure 89b, the fatigue response of as-HIPed 17-4PH is illustrated. A comparison of the fatigue data in Figure 89a and Figure 89b demonstrates that the HIPed material withstands significantly higher stress amplitudes compared to the as-received material, particularly below 10,000 cycles to failure. The fatigue response of as-HIPed 17-4PH in the *X* orientation (Conditions A and B) closely matches and exhibits an endurance stress of 600 MPa (Figure 89b). This contrasts with 17-4PH specimens in the *Z* orientation, which displays a lower number of cycles to failure at similar stress amplitudes, exhibiting endurance stresses of 300-400 MPa, consistent with the endurance stresses of their as-received counterparts. Figure 89c depicts the fatigue response of *Z*-oriented 17-4PH built using Condition A in the H900 heat-treated condition, compared with its HIPed and as-received
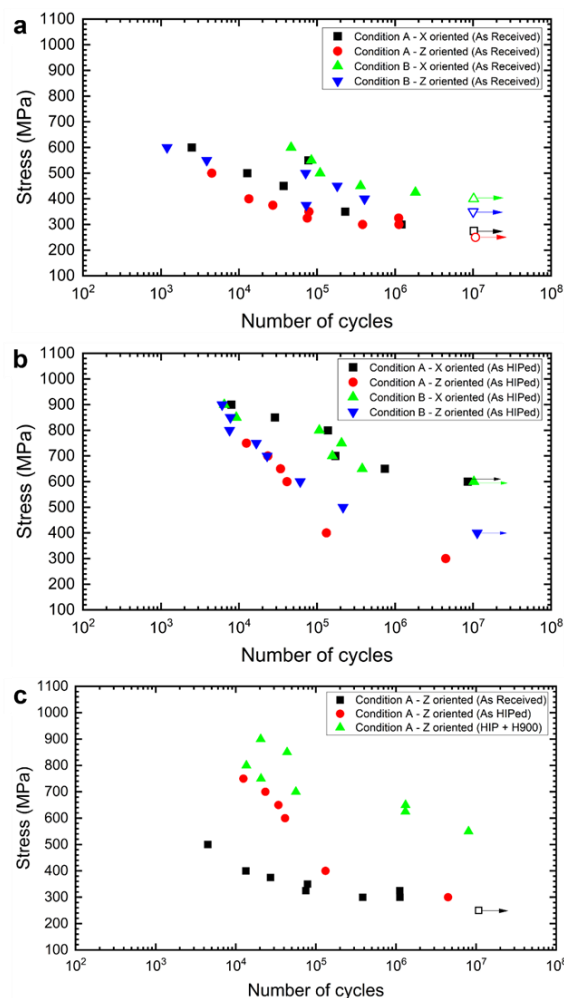

Figure 89.   S-N Curves (R= -1) for 17-4PH Steel
(a) As-Received Condition, (b) As-HIPed
Condition and (e) H900 Condition Compared
to As-Received and As-HIPed Counterparts

counterparts. The H900 heat treatment positively influences the fatigue response of Z-oriented 17-4PH, improving the HCF response with specimens failing at a larger number of cycles to failure for a given stress level compared to the HIPed and the as-received material. The test data indicate that the H900 material exhibited an endurance stress of approximately 600 MPa, double that of HIPed or as-received 17-4PH in the Z orientation. This fatigue test data underscores the significance of HIP and heat treatment for optimizing the fatigue properties of binder jet produced 17-4PH steel.

3.7.2   4340 Steel in Binder Jetting

4340 steel cylinders were fabricated through binder jet processing. The specimens were built in the X orientation with 40µm layer thickness and a binder saturation of 50%. The green part was depowdered from the print bed. Debinding and sintering was subsequently carried out in a furnace to achieve its final form. The sintered specimens were subjected to a final step of HIP; the 4340 material in the as-HIPed condition is hereafter referred to as "as-received" material.

Specimens for metallography were polished by mechanical griding on emery paper followed by polishing using diamond suspension. Optical micrographs of the polished specimens were analyzed to evaluate specimen porosity. The specimen was further etched in 2% nitol for 10 seconds and optical microscopy was conducted to evaluate the microstructure. Figure 90 shows the microstructure of binder jet processed 4340 steel.
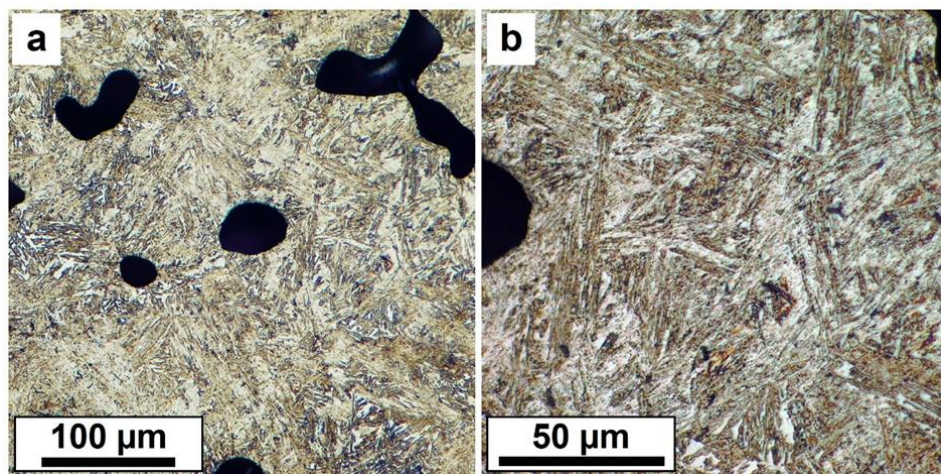

Figure 90.   Optical Micrographs of As-Received 4340 at 20X and 50X Magnifications

The 4340 specimens had a porosity of ~10% implying the presence of interconnected porosity in the specimen prior to HIPing; this would render HIPing ineffective (HIPing works when porosity is isolated and for that typically, the material needs to be more than 94% dense). The 4340 steel exhibited an acicular ferritic microstructure.

The tensile behavior of 4340 steel was assessed following the ASTM E8 standard. Specimens, featuring a round cross-section, were machined from the binder-jetted steel cylinders, with a gage length of 12.5mm and a diameter of 4mm. Tensile tests were conducted on an INSTRON universal testing machine equipped with a 100kN load cell capacity, and an extensometer was attached to the specimen for isolating gage-section elongation measurements. To ensure reproducibility of results, specimens were tested in duplicate. Table 39 provides a summary of the tensile data for the 4340 steel specimens.

Table 39. Summary of Tensile Tests Conducted on Binder Jet Processed 4340 Steel

Specimen Name	Yield strength (MPa)	Ultimate tensile Strength (MPa)	Elongation to failure (%)
B5-12	1005	1355	8.0
B5-19	953	1187	1.3
B5-22	935	1193	2.5

Figure 91 displays the tensile curves of 4340 steel specimens. Notably, the specimens exhibited a YS above 900 MPa. However, it is evident that the three specimens displayed notably different tensile elongation to failure (2.5-8%) which can be attributed to the significant porosity present in the as-received material.
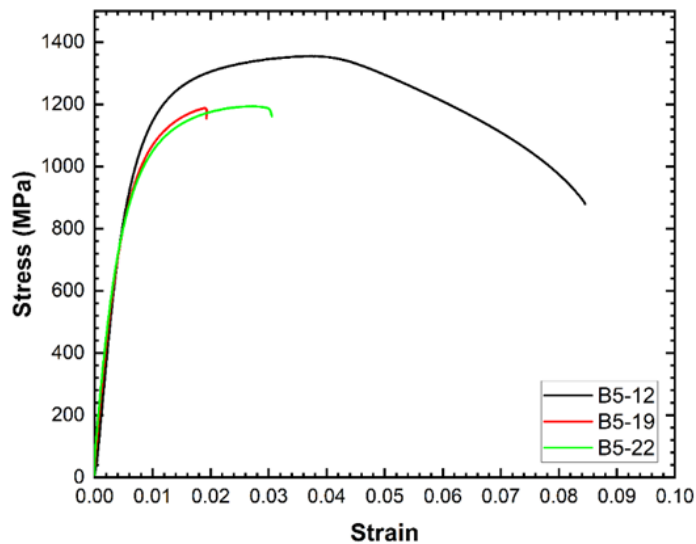

*Figure 91.   Tensile Stress-Strain Curves of Binder Jet Produced 4340 Steel*

Fatigue test specimens, machined from the as-received 4340 cylinders and sharing identical geometry with the 17-4PH fatigue test specimens described previously, were subjected to fatigue testing in force-controlled, tension-compression mode (R=-1) on an MTS Bionix universal testing machine equipped with a 25 kN load cell, operating at a 20 Hz test frequency. A fatigue test was considered run-off if the test specimen did not fail within 10 million cycles at the chosen stress amplitude.

Table 40 provides a summary of the 12 as-received 4340 specimens tested in the tension-compression cyclic loading mode. Out of the 12 specimens tested, six failed abruptly (those identified in red in Table 40). This observed inconsistent behavior can again be attributed to the significant porosity present in the 4340 HIPed specimens.

Figure 92 shows the S-N curve generated from the fatigue testing of binder jet produced 4340 steel specimens (those identified in red in Table 40 were not included in Figure 92). The data shows the binder jet produced 4340 has an endurance limit of 550 MPa (which is $0.57\sigma_y$).

Table 40. Summary of Fatigue Tests Conducted on Binder Jet Produced 4340 Steel

Specimen Name	Stress Amplitude (MPa)	Cycles to failure
B5-25	850	142
B5-10	800	163
B5-14	800	30687
B5-15	750	44603
B5-28	700	302
B5-30	700	1384
B5-3	700	93796
B5-29	675	298
B5-26	675	425
B5-17	650	1080797
B5-13	600	2815265
B5-18	550	8720512
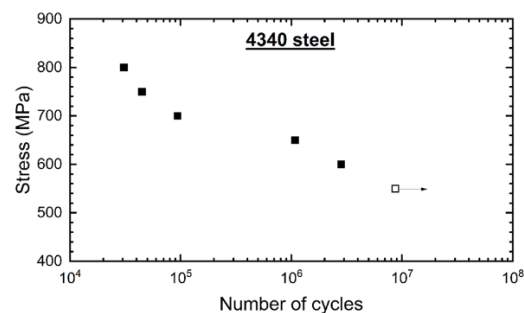
Figure 92. S-N Curve of 4340 Steel for R= -1

3.7.3 Dimensional Accuracy in Binder Jetting

In assessing the dimensional accuracy of the fabrication process of the 17-4 rotor component, initial dimensional evaluation of the accessory gearbox dynamic seal rotor was performed using 3D scanning technology (Figure 93). The nominal CAD geometry was set as a baseline. The colors on the part represent departure from nominal to the magnitude described in the legend. The observed tolerance range was approximately ± 0.25mm [± 0.010"]. This tolerance band is too large for critical surfaces like the inner diameter and seal face, but those two surfaces are to be machined regardless of dimensional quality in order to achieve the target sealing performance. The remaining geometry is acceptable as is at those tolerance ranges.
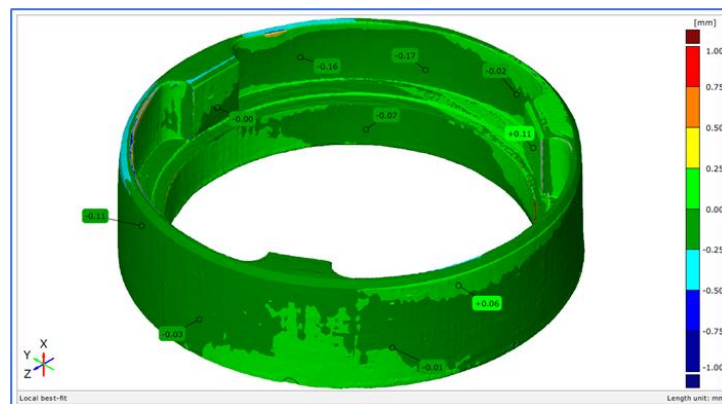
Figure 93. Accessory Gearbox Dynamic Seal Rotor, Dimensional Scan

The main-shaft dynamic seal rotor was inspected by the vendor using hard gauging. Vernier calipers and drop dial indicators were used to determine variance to the nominal geometry. Table 41 details the results.

Table 41. Dimensional Characteristics of Main-Shaft Dynamic Seal Rotor

No	Zone	Major/ Minor		Characteristics	*Checking Method	**Instrument /Gauge No.	AQL	Actual	
								Min	Max
I. Functional/Dimensional (in)									
1	B2	---	Diameter	62.87	Vernier caliper	IMSA-CAL-005		62.740	62.900
2	B2	---	Diameter	54.74	Vernier caliper	IMSA-CAL-005		54.200	54.500
3	B1	---	Diameter	47.37	Vernier caliper	IMSA-CAL-005		46.970	47.380
4	B1	---	Diameter	45.02	Vernier caliper	IMSA-CAL-005		45.690	44.890
5	B1	---	Diameter	60.7	Vernier caliper	IMSA-CAL-005	4.0	60.490	60.760
6	A1	---	Thickness	6.35	Vernier caliper	IMSA-CAL-005		6.180	6.420
7	B1	---	Depth	1.14	Vernier caliper	IMSA-CAL-005		1.080	1.201
8	B1	---	Depth	2.24	Drop dial indicator	--		2.183	2.347
9	B1	---	Depth	4.65	Drop dial indicator	--		4.512	4.743

As with the accessory gearbox rotor, the inner diameter and sealing face are critical and therefore post machined regardless of dimensional accuracy from printing. While thickness for this main-shaft rotor had a high level of variation circumferentially around the part, a grinding process provided even parallel surfaces front to back, followed by an ID turn to provide perpendicularity.

3.8 AM Binder Jetting Steel Component

3.8.1 Accessory Gearbox Rotor

Building off progress made in AMoCC Phase I, a third iteration Accessory Gearbox (AGB) rotor was designed and produced with the intention of running dynamic sealing testing to determine functional performance capability. Existing testing had been completed on the selected platform such that direct comparisons could be made with the binder jetted rotor.

Beginning with production of the rotor, Indo-MIM (a vendor out of San Antonio, TX), operating Desktop Metal P1 systems, produced a quantity of 10 AGB MVP3 rotors of the design explored in Phase I. A section of the design is shown in Figure 94 for reference. Of note, the design is in two pieces to facilitate depowdering. During the manufacture process, initial builds failed due to channel sizes being too small to depowder. Indo-MIM requested the channels be increased in size by ~15% to remove powder more easily prior to sintering with risk of damage to parts. However, prior to producing those redesign parts, Indo-MIM was able to successfully depowder the original channel sizes using a combination of compressed air and simple pipe cleaners as a mechanical

Figure 94.   AGB Rotor After Welding, Prior to Machining

depowdering means. This process is by no means efficient or effective when scaled up to production volumes but was suitable for experimentation.

Welding of the two components was performed by Eaton's East Providence facility. A Gas Tungsten Arc Weld (GTAW) process was used, with low power, to fuse the components together without melting through the part. Filler material was not used. This process is commonly used by Eaton in the production of metal bellows seals.

After welding, the parts were turned to size on the ID such that they would fit onto the shaft adapter on the test rig. The face was then turned to be perpendicular to the ID within 0.001". Finally, the face was ground to prepare for lapping

A hard-face coating (tungsten carbide) was meant to be applied to the rotor face, but time constraints and a vendor inflexibility led to delays that forced the team to test without the hard face coating. As such, the rotor was prepared further for test by installing the final features. The face was lapped flat to within three helium light bands (0.000033") of flatness. Hydrodynamic lift pads were added to the face using the same geometry developed for the current non-AM product. This enabled the team to compare results with AM features and material being the only differences. The final manufacturing step was the addition of holes at the beginning of the hydrodynamic pads to supply pressurized air from inside the part. From Phase I, the air is "pumped" into the part through a pair of nested helical channels that perform work to the air as the part rotates. With this final feature installed, it was ready for test (Figure 95).

Figure 95.   AM Mating Ring with Hydrodynamic Pads and Holes in Face

Start/stop cyclical testing on the rotor to characterize heat generation with speed, and determination of hydrodynamic lift-off and touch-down speeds was conducted. Testing was performed in Eaton East Providence in the dynamic seal test lab. The test rig used (shown in Figure 96) was the "Alpha Rig" which features an electric spindle driven by a Variable Frequency Drive (VFD). Rig control and data acquisition was performed with LabVIEW. Pressure transducers and thermocouples measure cavity pressures and temperatures during operation. Oil was delivered to the seal using an oil sump for delivery and recovery. The casing featured oil drain ports for collection of any leakage past the seal, its primary function. The carbon element was instrumented with thermocouples to measure temperature during operation.
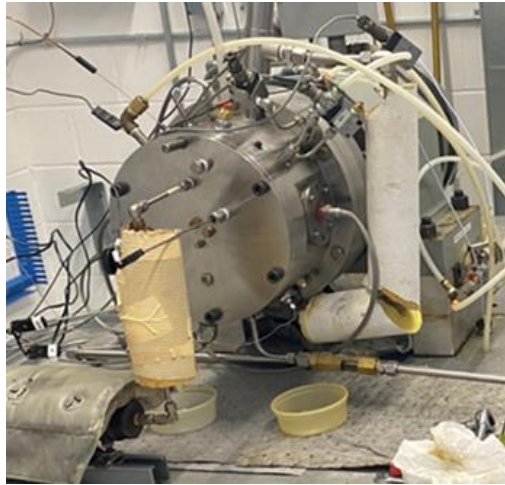
Figure 96.   Test Rig Used for AGB Rotor Testing

Testing demonstrated temperature at the sealing interface approximately 50-75°F higher than the baseline contacting and hydrodynamic tests. The hydrodynamic lift characteristics were inconsistent, with temperature fluctuating at steady state speed and pressure. This is indicative of a hydrodynamic film that is challenged by some condition. Oil leakage measurements were within expectations for a properly functioning seal.

Temperatures while running were lower than the oil coking limits, they were still higher than expected. The cause for these elevated temperatures is likely due to the lack of a hard face coating on the rotor. Hardness of the 17-4PH material was measured to be 35 HRc. A hard face coating would exceed 60 HRc and is more desirable for a dynamic seal tribological pairing. Additionally, post-test inspections highlighted wear on the rotor that directly impacted the hydrodynamic pads, in some cases removing them entirely. Test results are shown in Figure 97.

3.8.2 Main-Shaft Rotor

The main-shaft rotor build boasted easier depowdering and lower levels of post-printing work to achieve a final product. A larger envelope enabled larger through holes that did not necessitate a two-piece design to facilitate depowdering. Additionally, analysis uncovered a performance improvement by running individual channels from inlet to outlet, as opposed to running inlet channels to a common annulus as was done in the AGB rotor. The main-shaft rotor features a series of 16 inlets feeding 16 channels exiting out of the primary sealing face in 16 locations (Figure 98 and Figure 99).
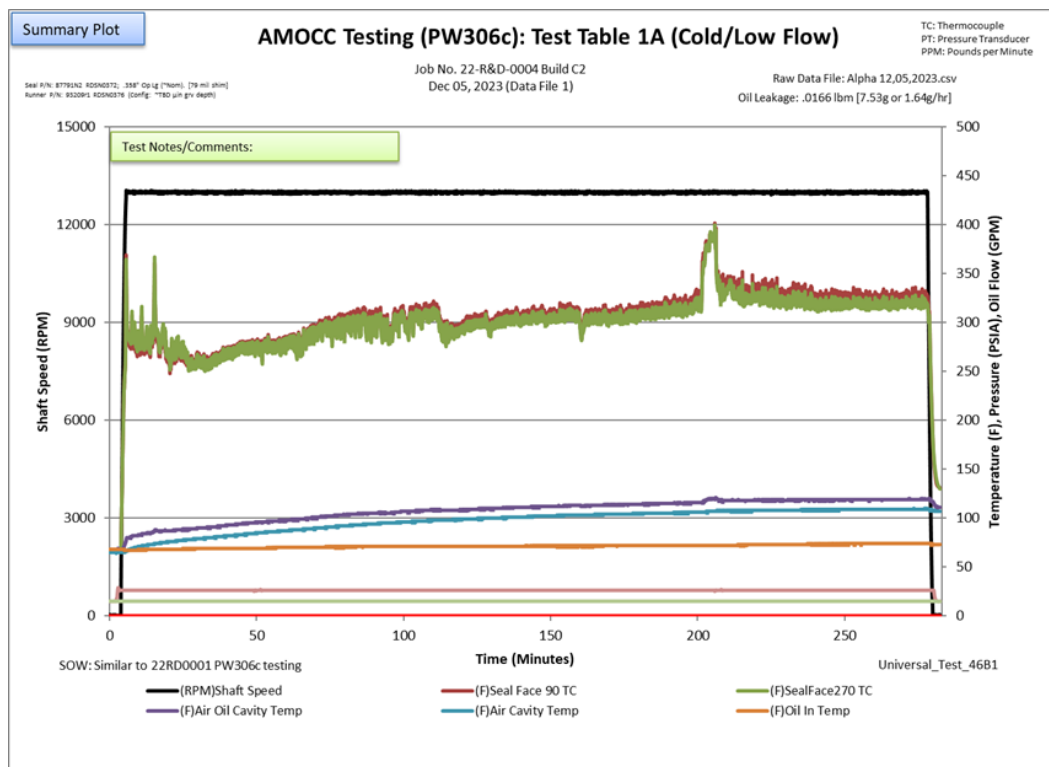
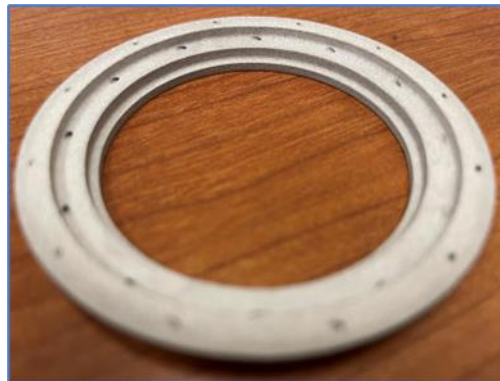*Figure 97. Test Results of MVP3 AGB Rotor*

Figure 98. Main-Shaft Rotor Prior to Machining, As Built (Post-Sinter)
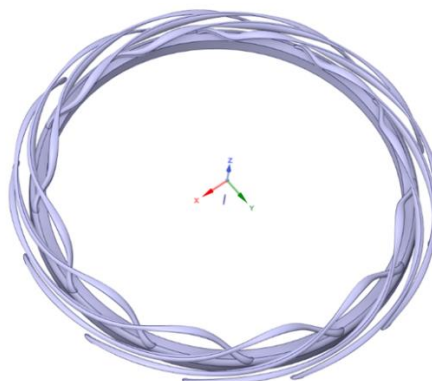

Figure 99. CAD of Internal Channels of Main-Shaft Rotor

Hardware built was turned on the ID for fit with a shaft, and the face was ground flat, then lapped. The intent was to test in this condition with the bare 17-4PH material as was done with the AGB rotor. However, due to learnings from AGB testing where it was found that the 17-4PH material was insufficient to prevent accelerated rotor wear, it was decided to not test until a coating was applied. The test rig adaptive hardware was completed, the carbon seal was instrumented, and all pre-test inspections were completed. The last step is to prepare the rotor for test by coating, lapping, and installing hydrodynamic features. Additionally, AGB rotor testing will continue once a hard face coating is applied in the same manner.

3.9 In-Situ Defect Detection

3.9.1 Introduction

This section summarizes the efforts conducted to survey and study a suite of in-situ monitoring solutions utilized in metal powder bed fusion processes as part of Phase II of the AMoCC project. This study aimed to both (1) conduct thorough research of industry-available in-situ monitoring and in-house developed supplementary software solutions for powder bed fusion processes and (2) perform an initial capability assessment of several down-selected packages using equipment available at the Charleston DDAMC. All software developed by Eaton that has been described in this section was done so as a previous and separate effort.

The packages chosen for capability analysis in this project were selected based on price, availability (timing), ability to implement without altering or affecting machine-original equipment manufacturer (OEM) hardware. All capability assessments are preliminary, with intent to provide a quantifiable understanding performance; all conclusions and derived models are subject to further substantiation necessary for practical implementation. In-situ software was chosen based on applicability to metal powder bed fusion processes; those solutions which apply to alternative AM processes were not considered for analysis herein.

3.9.2 Equipment Used

All software/hardware capability assessments were performed on two machines located at the Charleston DDAMC. See details for utilized equipment below.

The EOS M400-4 platform is an L-PBF platform that utilizes four lasers for simultaneous melting with a unique, centrally located gas flow inlet that allows enhanced flexibility of laser utilization. Platform size and quadrant identification is illustrated in Figure 100. All material produced on the M400-4 platform for purposes of this study was AlSi10Mg

The Arcam Spectra L leverages an electron beam as its energy source for powder fusion, operating in a vacuum-chamber environment, inert with a small volume of pure Helium. This platform (Figure 101) uses a cylindrical build volume, with all regions accessed by a single energy source. All material produced on the Spectra L platform in this study was Ti-6Al-4V.
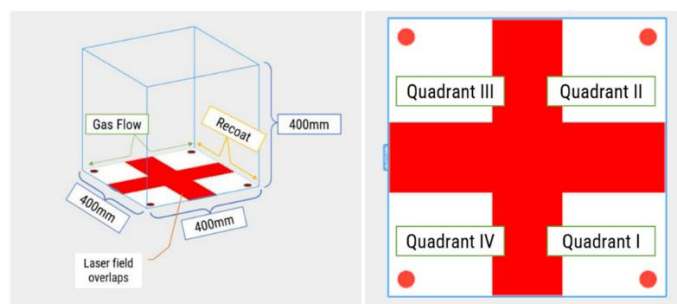
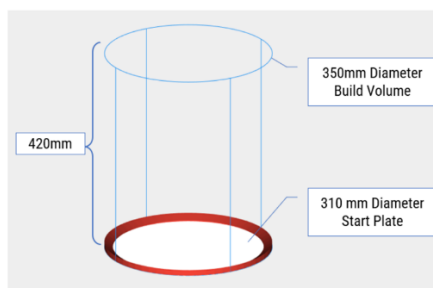**Figure 100.   M-400 Platform Definition**

Figure 101.   Spectra L Platform Definition

3.9.3   Industry Evaluation

The Eaton team conducted a thorough search of commercially available, privately licensed, and internally developed in-situ software solutions available for metal powder bed fusion processes. Table 42 details a comparison matrix of readily available solutions considered for the subject study. Software down-selection was done by prioritizing those solutions which involved no machine modifications. Table 42 aims to summarize those solutions which were potentially available to the Charleston DDAMC team for detail analysis and capability scoring. From initial industry evaluation, the software solutions listed below were targeted based on immediate applicability to the DDAMC production efforts.

Table 42.   Industry Evaluation of In-Situ Solutions

Software	Developer	Platform	Purchase Mechanism	Selected for Study	Summary
EOState Exposure OT	EOS	EOS	License	Yes	Real-time photodiode-based IR image generation for EOS platforms
EOState Powder Bed	EOS	EOS	License	Yes	In-process CMOS camera images captured at pre-defined points in layer wise process
EOState Melt Pool	EOS	EOS	License	No (cost)	Real-time melt pool data generation utilizing laser diodes for monitoring of emitted heat and melt pool shape
LayerQam Report	Arcam	Arcam	Free with Machine	Yes	Provides approximated, relative density information for parts produced by analyzing IR images after completion of each build
Powder Bed Analysis Tool	Carnegie Melon	Agnostic	License	Yes	Utilizes a pre-trained CNN to perform autonomous defect detection in powder bed images
Jimi	Eaton	Arcam	License	Yes	Generates a pseudo-CT scan by creating 3D models from in-situ IR images
Thermal Model Generator	Eaton	Agnostic	License	Yes	Creates a color-coded 3D model based on thermal profile identified in IR imaging
Powder Bed Image Heatmap Generator	Eaton	Agnostic	License	Yes	Generates a heatmap analysis report utilizing in-situ powder bed images for fixed process control
3D Heatmap Generator	Eaton	Agnostic	License	Yes	Creates a 3D space with color-coded models based on any user-defined variable to understand spatial variation
PrintRite3D Suite	Sigma Labs	Agnostic	Purchase / License	No (machine-invasive)	Utilizes external sensing equipment (added to machine) to perform real-time machine and part health analysis and provide closed-loop process control

3.9.4 Software Implementation

Table 43 lists the software solutions subjected to capability analysis herein; all software packages listed below are available and in regular use at the Charleston DDAMC for manufacturing of aerospace components.

Table 43. Targeted In-Situ Software Solutions

Software	Developer	Platform-Specific?	Targeted Technology
EOState Powder Bed	EOS	Yes	L-PBF
Powder Bed Analysis Tool	Carnegie Melon	No	L-PBF
EOState Exposure OT	EOS	Yes	L-PBF
LayerQam Report	Arcam	Yes	EB-PBF
Jimi	Eaton	Yes	EB-PBF
Powder Bed Image Heatmap Generator	Eaton	No	L-PBF
3D Heatmap Generator	Eaton	No	L-PBF
Thermal Model Generator	Eaton	No	L-PBF

Eaton's Charleston-based DDAMC EOS M400-4 machine is equipped with a Complementary Metal Oxide Semiconductor (CMOS) camera which was utilized (by default) to capture two grayscale images on each layer, within the visible light spectrum; after completion of recoat and after com–pletion of part exposure (Figure 102). These images, on their own, provide a useful history of the build process and comprise the standard EOSTATE Powder Bed in-situ monitoring framework. When used with ancillary image processing tools this can provide insight into build health. This benefit is most-immediately realized when comparing build-to-build image analysis results in a locked production scenario.

Figure 102. EOSTATE Powder Bed Images

During early industry evaluations of commercially available in-situ solutions, the Charleston DDAMC procured via license a MATLAB-based Artificial Intelligence (AI) algorithm, which utilizes a trained Computed Neural Network to flag common anomalies identified from a build by analyzing layer-wise build images from the manufacturing process. This tool developed by Carnegie Mellon University, henceforth referred to as Powder Bed Analysis (PBA) tool, utilizes images captured both after exposure and after recoating. After insourcing the algorithm for the backend modeling, the Eaton Aero AM team developed a single-point user interface for the application and performed various training activities to enable the tool's functionality with the Charleston DDAMC M400-4, for processing AlSi10Mg on a 70-micron standard layer. In addition to providing a user interface for software interaction, the Eaton-developed modifications automate the five backend processing steps, which would otherwise require manual intervention.

The PBA output provides insight to various anomaly types, defined in Table 44. An example output image from the PBA tool is shown in Figure 103.

Table 44. PBA Anomaly Classifications

|	
Recoater Hopping	Excessive contact between part and recoater, or damage to recoater drive hardware can lead to invariable powder thickness due to movement of the recoater orthogonal to the build plane (up and down). This typically appears like waves or ripples in the powder bed, often called "hopping" or "skipping".
Recoater Streaking	Occurs when recoater spreading mechanism (blade or otherwise) sustains damage that creates a high point along the length of the device. The high point leaves a line of elevated powder on subsequent layers, parallel to the path of the recoater.
Debris	Material identified that is neither feedstock (powder) or part (solid). In most cases, debris is soot by-product that was not sufficiently removed from cover gas flow. In few instances, debris can be pieces of part or recoater material that have separated due to excessive contact.
Super-Elevation	Parts that are poorly anchored to material below will lift above the powder bed due to thermomechanical responses (inherent stress). Can be the result of poor support strategy or lack-of-fusion between layers.
Part Damage	Occurs when a recoater (typically a "hard" recoater) contacts a part to the point of altering its geometry and potentially removing material from the part and recoater.
Incomplete Spreading	Occurs when powder dosing is insufficient to cover entire powder bed. Can be the result of poor powder flow or insufficient powder is provided by dosing mechanism due to high 2D melt volume.
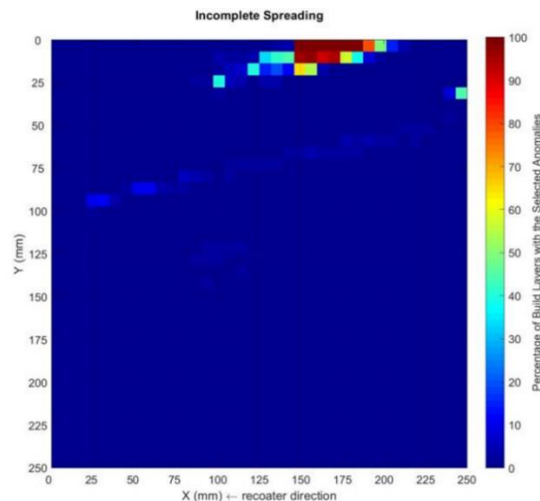
Figure 103. Example of Incomplete Spreading Heatmap Output from PBA Tool

The Charleston DDAMC EOS M400-4 machine was installed and additionally configured with the ExposureOT hardware/software package. This software package is provided by EOS as a standard add-on, with hardware built-in to all newly delivered equipment. The tool utilizes on Optical Tomography to report thermal response data from each unique part/build file. Optical tomography (OT) is an image-based measurement technique. The EOS-offered solution for OT utilizes an CMOS camera, mounted at the top of the build chamber, to capture thermal emissions from the entire build plate throughout the entire layer-wise process by recording emitted light in the near-infrared range. Included with the standard install, is a client-side software used to display and export generated images and data. At the end of each layer, color-scale image is generated to depict the maximum, instantaneous thermal emission observed at each discrete pixel location for the duration of the image (Figure 104). This image is useful for understanding factors that influence laser energy input.

Additionally, a secondary color-scale image is generated which depicts the resultant integral of the observed thermal emission vs time over the duration of the layer (Figure 105). By recording the integral of the heat profile rather than maximum point, effects of conductivity to lower layers are inherently captured as well. This image is useful for identifying differences from repeated builds/geometries, and layer-wise defects.
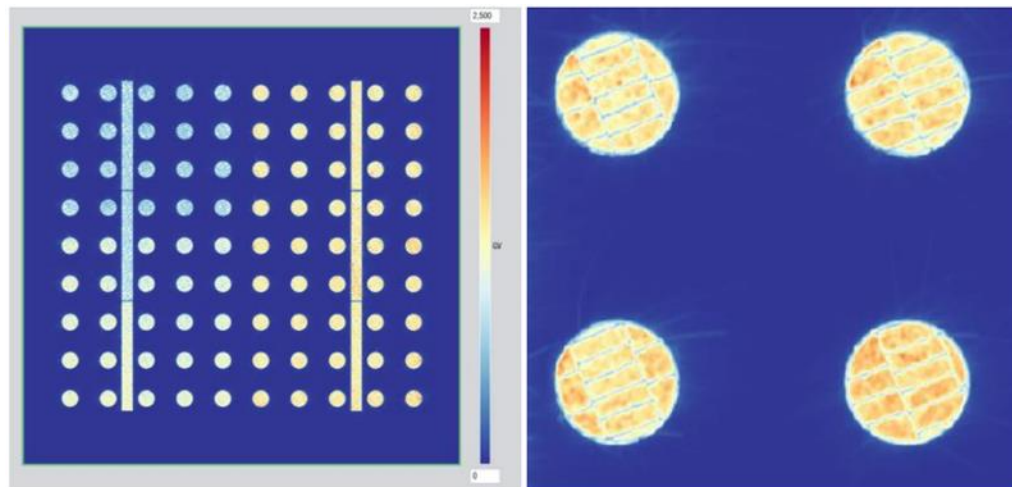

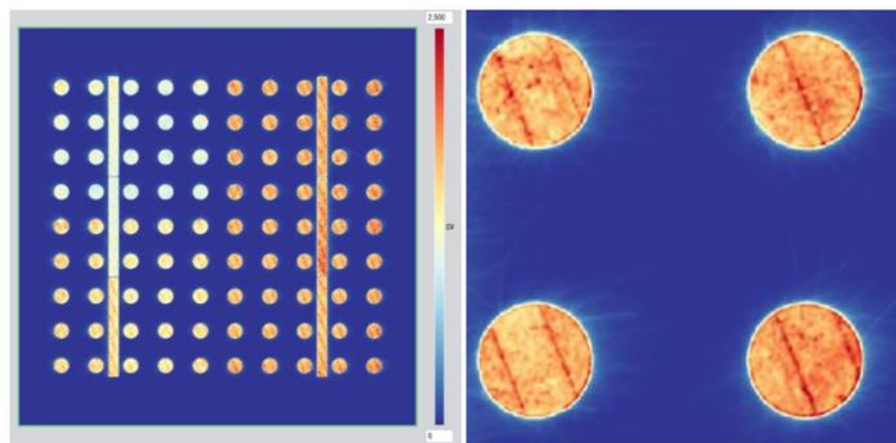*Figure 104.   Example of Max GV Image Output*

Figure 105.   Example of Integral GV Image Output

The Charleston DDAMC Arcam Spectra L EBM printer comes equipped with a camera mounted at the top of the chamber, outside of a viewport. This Arcam LayerQam camera operates at the near-infrared (IR) frequency and, by default, is utilized to capture a single, grayscale image at the end of every melted layer (Figure 106). This camera is controlled by the printer itself and, under standard install, captures images using an auto-exposure feature, wherein many images are taken for approximated exposure time analysis and one final image is captured based on analysis of the prior images to ensure each layer produces legible thermal images. Because the EBM process operates at elevated temperature (approximately 800°C) the thermal images provide unique insight about part quality compared to image data captured in L-PBF. Beyond the thermal history of the components built, IR imaging also reveals localized conductivity minimums in the material (i.e., "bright-spots") which are indicators of porosity, lack-of-fusion, or other in-build anomalies.
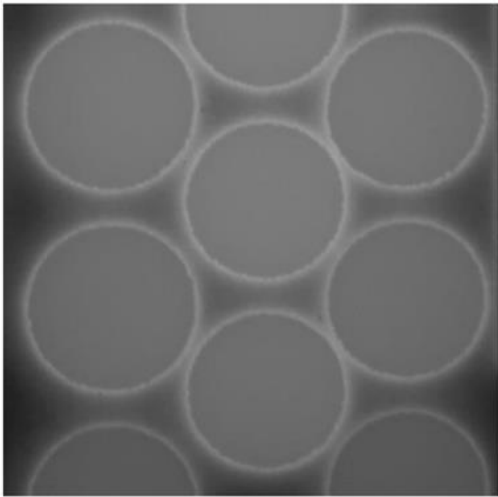

Figure 106.   Example of LayerQam Output Image

As part of the standard software package with purchase of the Spectra L machine, Arcam offers their own "LayerQam Report" (formerly known as "Defect Detector"). A report is automatically generated upon completion of each successful build, utilizing the build's LayerQam images. The LayerQam Analysis software analyzes each part in each generated IR image – using bright spots as assumed areas of low density – to create a graphical representation of density per layer, reported as a percentage (ratio of bright spots to "normal" pixels), with mean and standard deviation values reported for each part (Figure 107). Additionally, the report details the overall build density mean and standard deviation values based on all parts.
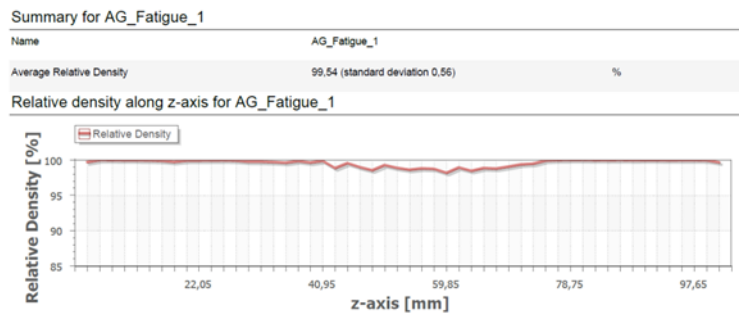

Figure 107.   Example of Arcam Part Analysis Graph and Summary Information

This Charleston DDAMC-developed Jimi software utilizes the standard LayerQam images generated by the Spectra L EBM machine to perform analysis in real-time during machine run to provide qualitative and quantitative insights to machine and build health. This software is considered supplementary to OEM-provided in-situ tools. The tool utilizes various image analysis techniques and a proprietary combination algorithm to detect perceived defects and anomalies throughout the build process and display them as a 3D model, with various graphical and 2D image outputs to support analysis (Figure 108).
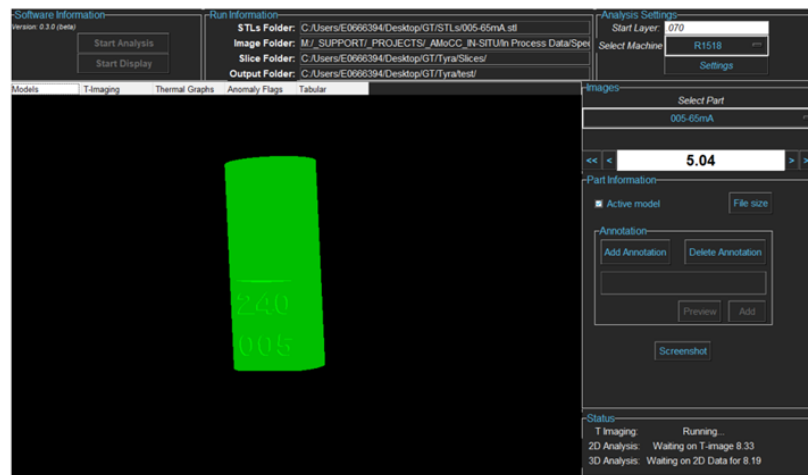
Figure 108.   Jimi User Interface

The Jimi software can operate post-build or in parallel to the building process to provide key quality information and process deviation alerts with <1 min lag from the real-time process. The first panel of the software features the real-time in-situ model generation, which identifies anomalies in the LayerQam images and creates a model for each unique anomaly in 3D space, emulating the results of a CT scan report (Figure 109). This model updates at a regular cadence to show build progress and in-process model results. Users can also add annotations to active model display and capture quick screenshots through the software to include in final quality report (Figure 110).

The fourth tab displays a uniquely selected part image on any specified layer, with image overlays to show what defects were identified by the algorithm. These 2D images are useful as a cross-sectional analysis – similar to CT analysis – as well as for troubleshooting build errors and analysis settings (Figure 111).
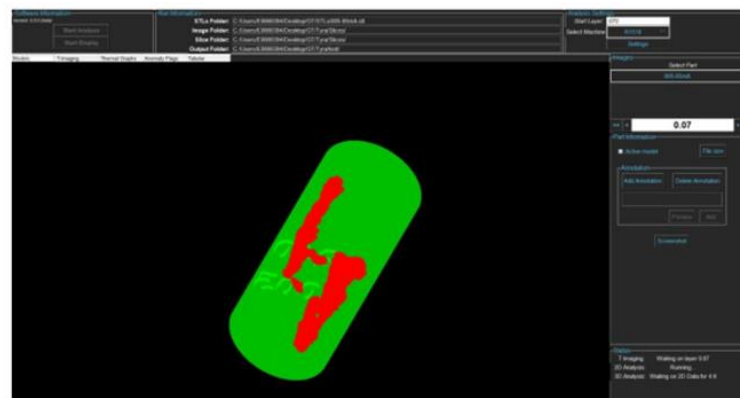

Figure 109.   Jimi In-Situ Anomaly Model Generation

Figure 110.   Jimi Example of Model Display Annotations
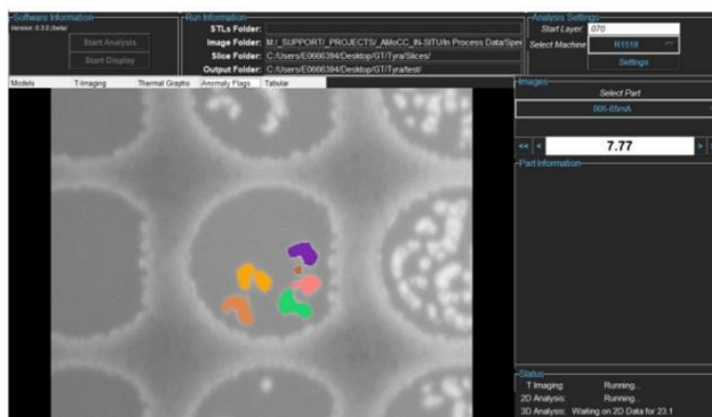

Figure 111.   Jimi Image Analysis Cross-Sections

The Charleston DDAMC-developed "Powder bed Heatmap Tool" is an additional analysis tool that summarizes all user-provided powder bed images with a graphical and heatmap output for both average image intensity and standard deviation by location (image segments – Figure 112). These heatmaps and image intensity graphs are useful for providing expedited insight to areas of concern in a new build file; they are also viable for build-to-build comparisons in a production setting for capturing process deviations between runs.
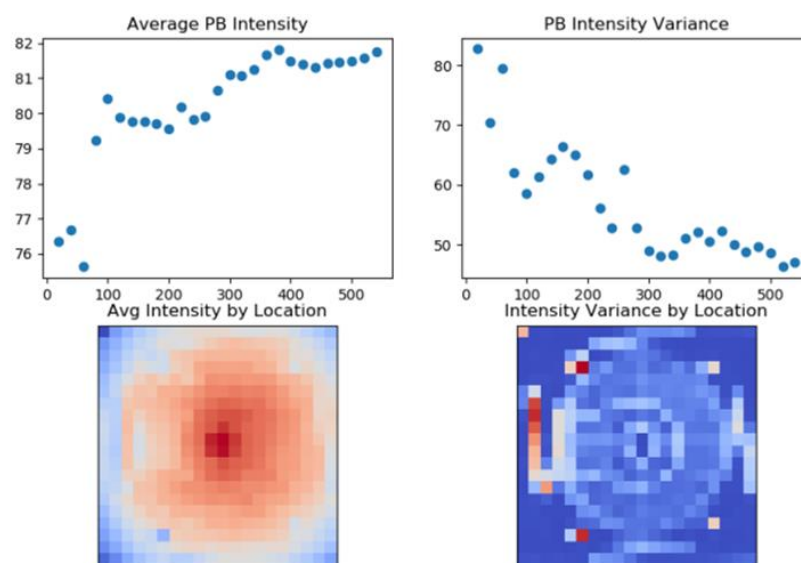

Figure 112.   Example of Heatmap Generation Output

The Charleston DDAMC-developed "3D Heatmap Generation Tool" is an analysis tool that can take any set of data coupled with a 3D model with assigned build location coordinates (X, Y, Z) and create a color-coordinated 3D graphical display that can be manipulated by the user. This tool is useful for comparing the results of in-situ data, static material properties, surface roughness, and other metrics in 3D space with respect to each part's original location on the build plate for expedited analysis and troubleshooting. The tool can be used to visualize machine biases and tendencies based on build height, location with respect to inlet gas flow/recoater, and distance from laser center (Figure 113).

The Charleston DDAMC-developed Thermal Image Model Generator software is designed to take an input of printed CAD and thermal images (via OT Exposure, IR camera, or other hardware) to produce a replicate model of the built component that is color-coded based on a user-defined voxel size to quickly and intuitively display 3D normalized temperature profile data for the subject part. This visualization of perceived thermal response is utilized for error/anomaly troubleshooting, feedback to distortion correction, support material decisions, and correlative analysis. An example of the tool's output is shown below in Figure 114.
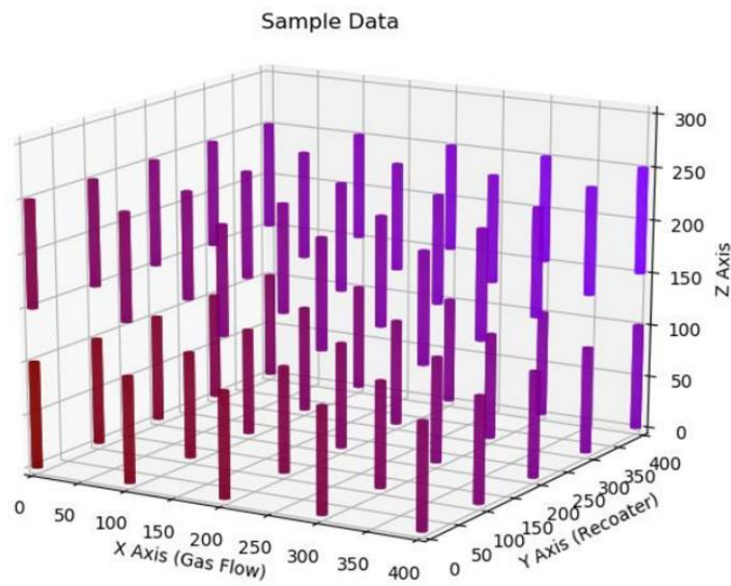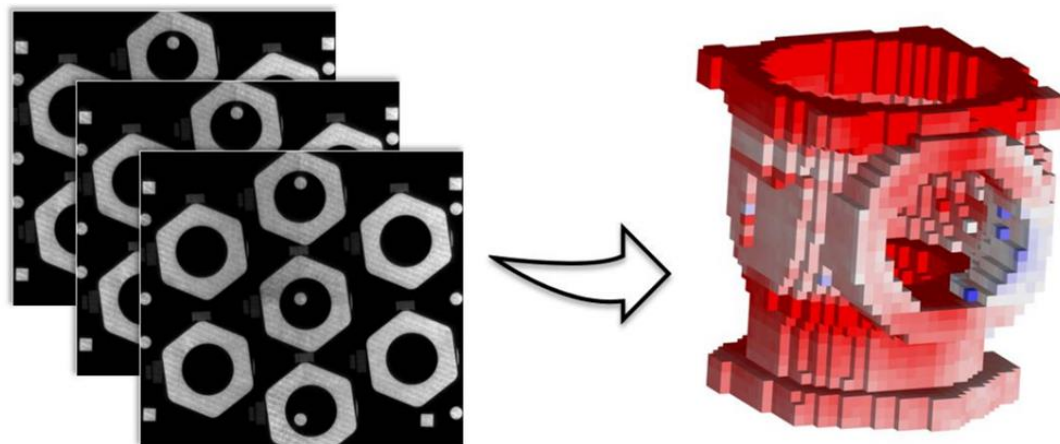

Figure 113.   Example of 3D Heatmap Generation Output

Figure 114.   Example of Thermal Image Model Generator Output

3.10   Model for Critical Flaw Size in AM Alloys

The VHCF behavior of an AM Ti-6Al-4V alloy processed by EBM and wire arc melting (SCIACKY) routes was studied to understand the role of microstructural length scale on the crack growth behavior of AM Ti alloys with fully lamellar microstructures. USF testing at the stress ratio of $R= -1$ was applied to monitor the growth of small cracks initiated from an artificially made defect on the surface of the specimens. The interaction of cracks with the lamellar microstructures was characterized by Electron Back Scatter Diffraction (EBSD) observations. The fatigue fracture surfaces of both samples were also characterized by SEM.

Figure 115 illustrates the SEM images of microstructures of the AM Ti-6Al-4V alloy processed via EBM and SCIACKY in both the building (Z) and perpendicular to the building (X) directions. The microstructures mostly consist of large grains, beta grains formed upon solidification. The fully lamellar microstructure of the alloy fabricated by the EBM route consists of finer grain size and coarser a laths with a smaller aspect ratio compared to the alloy produced by the SCIACKY method. The measured thickness of a lamella was about 1mm and 2.5mm for the samples produced by SCIACKY and EBM techniques, respectively. The length scales of microstructure are anisotropic with comparable lath length along the X and Z directions. The EBSD maps of the X and Z cross-sections for the SCIACKY and EBM samples are shown in Figure 116. The SCIACKY sample confirmed the presence of very large grains at the order of several hundred microns which are more elongated in the Z direction and more equiaxed in the X direction (Figure 116a-b). Figure 116c-d shows a finer grain structure at the order of 100mm for the EBM sample. Figure 116c, shows both needle-like and equiaxed a colonies larger than 50mm in the X direction. Figure 116d demonstrates
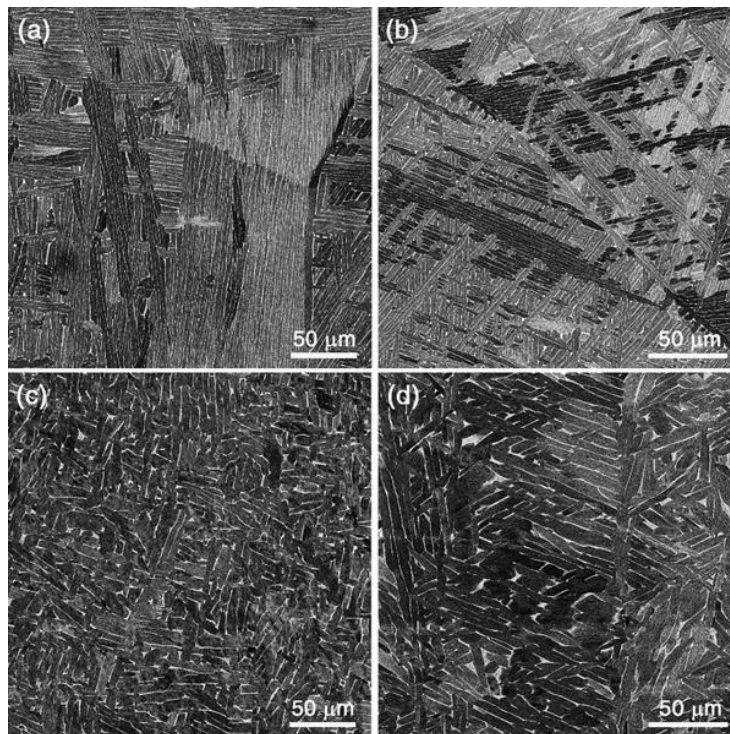

Figure 115.   SEM BSE Images of SCIACKY Ti-6Al-4V Sample
Sectioned from (a) perpendicular to the building direction (X), (b) parallel to the building direction (Z), and of the EBM Ti-6Al-4V sample sectioned from (c) perpendicular to the building direction (X), (d) parallel to the building direction (Z)

the columnar grain structure of the EBM sample in the *Z* direction, and the presence of coarse a laths is apparent within the elongated grains.
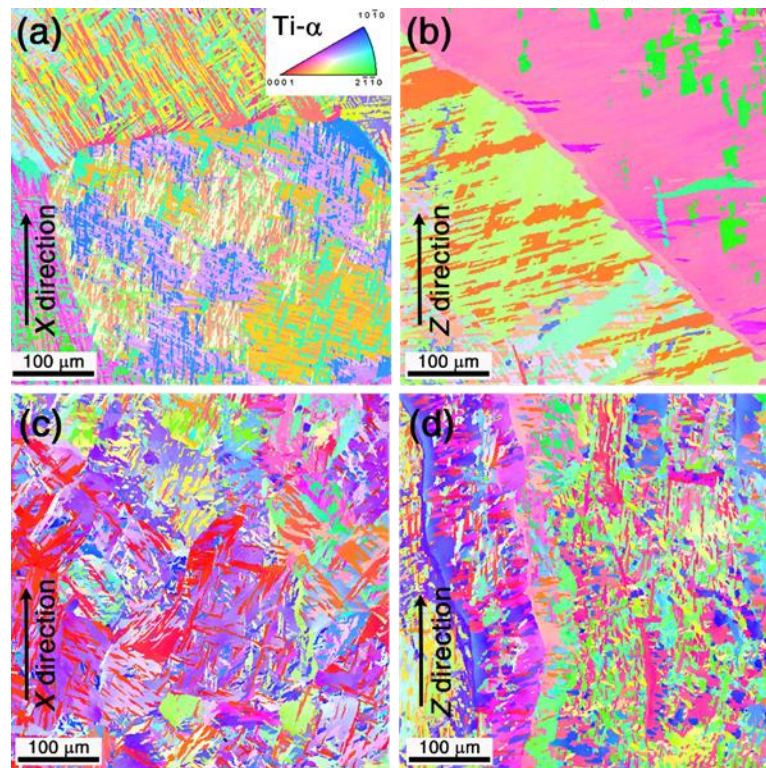

Figure 116.   EBSD Images of SCIACKY Ti-6Al-4V Sample
Sectioned from (a) perpendicular to the building direction (X),
(b) parallel to the building direction (Z), and of the EBM Ti-6Al-4V
sample sectioned from (c) perpendicular to the building direction (X),
(d) parallel to the building direction (Z)

Figure 117 shows the crack growth rates for the SCIACKY sample in the *X* and *Z* directions and the EBM sample only in the *Z* direction at the stress level of 240 MPa and stress ratio of *R*= -1. Similar threshold values (ΔK_{th}) were obtained for crack growth of the processed samples. The crack growth rate of the alloy processed by both EBM and SCIACKY routes was detected to be lower than 10^{-8} (*m*/Cycle) at D*K*=10 MPa.m$^{1/2}$ suggesting the improved fatigue crack growth resistance of the developed alloys in this study compared to other AM Ti-6Al-4V. In the present study, the EBM sample shows a higher crack growth rate for a given stress intensity range compared to the SCIACKY samples. The higher crack growth rate for the EBM sample compared to the SCIACKY specimen can be related to the thicker a laths as shown in Figure 115. The observations here show that with increasing the thickness of a laths above 1mm, the fatigue crack growth resistance is reduced suggesting that the number of interfaces acting as barriers to deflect the cracks decreases. Higher or similar crack growth rates in the same range of stress intensity factors tested here were reported for the fatigue crack growth behavior of wrought and AM Ti-6Al-4V alloys with bimodal or lamellar microstructures at the stress ratio of -1.
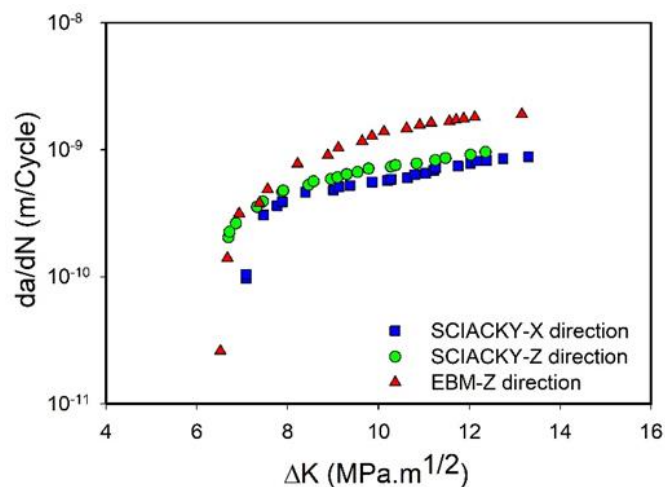
Figure 117.   Crack Growth Rate vs Stress Intensity Factor Range,
ΔK, for the SCIACKY and EBM Samples

To characterize the crack interaction with the microstructure in SCIACKY and EBM samples, the EBSD maps of the microstructures in front of the notch tips are presented in Figure 118 and Figure 119. The cracks are superimposed on the inverse pole figure and Schmid factor maps from the image quality maps. EBSD observations show that short crack growth behavior is not sensitive to the grain boundaries, and it is strongly affected by the length scale of a laths and local crystal–lographic orientations at the crack tips. In addition, the crack propagation along the regions with the highest Schmid factor for the basal slip system is characterized for both EBM and SCIACKY samples. The crack growth is mainly accommodated by following the lamellar interfaces and cutting through some of the laths in the SCIACKY sample with deflection and branching (Figure 118), while the crack mainly grows by crossing the laths or colonies and growing along some of the laths having various orientations in the EBM sample (Figure 119). Ultimately, it is suggested that for both SCIACKY and EBM samples, the lamella spacing in the range of 1-2.5mm is large enough to retard crack growth where the cracks propagate via a combination of cutting through and passing along the laths.

Figure 120 shows fracture surfaces of the SCIACKY and EBM samples which were loaded parallel to the Z (building) direction in the fatigue testing. No voids or porosities were identified in the fatigue fracture surfaces of both samples. Distinct fatigue fracture surfaces were observed for the EBM and SCIACKY samples. The SCIACKY sample exhibited a more faceted fracture surface due to the propagation of cracks along lamella with larger aspect ratios. However, a rougher fracture surface was characterized in the EBM sample as the crack passed through coarser colonies. It is suggested that although the fracture surface of the EBM sample is rougher, the crack comes across a smaller number of colonies and thereby a lower resistance to fatigue crack growth is observed.
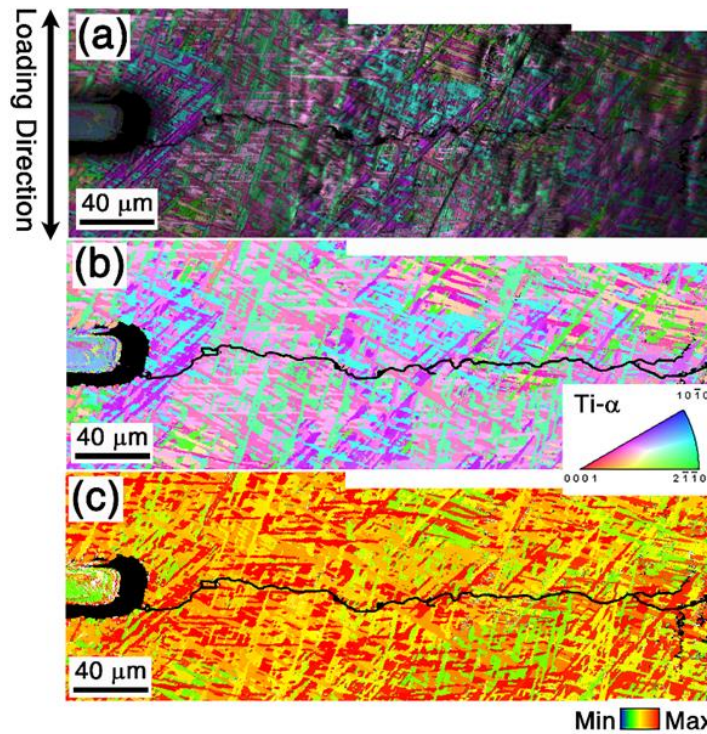
Figure 118. EBSD Images of Gage Length in Front of Notch Tips at End of Crack Growth Experiment for SCIACKY Sample in Z (Building) Direction
(a) inverse pole figure (IPF) with image quality (IQ) map
(b) inverse pole figure (IPF) with superimposed cracks from
(a) and (c) Schmid factor map with superimposed cracks from (a)

Figure 119. EBSD Images of Gage Length in Front of Notch Tips at End of Crack Growth Experiment for EBM Sample in Z (Building) Direction
(a) inverse pole figure (IPF) with image quality (IQ) map (b) inverse pole figure (IPF) with superimposed cracks from (a) and (c) Schmid factor map with superimposed cracks from (a)
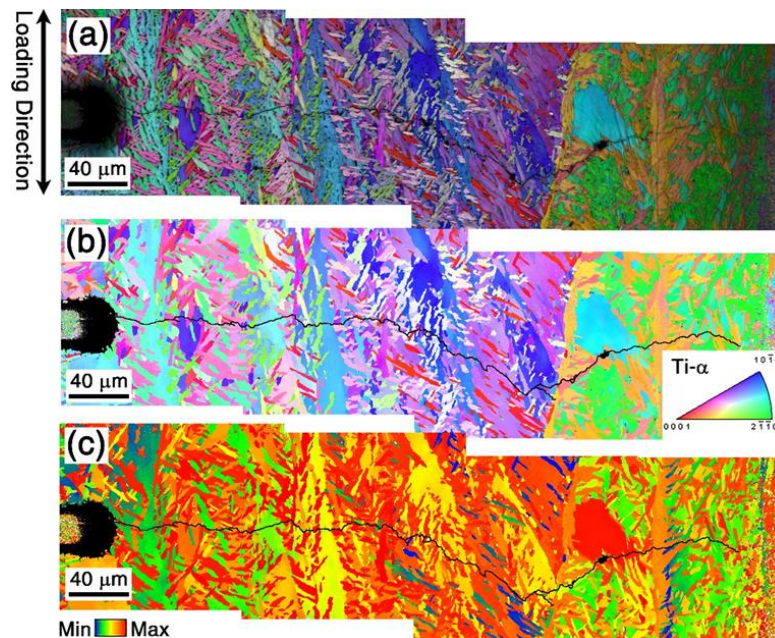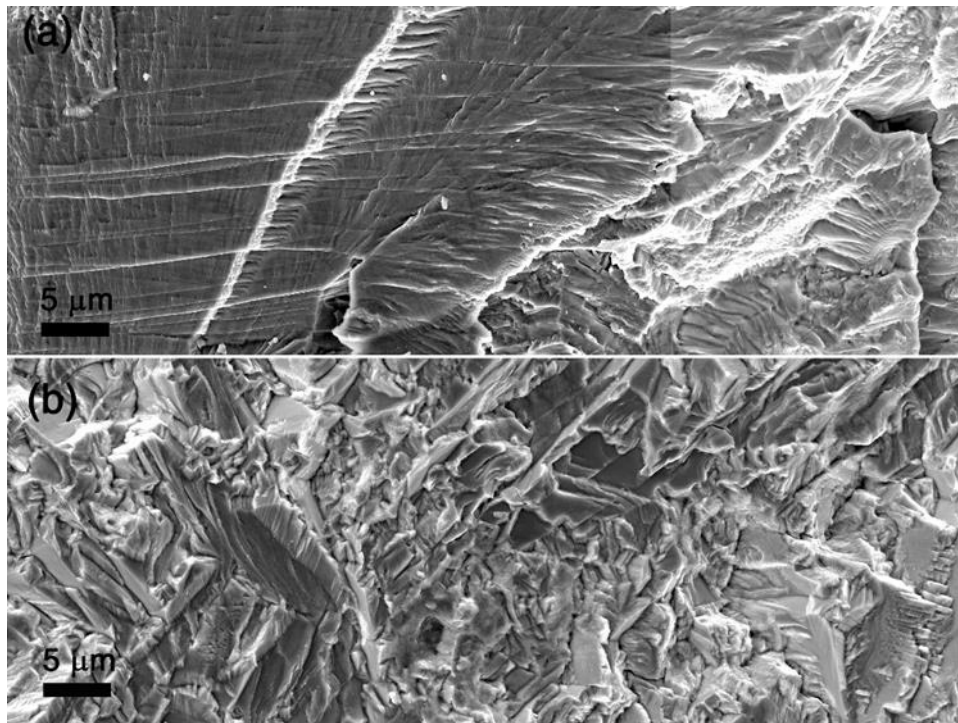
Figure 120. SEM Fatigue Fracture Surface Images Along Z (Building) Direction
(a) in the SCIACKY sample, and (b) the EBM sample

4. Conclusions

Several conclusions can be drawn from this work, presented here in order of relevant deliverable.

- For the standard rapid qualification procedure via USF, the results were not conclusive. This can likely be attributed to the spread in defect size distribution in the underlying sample population. Further work extending to other material systems with a tighter distribution would likely mitigate some of the resultant spread in fatigue life.

- Strong improvement in productivity of L-PBF AlSi10Mg can be realized via beam shaping as a result of the assessment in this project. It is expected that a increase of >2X in productivity can be achieved via non-Gaussian laser beam shaping without a serious debit in mechanical properties. Increases in elongation were also observed.

- L-PBF aluminum port-and-pressure plate components were constructed and tested as a part of this work. A new design incorporating the geometric benefits of AM was used and subjected to aggressive cyclic pressure testing without failure – matching comparable performance in a conventional part. This new AM design likely remains conservative and subsequent iterations can possibly further optimize the geometry.

- A titanium (Ti-6AL-4V) component was constructed via EBM. This titanium manifold was a further refinement of a design that was initiated in Phase I of this project. The surface of these manifolds was exposed to chemical milling to remove different amounts of material and the final parts' exposure to fatigue testing revealed a positive correlation between chemical milling and fatigue performance in the tested range. Minimal build-to-build and machine-to-machine variability was observed.

- A major thrust of Phase II was the improvement of material properties in binder jetting – specifically with steels. Successful full factorial experiments on 17-4 in binder jetting were conducted at Brown University and relevant parameters identified for use in future design. Additionally, strong initial fatigue performance was found in binder jet 4340 steel. Novel heat treatments combined with a HIP operation were also explored in the interest of enhanced productivity.

- A number of in-situ monitoring techniques for L-PBF and EB-PBF were assessed as a part of Phase II. Non-destructive testing currently consumes approximately 30% of part cost during production and certain techniques have now been identified that can assist in scaling back this amount.

- Critical flaw size models were developed both in binder jet 17-4 and queried in EB-PBF and SCIACKY Ti-6Al-4V. These models were shown to link surface defect size with fatigue performance reasonably well. Assuming these defects can be controlled going forward, this allows for some tuning of ultimate fatigue performance.

5. Project Benefits

5.1 Benefits for the General Public

Prior to this project's initiation, there were several gaps in AM space when it comes to improving material properties and enhancing productivity across multiple modalities. Among the key benefits coming out of Phase II, L-PBF productivity has been shown to greatly improve with non-Gaussian beam shape (>2X). EBM Ti-6Al-4V has shown dramatic improvement in fatigue performance with chemical milling and binder jetting steels have also demonstrated enhanced mechanical properties. Collectively, these benefits allow industry to gain more confidence in AM techniques, expanding the range of design space and yielding promising new avenues for the underlying technology.

5.2 Benefits for DOD

Specifically for the DOD, this project is beneficial in that it allows for greater acceptance of AM as a legitimate means of fabricating components in components with higher degrees of criticality. It has been successfully demonstrated that these components have performed at or exceeded baseline requirements. This leads to increased confidence in the utility of AM going forward, especially in new technologies such as binder jetting of steels. New components will be able to be designed and constructed with an enhanced degree of readiness.

6. References

[1]   Agrawal, A. K., Rankouhi, B., & Thoma, D. J. (2022). Predictive Process Mapping for Laser Powder Bed Fusion: A Review of Existing Analytical Solutions. *Current Opinion in Solid State and Materials Science*. doi:https//doi.org/10.1016/j.cossms.2022.101024.

[2]   ASTM E8/E8M-16a. Standard Test Methods for Tension Testing of Metallic Materials. ASTM International, West Conshohocken, PA, 2016, www.astm.org.

[3]   Kuhn, H. M. (2000). *ASM Handbook, Volume 8: Mechanical Testing and Evaluation.* ASM International.

[4]   Mayer, H. (2016). Recent Developments in Ultrasonic Fatigue. *Fatigue and Fracture of Engineering Materials and Structures, 39*, 3-29. doi:https://doi.org/10.1111/ffe.12365.

[5]   Murakami, Y. (2002). Metal Fatigue: Effects of Small Defects and Nonmetallic Inclusions. Elsevier.

[6]   Schonbauer, B. (2020). Defect-Tolerant Design in the High and Very-High Cycle Fatigue Regime. iMdc Spring 2020 Meeting.

[7]   SAE International Surface Vehicle Recommended Practice. Chemical Milling of Metals, Specification for AMSC81769. SAE Standard AMSC81769, Rev. 2008.

[8]   Tahmasbi, K., Alharthi, F., Webster, G., & Haghsenas, M. (2023). Dynamic Frequency-Dependent Fatigue Damage in Metals: A State-of-the-Art Review. *Forces in Mechanics*. doi:https://doi.org/10.1016/j.finmec.2023.10016.